



University of
Stavanger

Faculty of Science and Technology

MASTER'S THESIS

Study program/Specialization:

Petroleum Geosciences Engineering

Spring, 2017

Open

Writer:

Leah Jean Koch

(Writer's signature)

Faculty supervisor:

Nestor Fernando Cardozo Diaz

Title of thesis:

3D reconstruction of a normal fault zone: A trenching study on a strand of the Baza fault, Central Betic cordillera, south central Spain

Credits (ECTS): 30

Keywords:

Fault Zone
Baza Fault
Structural Model
LiDar
Photomosaic

Pages: 100

Stavanger, 12, June 2017

Copyright

by

Leah Jean Koch

2017

**3D reconstruction of a normal fault zone: A trenching study of a strand of
the active Baza fault, Central Betic Cordillera, south central Spain**

by

Leah Jean Koch, B.S

Thesis

Presented to the Faculty of Science and Technology

The University of Stavanger

The University of Stavanger

June 2017

DEDICATION

I would like to dedicate this thesis to my sister-in-law, Jannica Schmoecker for encouraging me to reach higher.

ACKNOWLEDGEMENTS

I would first like to acknowledge all the people who were involved in this project. First and foremost, I want to offer my immense gratitude to Nestor Cardozo, for endless guidance, assistance, and inspiration throughout this thesis. I would also like to thank Ivàn Martin-Rojas, Pedro Alfaro, Julia Castro, Ivàn Medina-Cascales, and Francisco García-Tortosa for your contributions to this project, both in the field and interpretation of the data. Also, there is also Simon Buckley and Benjamin Dolva who offered their expertise in processing the LiDAR data, Jan Tveranger and Jacob Dieset for their invaluable assistance and knowledge in the field, and Isabelle Lecomte for her work with seismic modeling. This thesis would not be possible without the collaboration from all of these intelligent and generous individuals. Thank you all very much; you truly were the best resource.

I would like to thank my fellow students who have inspired, pushed and reassured me over the past two years. It has been an honor to work with you and I look forward to working with you in the future. Also, my parents, Deb and Carl Koch, who have always been a foundation of support. Lastly, I would like to thank my wonderful husband, Sindre Schmoecker, who offered unwavering support and encouragement throughout the last two years. I could not have done it without you.

3D reconstruction of a normal fault zone at sub-seismic scale: A trenching study of a strand of the active Baza fault, Central Betic Cordillera, south central Spain

by

Leah Jean Koch, M.S.

The University of Stavanger, 2017

SUPERVISOR: Nestor Fernando Cardozo Diaz

Faults are rarely a discrete two-dimensional surface, but a three dimensional volume with a complex internal structure. Faults are commonly encountered in reservoirs and evaluated for their ability to act as a fluid flow conduit or barrier. The problem is that the structure of a fault zone in 3D is poorly understood, particularly because outcrops exposing fault zones in 3D are rare, and few have large (e.g. 100 m) throw. Detailed 3D outcrop studies of fault zones can help provide insight into their internal structure, and the processes undergone during faulting, as well as improve the predictability of subsurface (e.g. reservoir) models. The main objective of this project is to construct a 3D structural model of a strand of the Baza fault, an active normal fault located in south central Spain in the Betic Cordillera. This strand is one of the many strands on the Baza fault system, and has an estimated throw of 30 meters in relatively unconsolidated clay to silt Pliocene sequence. Through a trenching study 8 vertical dip sections, 3 vertical strike sections, and one depth section in an area of approximately 80 m² were excavated, cleaned, LiDar scanned, photographed, and documented. Based on these sections, we have reconstructed the 3D geometry and associated structures of this superb fault zone. These data can be used to study the variability of fault zones in 3D, but also for geophysical (e.g. seismic imaging) and reservoir modeling studies.

TABLE OF CONTENTS

List of Tables	viii
List of Figures	ix
INTRODUCTION.....	1
PREVIOUS WORK.....	6
GEOLOGIC SETTING.....	12
METHODS	17
Field Work	18
Data Processing.....	21
Interpretations	26
Build Model	28
DATASET	30
OBSERVATIONS	33
Lithological Units	33
Structural Units	34
Trench Descriptions	35
Trench A1	35
Trench A2	38
Trench A3	41
Trench A4	44
Trench A5	47
Trench B0.....	50
Trench B1.....	52
Trench B3.....	54
Trench C1.....	56
Trench C2.....	57
Trench C3.....	58

MODEL	59
DISCUSSION	69
CONCLUSION	76
APPENDIX.....	77
REFERNCES	83

LIST OF TABLES

Table 1:	Textural classification scheme for discriminating fault rocks. This has been adapted from the scheme developed by Sibson (1977) with the inclusion of foliated gouge proven possible by Chester et al, 1985. (Scholz et al., 1991)	10
Table 2:	Description of the dataset	31

LIST OF FIGURES

- Figure 1:** Cross section (a-f) along strike of a normal fault zone through a series of Carboniferous sandstones and shales. This fault has a throw of approximately 3 m. These cross sections were constructed from near vertical faces exposed while excavating a quarry. (Childs et al., 1996). 1
- Figure 2:** Illustrates the issue regarding seismic resolution and the ability to image the structures that lie within a fault zone. The seismic line may show what appears to be a single slip surface, but can have multiple geometries that have different implications for reservoir connectivity. (Wibberley et al., 2008) 3
- Figure 3:** The trench is located in south central Spain, in the central Betic Cordillera, approximately 3 km north of Baza. 4
- Figure 4:** Conceptual model of fault zone (Adapted from Chester and Logan, 1986, Smith et al., 1990). The dark region represents the fault core, which can be composed of gouge, cataclasite, and/or mylonite. The gray area represents the damage zone, which can include small faults, fractures, veins, and folds. The protolith, which has been removed so the interior is visible, contains only regional structures (Caine et al., 1996). 7
- Figure 5:** Illustration of the different processes that contribute to fault zone growth at different scales. The dark shaded material indicates the newly incorporated material in each process. The diagonal shading indicates the previously existing fault gouge. Each process involves first material weakening (i) then breaking off and incorporation into the fault zone (ii). (from Wibberley et al, 2008). 8
- Figure 6:** Block diagrams illustrating a simple model of tip-line and asperity bifurcations in three dimensions. Less competent layers (shales) are shaded in black and the more competent layers are white. (a) Initial geometries of fault 1-3 with arrows indicating the direction of propagation that would create this geometry. (b-d) Illustrate the changes in the fault zone with progressive displacement. Fault 1 exhibits tip-line bifurcation, fault 2 exhibits tip-line bifurcation as a result of lithological layering, and fault 3 exhibits asperity bifurcation and lens creation in c and d (Childs et al ., 1996). 9
- Figure 7:** Simplified geologic map of the Betic Cordillera. The location of the Baza Fault is noted by the box near the center of the map. (Alfaro et al., 2008) 12
- Figure 8:** Block Diagram showing the tectonic deformation on the geomorphologic features of the Baza Fault. (García-Tortosa et al., 2008) 15

Figure 9:	Digital terrain model of the Guadix-Baza Basin with the Baza Fault drawn in solid white lines. (García-Tortosa et al., 2008)	15
Figure 10:	Sedimentary units on the hanging wall and footwall of the studied strand of the Baza Fault.	16
Figure 11:	Flow chart describing all the steps completed in the project. Each step is discussed in detail in the following section.	17
Figure 12:	The two trenches originally opened, Trench A and Trench B. The future trenches faces were named after the trench they grew from. The trenches faces connecting trench A and B start with a C.	18
Figure 13:	The team working together to remove the debris from the fresh surface using hand tools.	19
Figure 14:	These pictures demonstrate the coordinate system that was set up on each grid face. (a) Shows the scale from a distance. Each nail has a piece of string tied around and pulled taut. (b) This is a single cell in the coordinate system marked with labels.	20
Figure 15:	This is an example of the corrections applied to the photo. (a) Shows the original photo and (b) shows the same image after lens distortion has been removed and orthorectification has been applied.	22
Figure 16:	Illustrates how the software, Huggins, builds the photomosaics. (a) First, correlating points are identified between two adjacent photos, (b) then stitches the photo together using these points.	23
Figure 17:	Illustrates the progression of processing the meshes and overlaying the photomosaic. (a) Shows the unrefined LiDar data with the data spikes and incidental collection of the surface and ground. (b) Is the same mesh, but the data spikes and unnecessary surfaces have been removed. (c) Shows the photomosaic georeferenced and draped over the mesh in a 3D environment.	25
Figure 18:	(a) Shows the interpretation initially done on the high resolution photomosaic. (b) This interpretation is then reproduced on the mesh in the 3D environment. This sample interpretation was conducted on trench A5.	27
Figure 19:	Illustrates the construction of surfaces from the interpretations. (a) Shows the interpretation of a fault from the different trenches. A surface is interpolated over these lines, and then verified again in the interpretations (b).	28
Figure 20:	Schematic map view of the trenches. The trenches are the black lines and the stipples indicate the side of the trench that was viewed. Each trench is labeled (A1-5, B0-3, and C1-3). The red lines show the major faults crossing the area.	30

Figure 21:	The interpretation of <i>Trench A1</i> . The structural units (SU), faults (F), and lithological boundaries (tops, letters in footwall and numbers in hanging wall) have been labeled on the figure.	38
Figure 22:	The interpretation of <i>Trench A2</i> . The structural units (SU), faults (F), and lithological boundaries (tops, letters in footwall and numbers in hanging wall) have been labeled on the figure.	40
Figure 23:	The interpretation of <i>Trench A3</i> . The structural units (SU), faults (F), and lithological boundaries (tops, letters in footwall and numbers in hanging wall) have been labeled on the figure.	43
Figure 24:	The interpretation of <i>Trench A4</i> . The structural units (SU), faults (F), and lithological boundaries (tops, letters in footwall and numbers in hanging wall) have been labeled on the figure.	46
Figure 25:	The interpretation of <i>Trench A5</i> . The structural units (SU), faults (F), and lithological boundaries (tops, letters in footwall and numbers in hanging wall) have been labeled on the figure.	49
Figure 26:	The interpretation of <i>Trench B0</i> . The structural units (SU), faults (F), and lithological boundaries (tops, letters in footwall and numbers in hanging wall) have been labeled on the figure.	51
Figure 27:	The interpretation of <i>Trench B1</i> . The structural units (SU), faults (F), and lithological boundaries (tops, letters in footwall and numbers in hanging wall) have been labeled on the figure.	53
Figure 28:	The interpretation of <i>Trench B3</i> . The structural units (SU), faults (F), and lithological boundaries (tops, letters in footwall and numbers in hanging wall) have been labeled on the figure.	55
Figure 29:	The interpretation of <i>Trench C1</i> . The structural units (SU), faults (F), and lithological boundaries (tops, letters in footwall and numbers in hanging wall) have been labeled on the figure.	56
Figure 30:	The interpretation of <i>Trench C2</i> . The structural units (SU), faults (F), and lithological boundaries (tops, letters in footwall and numbers in hanging wall) have been labeled on the figure.	57
Figure 31:	The interpretation of <i>Trench C3</i> . The structural units (SU), faults (F), and lithological boundaries (tops, letters in footwall and numbers in hanging wall) have been labeled on the figure.	58
Figure 32:	Shows the 3D interpretation of fault -3. The model to the left shows the interpretations on trench B1, C1, and the floor. On average this fault is 96°/79°N.	59
Figure 33:	Shows the 3D interpretation of fault -2. The model to the left shows the interpretations on trench A5 and the floor section. On average, the fault is 332°/50°E.	59

Figure 34:	Shows the 3D interpretation of fault -1. The model to the left shows the interpretations on trenches B0, A2, and the floor section. On average, this fault is 310°/ 51°E.	60
Figure 35:	Shows the 3D interpretation of fault 0. The model to the left shows the interpretations of trenches B1, C3, A1, and the floor section. On average this fault is 311°/56°E.	60
Figure 36:	Shows the 3D interpretation of fault 1. The model to the left shows the interpretations of trenches A4, B3, and the floor section. This fault strikes 317°/ 49°E.	60
Figure 37:	Shows the 3D interpretation of fault 2. The model to the left shows the interpretations of trenches A2, A5, and the floor section. On average, this fault is 163°/78°SW.	61
Figure 38:	Shows the 3D interpretation of fault 4. The model to the left shows the interpretations of trenches A2, A4, and the floor section. On average, this fault is 321°/33°NE.	61
Figure 39:	Shows the 3D interpretation of fault 5. The model to the left shows the interpretations of trenches A2, A5, and the floor section. On average, this fault is 287°/23°NW.	61
Figure 40:	Shows the 3D interpretation of fault 7. The model to the left shows the interpretations of trenches A1 and the floor section. On average, this fault is 314°/66°NE.	62
Figure 41:	Shows the 3D interpretation of Fault 8. The model to the left shows the interpretations of trench A1 and the floor section. This fault is oriented at 275°/55 °NE.	62
Figure 42:	Shows the 3D interpretation of Fault 10. The model to the left shows the interpretations of trenches A2, B3, and the floor section. This fault is oriented at 328°/57 °NE.	62
Figure 43:	The lithologic boundaries of the footwall stratigraphy. Three horizons were included in the model, (a) Horizon AA, (b) Horizon A, and (c) Horizon C. (a) and (b) have three separate segments. These have been offset by faults -3, and -2. There was no exposure of these horizons in the hanging wall of fault -1. Horizon C (c) only contains 2 separate segments. These have been offset by fault -1. In the footwall, this horizon is horizontal and undisturbed. In the hanging wall, the horizon appears to have been smeared along the fault plane. In the other segments (e.g. footwall of fault -2 and -3), this horizon would be above the model.	63
Figure 44:	The lithologic boundaries in the hanging wall stratigraphy. Six horizons were included in the model, (a) Gravel , (b) Horizon 2, (c) Horizon 4, (d) Horizon 7, (e) Horizon 8, and (f) Horizon 9. These horizons are contained between fault 0 and fault 10. The gravel unit and Horizon 2 (a and b) had similar geometry. They appear to have been smeared up fault 0 in the direction of fault movement. Horizon 4 (c) however looks	64

much different from the other two. This unit has exposures in almost every hanging wall structural unit so it has many different segments. The unit is generally dipping about 30 degrees to the east and offset by the series of faults in the hanging wall. Horizon 7 (d) is a highly deformed unit that forms some of the injection structures seen in the southern portion of the study area. This formation dips gently to the east between faults 0 10. Horizons 8 and 9 (e and f) are also highly deformed units that lie both above and below fault 4. These horizons only exist in one of the structural units to the south of the study area.

- Figure 45:** Cross sections across the model compared to the interpretations of the trenches. The cross sections were created at the approximate location of the trenches to compare the model to the interpretations 67
- Figure 46:** Horizontal sections through the fault model illustrating the vertical variations of the structural units. (a) Shows the location of sections 1 (b), 2 (c), 3 (d), 4 (e), and 5 (f). Sections are 1 m apart. 70
- Figure 47:** Vertical sections through the fault zone illustrating the horizontal variations of the different structural units. The section farthest north is section A (a). The following sections (b), (c), (d), and (e) are progressively southward Image (f) shows the relative location of each section. Sections are 3 m apart. 70
- Figure 48:** Comparison of Baza rock and fault zone thickness of the studied Baza fault strand and other studies compiled by Childs et al. (2009). Notice that the fault rock thickness in the Baza fault strand changes over an order of magnitude along strike. 73
- Figure 49:** Illustrates the comparison of scale of the data from the trenches to a seismic section. (a) Is a generic seismic section of a normal fault. Zooming into the seemingly single slip surface can actually be multiple slip surfaces. If you zoom in even more to (c) the outcrop scale, the structure becomes even more complex. This continues down to (d) the hand sample scale. (a and b were adapted from Wibberley et al., 2008) 74
- Figure 50:** Seismic Modeling of trench A3 by Isabelle Lecomte at UiB. The input to the model is the trench lithology (a) which has been assigned elastic properties (b). (c) is the modeled seismic response using a ray-based pre-stack depth migration simulator (Lecomte et al., 2015, 2016) with perfect and limited illumination. The modeled image is equivalent to high frequency seismic and ground radar. (Courtesy of Isabelle Lecomte, unpublished) 75

INTRODUCTION

Faults are rarely a single, discrete two-dimensional discontinuity (Wallace and Morris, 1979; Cox and Scholz, 1988). More commonly, they occur as highly irregular zones of extreme internal complexity bounded by two primary parallel slip surfaces. The slip surfaces usually envelope fault rock that has undergone varying degrees of ductile strain, cataclasis, and rotation (Childs et al., 1996; Childs et al., 2009). As displacement increases, growing the fault zone in length, width and depth, heterogeneities in the material react differently to the stress field and create diverse geometries overprinting on prior events. The result of this reiterative process is a variable and unpredictable structural architecture (Childs et al., 1996). Figure 1 shows an example from a Carboniferous quarry demonstrating the potential variability over short distances along strike in a fault zone.

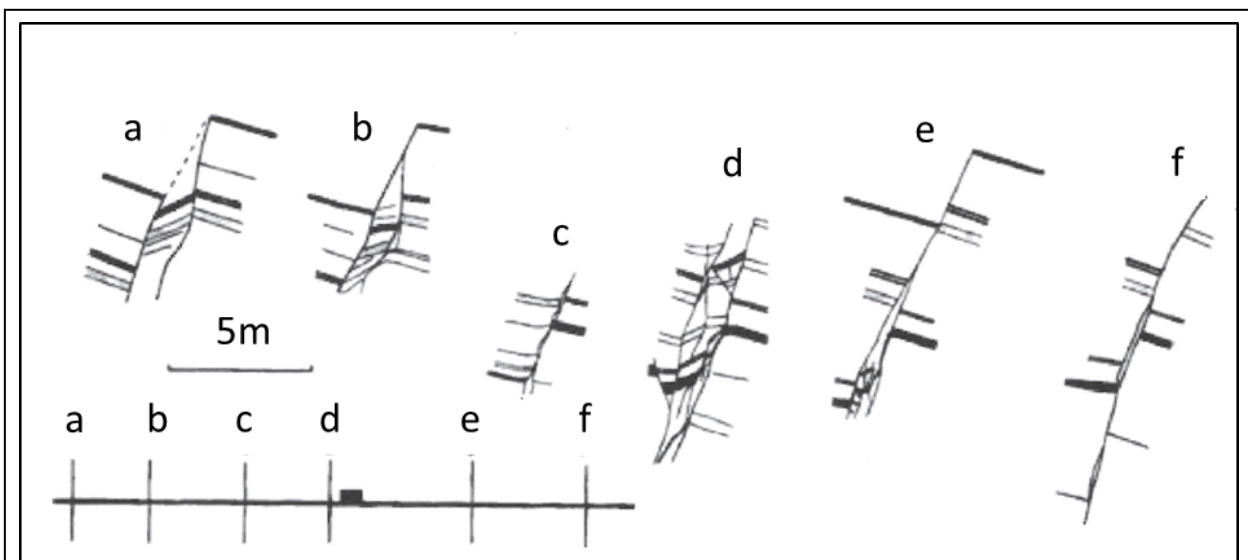


Figure 1: Cross section (a-f) along strike of a normal fault zone through a series of Carboniferous sandstones and shales. This fault has a throw of approximately 3 m. These cross sections were constructed from near vertical faces exposed while excavating a quarry. (Childs et al., 1996)

Despite decades of research, the interaction of the variables and processes involved in the development of these structures are poorly understood, although there are some conceptual models that broadly explain the evolution of these structures (e.g. Childs et al., 2009). Fault zones exist on a wide range of space-time scales, from mm to 100s km and centuries to eons. Over these spatial and temporal ranges, there is potential

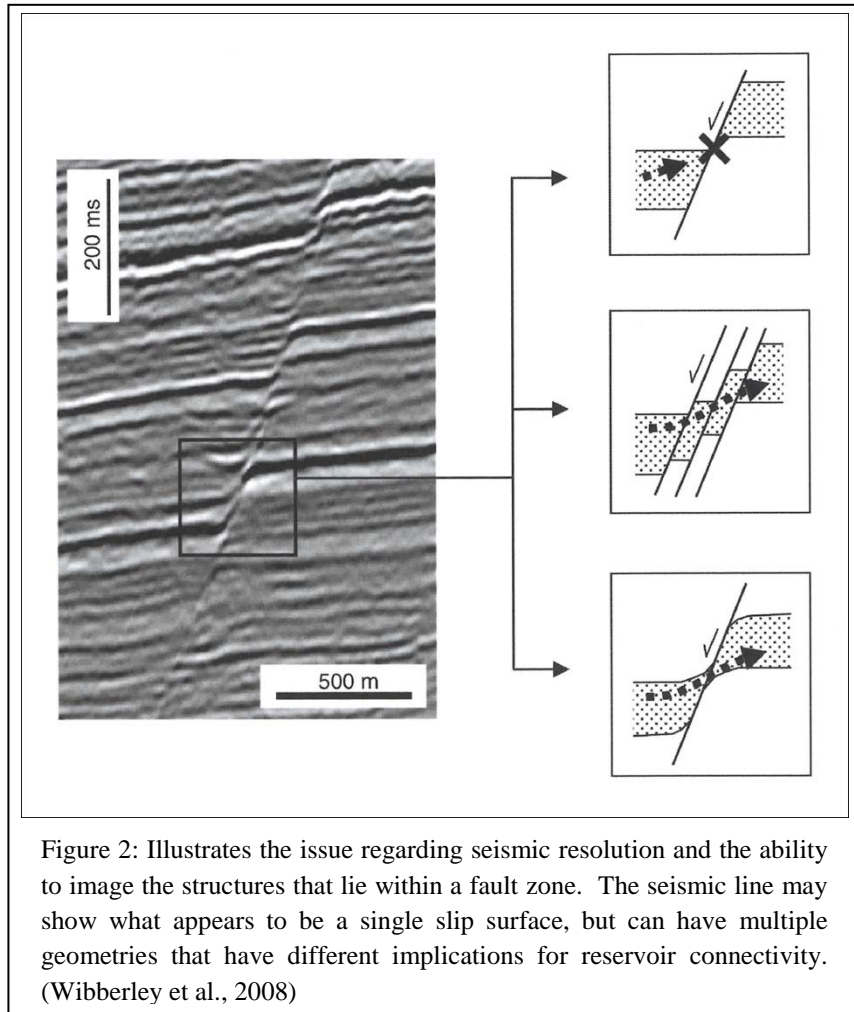
for vastly different petrophysical, rheological properties, and prior structural elements. It is incredibly difficult to quantify all the variables involved to adequately understand fault zones (Ben-Zion and Sammis, 2009).

Faults are encountered in nearly all geoscience disciplines and have important effects on the systems of which they are a part. Notably, they are among the most important structures when studying earthquakes, geothermal systems, exploration and production of minerals, and reservoir systems (e.g. hydrocarbons, water, or CO₂). A thorough understanding of structural and functional components in the zone of deformation caused by faults is vital to fully understanding these systems.

In reservoir systems, faults are evaluated for their ability to act as a fluid conduit, baffle or barrier (Wibberley et al., 2016). For example, determining migration pathways in hydrocarbon exploration may require fluid flow through a fault zone conduit. Reservoir recharge rates in aquifers through a fault zone acting as a baffle could have important repercussions for regional water resources. In the case of CO₂ storage, compartmentalization could be desirable, thus requiring a sealing fault system.

Understanding the properties of a fault zone can have important impact on the modelling of fluid flow behavior. The dataset commonly used for evaluating these properties is seismic data. This can be problematic because much of the structure that exists in a fault zone is below the resolution of seismic data. What would appear to be a single slip surface on seismic, may actually be multiple slip surfaces, creating a conduit that would otherwise appear as a barrier (Figure 2). By refining our understanding of the formation of fault zone structures, the prediction of their behavior can be greatly improved.

Fault zones have similar implications to geothermal resources. The fracture systems in a fault zone control the flow of fluids. Aside from transporting geothermal energy, the fluids can precipitate minerals, which in turn can clog the fracture system. This can happen very rapidly, on the scale of centuries (Egger et al., 2014). Detailed characterization of



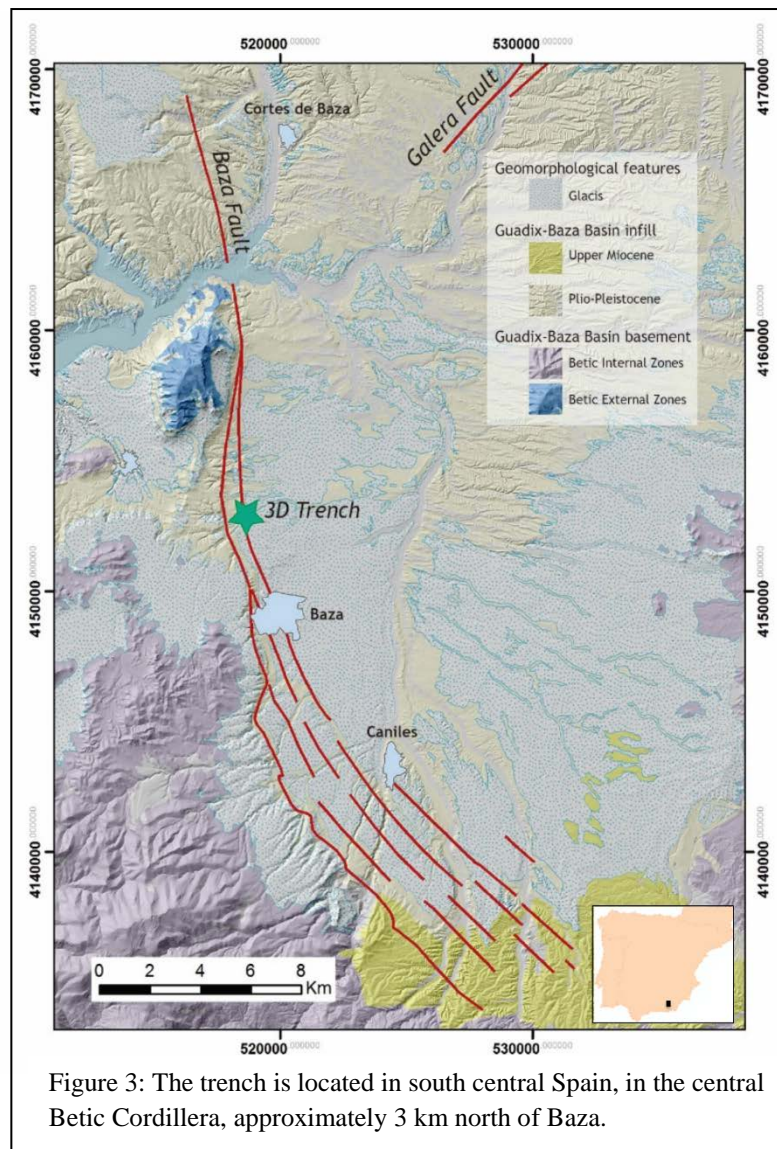
fault zones can improve the understanding of hydrothermal systems, fluid flow through fracture networks, and harnessing of geothermal resources.

The zone of deformation records a series of events that occur under different physical conditions during their evolution (Chester, 1995; Chester and Chester, 1998; Wang et al., 2014). Reconstructing these events can provide valuable insight regarding the mechanical properties and behavior of a fault. This is useful information that can be applied to improving the prediction of nucleation, propagation and arrest of earthquakes. Understanding this process can improve earthquake risk classification and warning systems.

Over the past couple of decades, there has been an invigorated interest in fault zone studies motivated by constant advancements in seismic data quality and pressure on the industry to improve production and recovery. Numerical modeling and seismic

data processing has become more sophisticated. However, there is a noted lack of outcrop studies, especially those with high-resolution data and three-dimensional outcrops (Wibberley et al., 2008; Manzcchi et al., 2010). These studies can provide highly valuable datasets when researching the processes and mechanical properties of fault zones over varying geologic settings. Field data provides a foundation for which improvements of the aforementioned techniques can be built upon.

Approximately 3 km north of the Spanish town of Baza (Figure 3), a paleoseismology study exposed a fault strand. A trenching campaign conducted into the quaternary deposits exposed a spectacular fault zone structure beneath. It consists of an active normal fault with an estimated throw of 30 meters. This fault strand inspired this project, which investigates the internal structure of a normal fault from an excavation field campaign that exposed the fault zone in three dimensions. This project underwent four phases: data collection, data processing, interpretation and



3D model construction. The data was collected during a field campaign where the fault was excavated by digging several trenches along the strike, perpendicular to the fault. The data collected included LiDar, photographic data, and field observations. The photos were compiled to create high-resolution photomosaics of each trench face.

They were then draped over the LiDar point clouds in a 3D visualization software. In this environment, the sections were interpreted and correlated to build key fault and lithological contacts surfaces. The final result of this process is a 3D reconstruction of the major structural components of the fault zone. This provides a high-resolution sub-seismic outcrop dataset that can be used for studying the internal structure, properties, and processes in the fault zone.

PREVIOUS WORK

John Wesley Powell observed and described the structure of a fault zone for the first time ca 1870 (Wibberley et al., 2016). Fault zones have since been thoroughly studied by industry professionals and academics alike because of the important implications fault zone properties can have. Permeability structures around fault zones were found to have profound effects on reservoir production and fault geometry was found to relate to seismicity. As the understanding of faults emerged over the next century, research intensified to develop a framework for discussing fault zones. Early studies examined the effect of clay rich gouges from the fault core of large strike slip faults, like the San Andreas Fault in western United States (Chu et al., 1981; Morrow et al., 1984). A study by Chester and Logan (1986) investigated the high permeability zones in peripheral fractures around faults developed the precursor definitions of the fault zone anatomy (Wibberley et al., 2008; Smith et al., 1990). Caine et al. (1996) later adapted these ideas in his discussion of fault zone architecture and the implications to the permeability structure. This study defined the components of a fault zone, which are still accepted today. Fault zone kinematics and the process of reworking fault rocks into the fault zone was first discussed by Tchalenko (1970) in his study regarding the formation of fault gouge in shear zones at various scales (Brosch and Kurz, 2008). The mechanical process for how a fault zone grows lengthwise and widthwise were defined by Childs et al. (1996). The work conducted by the aforementioned researchers and their contemporaries has coalesced into today's framework for discussing the structure and function of fault zones.

It has been established that fault zones are composed of three distinct elements, the undisturbed protolith, the damage zone and the fault core (Figure 4), but all elements are not necessarily present in each fault zone (Caine et al., 1996). The protolith is the undisturbed rock containing only the regional structures. The permeability structure is the same as the unfaulted host rock and all fault related structures are absent. The damage zone is bound by the protolith. The features found here are mechanically related to the fault impeding on the protolith through fault propagation and growth (Caine et al, 1996). The structures possibly present include smaller faults, fractures, veins or folds. These cause heterogeneity and anisotropy in the permeability and structure of the fault zone. The innermost element is the fault core, where a majority of the fault displacement is accommodated. Possible features present include single slip surfaces (Caine et al., 1996), unconsolidated clay rich gouge zones (Andersen, 1983), brecciated and

geochemically altered zones (Sibson, 1977), or highly indurated cataclastic zones (Chester and Logan 1986 and Caine et al., 1996). Currently, a scalar relationship has not been established between all components. In fact, the proportions tend to be highly variable (Childs et al, 2009, their Figure 4).

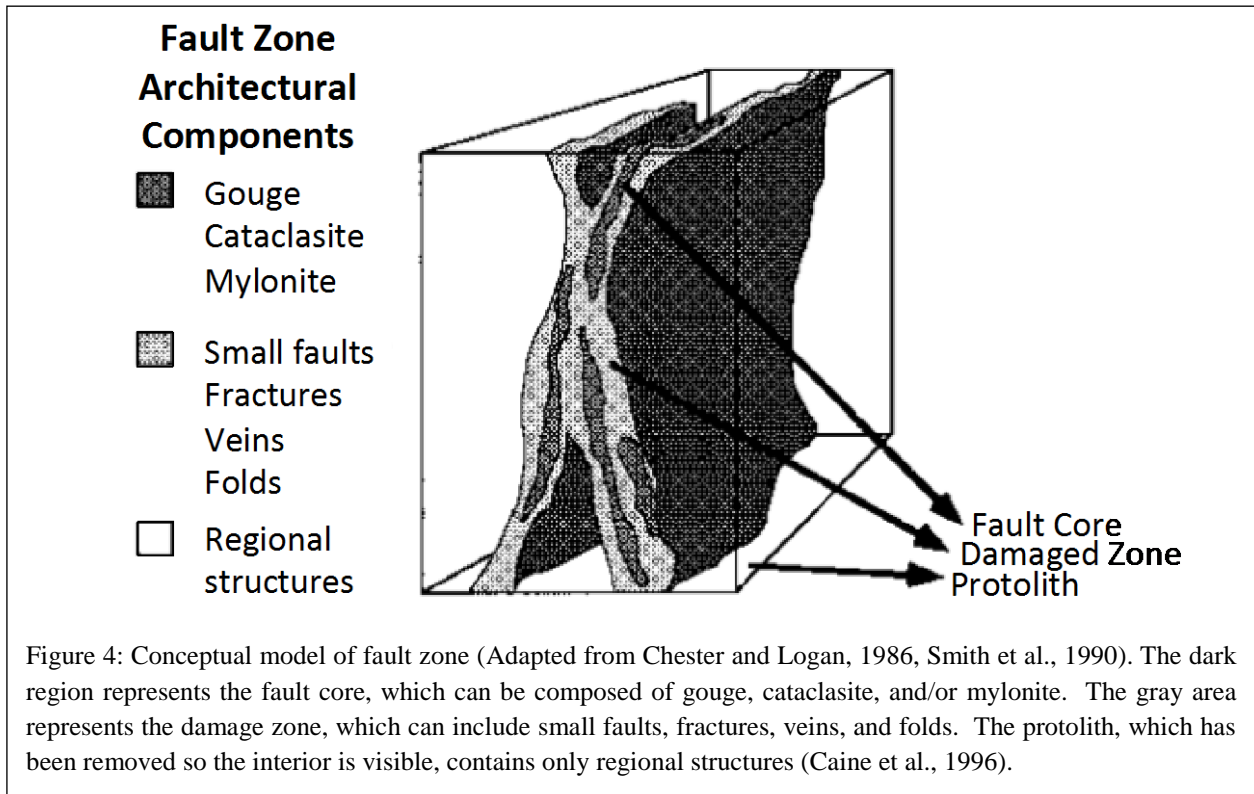


Figure 4: Conceptual model of fault zone (Adapted from Chester and Logan, 1986, Smith et al., 1990). The dark region represents the fault core, which can be composed of gouge, cataclasite, and/or mylonite. The gray area represents the damage zone, which can include small faults, fractures, veins, and folds. The protolith, which has been removed so the interior is visible, contains only regional structures (Caine et al., 1996).

The fracture density also varies over the width of a fault zone. It tends to be greater in the damage zone. This could be due to its propensity towards brittle deformation. In the fault core, the permeability structure is dominated by grain scale permeability of the fault rocks, whereas the fracture network controls the permeability in the damage zone. The geometry and magnitude of permeability contrasts between the fault core and damage zone are primary controls on the barrier conduit systematics of a fault zone (Caine et al., 1996).

Mature fault zones, which are those considered to have been active longer relative to their size, are more likely to have smooth slip surface allowing for more rapid slip. In immature faults, it is more common to have rough planes (Sagy et al., 2007). The complexity of fault zones will also increase with maturity. Fault zone complexity is strongly dependent on the lithology of the protolith, preexisting structures, mechanical layering of the materials, depth, stress regime, and evolution during the life of the fault (Sibson, 1977; Butler et al., 1995; Wibberley 2008).

With increasing displacement, structures overprint over prior structures creating a progressively more complex geometry.

The process of reworking protolith to core rocks has two steps. First the protolith weakens under stress, converting the undisturbed rock into damage zone rocks. The weakened material then breaks off and becomes incorporated into the fault core (Figure 5). This process can occur at small scale through tip process zone microfracturing, larger scale segment linkage by relay breaching and lens formation, and at the largest scale, splay faulting and reconnection, which can form sidewall rip-outs. Through these steps, the protolith is converted to fault gouge material.

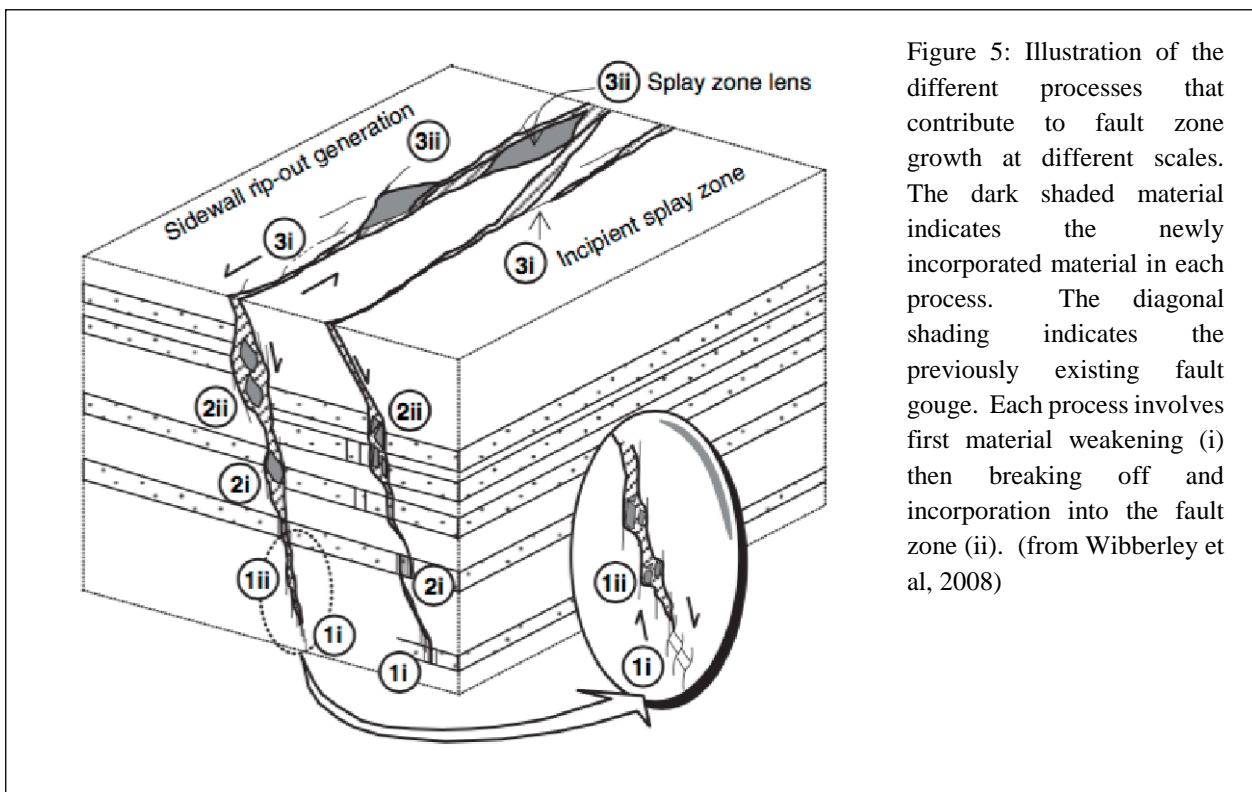


Figure 5: Illustration of the different processes that contribute to fault zone growth at different scales. The dark shaded material indicates the newly incorporated material in each process. The diagonal shading indicates the previously existing fault gouge. Each process involves first material weakening (i) then breaking off and incorporation into the fault zone (ii). (from Wibberley et al, 2008)

Cross sections of fault zones commonly show two subparallel slip surfaces that bound the deformed fault core. This geometry arises from the mechanisms of fault growth, which consist of various combinations of tip-line and asperity bifurcation processes (Figure 6). Fault zone thickening by bifurcation is intermittent rather than progressive so the overprinting of these processes with progressive displacement along the fault may cause localized thickening and thinning of a fault zone (Wibberley, 2010).

The process of tip-line bifurcation increases fault zone complexity along strike and depth. It is initiated by minor irregularities that will inevitably result in forking of a tip-line forming subparallel slip surfaces (Huggins et al., 1995). As the fault further propagates, these bifurcated slip surfaces will eventually rejoin, enclosing and creating a lens of material. In layered sequences, the tip-line propagates at different rates through the different layers creating lenses vertically along the fault dip. This process is scale independent and a single tip-line can be bifurcated at several different scales simultaneously (Childs et al., 1996).

Asperity bifurcation is the process by which the fault zone grows in width. This process removes a fault surface irregularity by the generation of a new slip surface that bypasses the original irregularity. There is a very clear tendency for fault thickness to increase with displacement and length. However, some of the widening of a fault zone can be explained through more widely spaced paired slip surfaces created through the tipline process (Childs et al., 1996). A general increase in fault zone thickness results from progressive shearing off of fault asperities. It is simply a larger scale manifestation of the wear processes that generates fault gouge.

The mechanically altered material in the core of a fault zone is classified as fault rock (Sibson, 1977). This material often supports smaller structures contained in the fault core. The possible structures present could include faults, fractures, folds, fluid injection structures, soft sediment deformation, and clay

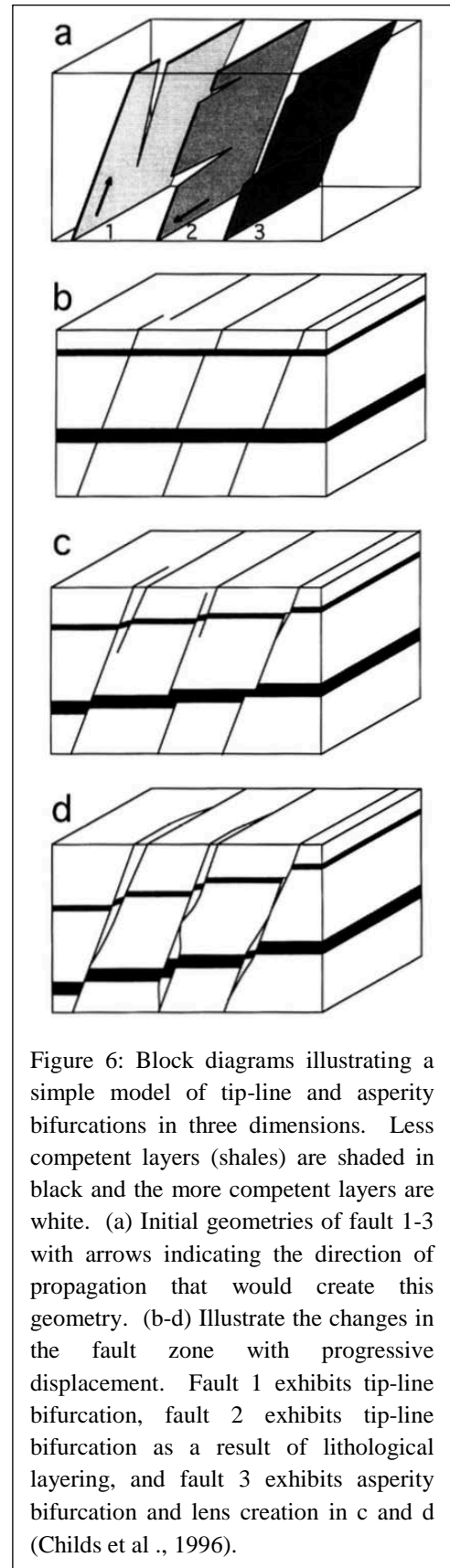


Figure 6: Block diagrams illustrating a simple model of tip-line and asperity bifurcations in three dimensions. Less competent layers (shales) are shaded in black and the more competent layers are white. (a) Initial geometries of fault 1-3 with arrows indicating the direction of propagation that would create this geometry. (b-d) Illustrate the changes in the fault zone with progressive displacement. Fault 1 exhibits tip-line bifurcation, fault 2 exhibits tip-line bifurcation as a result of lithological layering, and fault 3 exhibits asperity bifurcation and lens creation in c and d (Childs et al., 1996).

smearing. The types of structures depend on the deformation mechanism acting on the material.

The nomenclature for differentiating fault rocks has been a subject of debate. The classification schemes use the deformation mechanism and degree of deformation to differentiate between different fault rocks. Sibson introduced the most accepted scheme in 1977, which determined the deformation mechanism by the presence or absence of foliation. However, many critics of this method argue that this assumption has been poorly inferred (Schmidt and Handy, 1997). Chester et al (1986) proved foliations could form in cataclasis of shallow faults through analogue modeling, and later identified in outcrops. Scholz included this finding when he adjusted the Sibson textural classification scheme (Table 1) in 1991. Also in 1991 Schmid and Handy developed a new method that used the deformation mechanism as the discriminating factor, instead of textural indicators of the deformation mechanism. This scheme can be inconvenient because determining deformation mechanisms in hand samples can be quite difficult and commonly a thin section is required.

Soft sediment deformation structures such as convolute laminations, deformed cross bedding, load structures and water escape structures are common in sands and sandstones (Allan et al., 1982; Jones and Preston, 1987; Lowe, 1975; Maltman et al., 1994; Mills, 1983) This structures emerge when primary strata deform while the sediments are temporarily in a weakened state. This can happen through the process of fluidization and liquefaction. Fluidization is caused by the upward directed

Table 1: Textural classification scheme for discriminating fault rocks. This has been adapted form the scheme developed by Sibson (1977) with the inclusion of foliated gouge proven possible by Chester et al, 1985. (Scholz et al., 1991)

Textural classification of fault rocks							
		Random fabric		Foliated			
Incohesive	Fault breccia (visible fragments > 30% of rock mass)		?				
	Fault gouge (visible fragments < 30% of rock mass)		Foliated gouge				
Cohesive	Nature of matrix	Glass-devitrified glass	Pseudotachylyte		?		
			Tectonic reduction in grain size dominates grain growth by recrystallization and neomineralization	Crush breccia (fragments > 0.5 cm)		Percent of matrix	10-100
	Fine crush breccia (0.1 < fragments < 0.5 cm)			0-10			
	Crush microbreccia (fragments < 0.1 cm)						
Grain growth pronounced	Cataclasite Series	Mylonite series	Protocataclasite	Protomylonite	10-50		
			Cataclasite	Mylonite	Phylonite varieties	50-90	
			Ultracataclasite	Ultramylonite		90-100	
?		Blastomylonite					

stress of fluid flowing through a porous medium counteracted by the grain weight, which in turn reduces the strength of the material (Allen, 1982; Lowe, 1976, Nichols et al., 1994). Typical fluidization structures include pillar structures, clastic dykes, and water escape cusps. Liquefaction, on the other hand, occurs when the grain weight is temporarily transferred to the pore fluid by either the collapse of loose grain packing or an increase in pore fluid pressure (Allen 1982, Lowe 1976, Seed, 1979) This can be induced by seismic shaking, water waves, rapid deposition of sediments or groundwater movements. Lacustrine deposits, similar to the ones found in this study area have been proven to be generally favorable to fluidization and liquefaction (Alfaro et al., 1997).

Clay smearing is also a common structure found in fault zones. This is a loosely defined term coined by the hydrocarbon industry to describe the process of incorporating clay from the wall rock in the fault zone (Vrolik et al, 2016).

The abundance of research conducted over the last several decades has developed a sturdy foundation for understanding fault zones. By organizing and understanding data, collecting field observations, and applying numerical models, researchers have begun unraveling the internal workings of fault zones. With a proper framework for understanding the structure, formation, and contents of a fault zone, we can progress the understanding of faults and their zones of deformations to the point of developing predictive models. This would be a powerful framework for earthquake hazard classification, geothermal energy, the oil and gas industry, and other reservoir studies.

GEOLOGIC SETTING

The subject of this study is the active normal Baza Fault, located in the Central Betic Cordillera in Southern Spain. The uplift of the Betic Cordillera was the consequence of the continental collision between the African and Eurasian Plates. This active plate boundary has been undergoing NW-SE directed oblique convergence at an estimated rate of 4 mm/yr since the Miocene (Montenat and Ott d'Estevou, 1990; Sanz de Galdeano, 1990; Herraiz et al., 2000; DeMets et al., 1994). A part of the resultant structure is the NE-SW trending Arc of Gibraltar, the westernmost extent of the Alpine Uplift (Figure 7). The Arc of Gibraltar spans along the coast of Morocco from Oujda in the east to Tangier in the west. This segment is known as the Rif Mountains. The arc then runs across the Strait of Gibraltar to southern Spain from Cadiz to Valencia, and finally into the Balearic Islands. This segment constitutes the Betic Cordillera (Gibbons and Moreno, 2002).

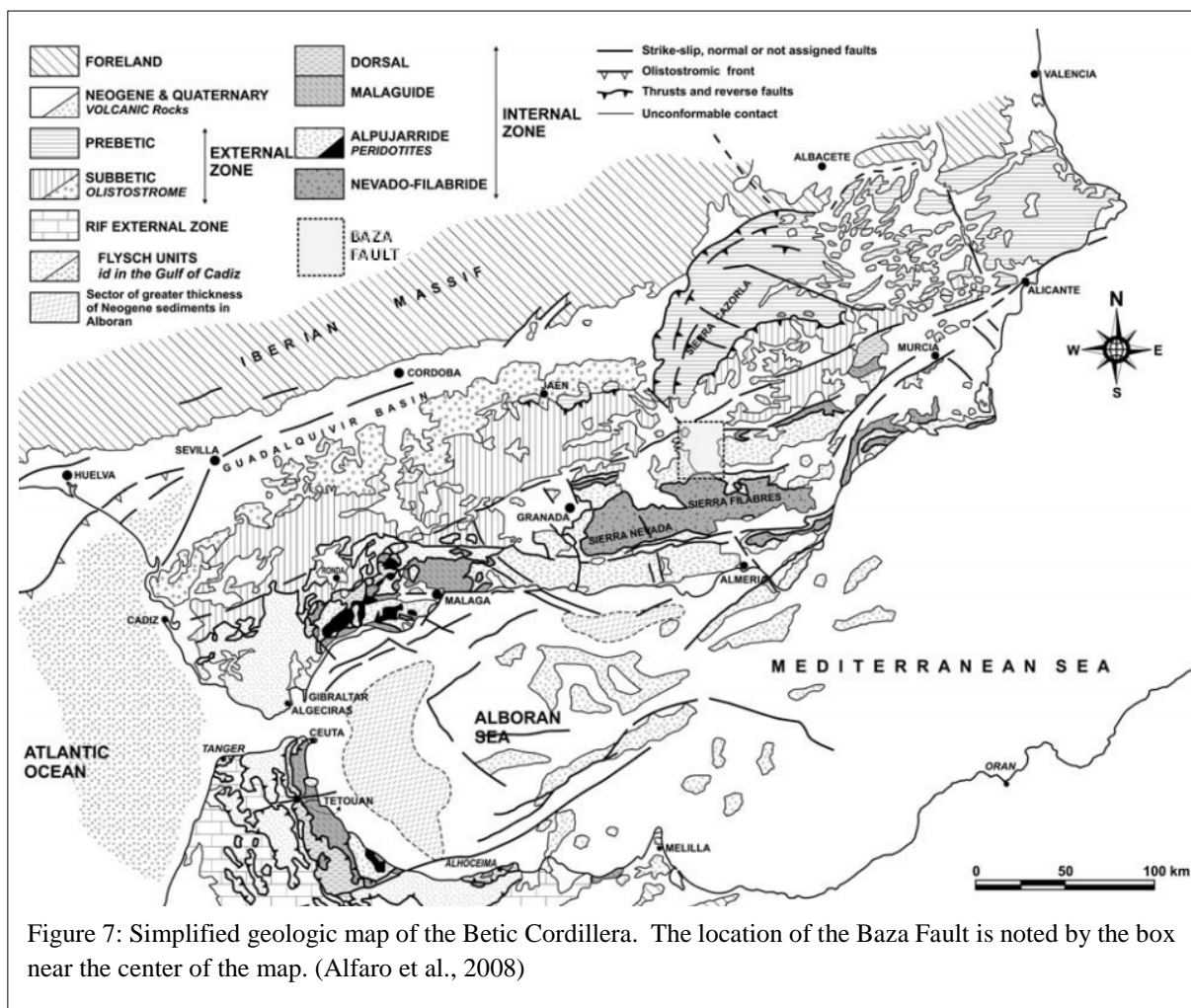


Figure 7: Simplified geologic map of the Betic Cordillera. The location of the Baza Fault is noted by the box near the center of the map. (Alfaro et al., 2008)

The Betic Cordillera is divided into two provinces, the Internal Betic Zone and the External Betic Zone. The Internal Zone is formed by the ancient Mesomediterranean microplate colliding with Iberian plate, which is considered the External Zone. Up until the Miocene, this area was in a marine setting below the Alboran Sea. Uplift beginning in the Tortonian raised a series of mountains belts above sea level, cutting off their intervening basins from the Mediterranean Sea and the Atlantic Ocean. These intermountain basins developed on the hanging wall of the crustal detachments and are considered piggy back basins (Jabaloy et al 1992). They are characterized by low angle normal faults from E-W extension coeval with the compressional geodynamic setting (García-Tortosa et al., 2011; Platt and Vissers, 1989; Galindo- Zaldívar et al., 1989). This study is located in one of these basins, the Guadix-Baza Basin.

The Guadix-Baza Basin encompasses an area of $\approx 4000 \text{ km}^2$. The elevation is as high as 1200 m on the margins and 600 m in the deepest river valleys. The average elevation is 800 m (García-Tortosa et al., 2008). The basin is bound by the uplifted basement with an average elevation of 1500 m with peaks up to 2000 m. The contact between the Internal and External Betic Zone lies underneath the basin in the basement rocks. The external zone is in the northern portion of the basin. It is composed of Triassic to Jurassic carbonates and marls. The rocks of the Internal Betic zone are found in the southern portion of the basin. This zone is composed of early Triassic Nevado-Filábride micashists, quartzite and gypsum, upper-middle Triassic Alpujárride limestones and dolostones, Jurassic Maláguide limestones and dolostones, and the Cenozoic Dorsal Complex limestones. The Alpujárride Fm is exposed in the Sierra de Baza, where it also exhibits low-grade metamorphism. North of the Sierra de Baza is Mt. Jabalcón, which is composed of the Maláguide Fm. North of Jabalcón is the domain of the external Betics, which crop out in valleys near the north end of the Baza fault. (Alfaro et al., 2008).

The contact between the external and internal zones of the Betic Cordillera is covered by Miocene to Quaternary sedimentary deposits. The Miocene sediments were deposited in a marine environment and outcrop in the southern part of the basin, near Bodurria, (Figure 3). These sediments are Tortonian calcarenites and Tortonian to Messinian marls interpreted as fan delta deposits. This is the first tectonostratigraphic unit of the basin and continues until the continental derived deposits (Guerra-Merchán, 1992). The change from marine to continental sediments is a result of the regional uplift of the central Betic Cordillera, cutting this Basin off from the marine influence at the end of the Miocene. Relative uplift caused differential

subsidence allowing continental deposition in the Pliocene and Pleistocene (Vera, 1970; Gibert, 2006; Gibert et al., 2007)

Overlying the marine sediments are the Pliocene to Quaternary fluvial and lacustrine deposits, which are generally separated by the Baza Fault running N-S dividing the basin in two. The Guadix Fm is west of the Baza Fault, on the footwall. These are fluvial sedimentary deposits consisting of siltstone, sandstone, and conglomerates (Von Drasche, 1879; Vera, 1970a, b). On the east side of the fault (the hanging wall), is the Baza Fm. These units consist of lacustrine derived limestone, marls and gypsum (Vera, 1970a). The depositional systems in this Basin were strongly influenced by the movement on the fault. The rivers of the Guadix Fm drained from the northeast over the footwall of the Baza Fault. They then terminated in the large lake of the Baza Fm, which filled a depression formed by the downward motion on the hanging wall of the Baza Fault. This system was active from the Pliocene to the Pleistocene (García-Tortosa, 2008). Sedimentation rates in the lake were estimated to be 0.2 mm/yr by a study in 2006 (Ortiz et al.). Within the Baza lacustrine deposits, there are three concentric facies belts identified, becoming less evaporitic towards the margins. The two inner circles are the Benamaurel Gypsum unit, exposed near their namesake. Detrital and palustrine sedimentary rocks are prominent in the marginal facies belt (García-Tortosa, 2008).

Deposition in the basin ended in the Late Pleistocene when the basin changed from endorheic to exorheic (Calvache and Viseras, 1997). This change was initiated when a meander from the Guadalquivir River drainage system captured the lake and released it into the Atlantic Ocean (Vera, 1970; Calvache and Viseras, 1997; García-Tortosa 2008). After this, sedimentation was restricted to valley bottoms, alluvial fans and piedmont deposits on the outskirts of the basins and on fluvial terraces.

The fault then curves to the east with the Sierra de Baza mountain front. Also, the fault begins as one strand in the north then splays out into multiple and progressively wider spaced strands at the boundary between the internal and external zone which is just north of Mt. Jabalcón. The fault generally dips between 40 and 50 degrees to the east. It has created a half graben structure with 2000 to 3000 m of syntectonic sedimentary infill, which was estimated from a series of gravimetric studies conducted in 2008 (Alfaro et al., 2008).

The location of the study area is indicated by the box in Figure 9. This strand of the fault cuts through the Pliocene and Pleistocene Baza Formation. The sediments found here are described as finely laminated lacustrine derived evaporate deposits locally interbedded with fluvio-deltaic clastics. The stratigraphy between the hanging wall and footwall are completely different. A detailed description of the outcropping units in one of the trenches is shown in Figure 10. The beds consist mostly of clay with some fraction of sand and silt in the hanging wall. The footwall consists mainly of claystone, calcareous siltstone and siltstone. The offset on this strand is estimated to be 30 m from regional estimates. The strike of the fault is variable within the fault zone but has an average N-S orientation and dips 50°E.

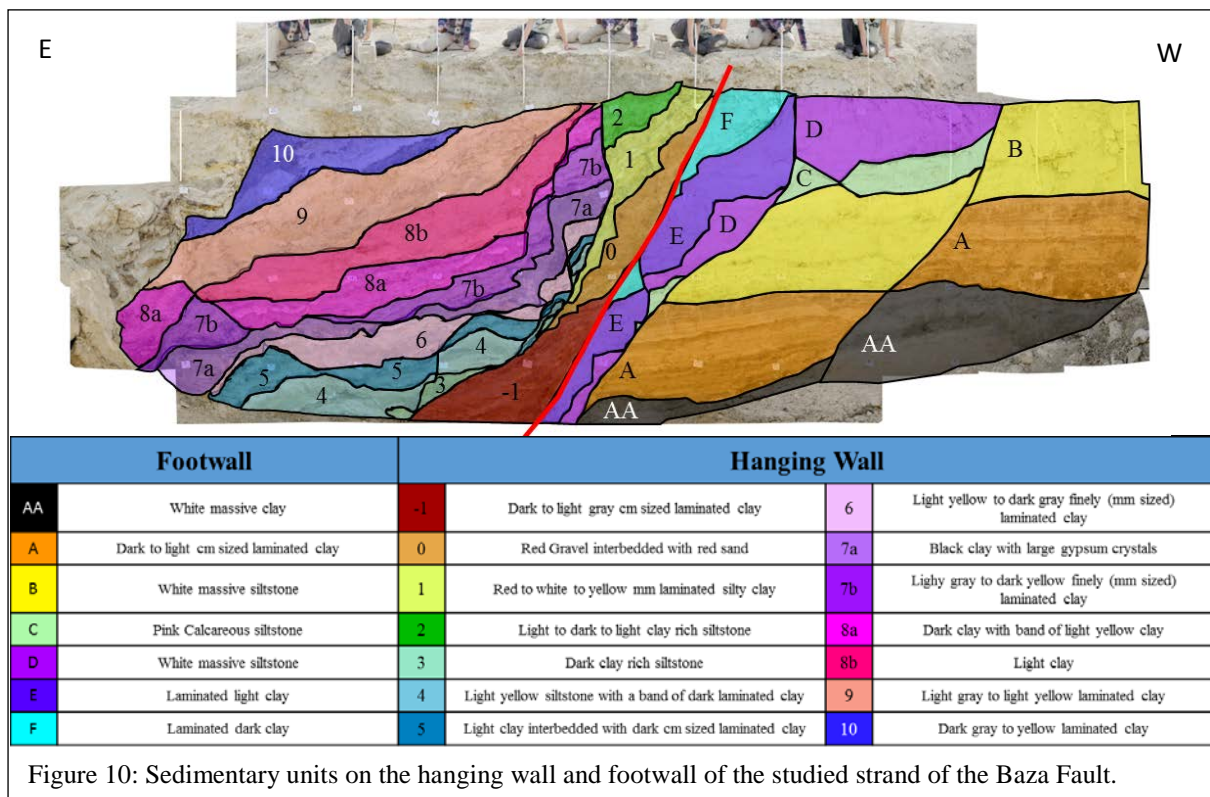
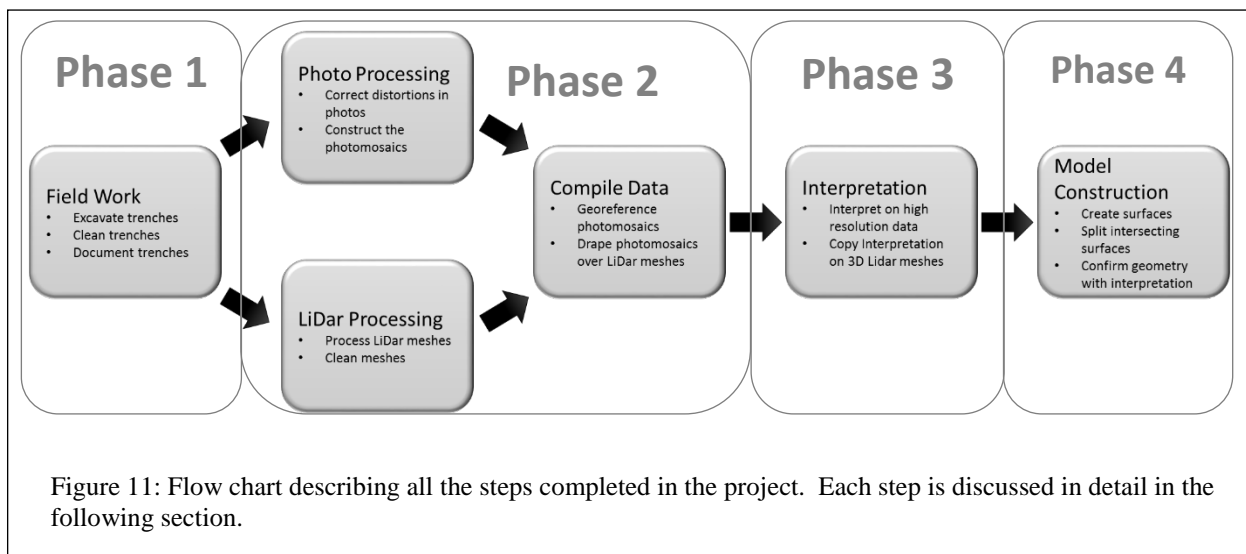


Figure 10: Sedimentary units on the hanging wall and footwall of the studied strand of the Baza Fault.

METHODS

The objective of this study is to reconstruct in three dimensions the zone of deformation associated to a ~30 m throw strand of the Baza Fault. The three dimensional perspective of the fault zone is achieved by progressively exposing the fault perpendicular and parallel to strike as well as a floor section. The fault was unearthed in a 7-days field campaign where the trenches were excavated to reveal the structure and composition of this fault zone while simultaneously being documented. The documentation required meticulous observations, measurements, and data collection to preserve the data for later studies. Photographs were taken to preserve the visual data. These were later positioned in space by georeferencing them to the LiDar point clouds. These were the data used for the fault reconstruction. Four phases were required for this project (1) field data collection, (2) data compilation in software, (3) interpretation of the trench faces, and finally (4) constructing the model. These steps have been outlined in figure 11.



The field campaign in southern Spain began in late November. Seven days were allowed to complete the excavation and data collection. By the end of the trip, 11 separate vertical trenches and a floor section were completed. Shortly afterwards, data processing began with first correcting the photos and then stitching them together to build photomosaics. Next the LiDar data was processed into meshes and input into a 3D interpretation environment with the photomosaic, georeferenced, and draped over. At this stage, all the data has been collected, processed and compiled, and ready to start phase 3.

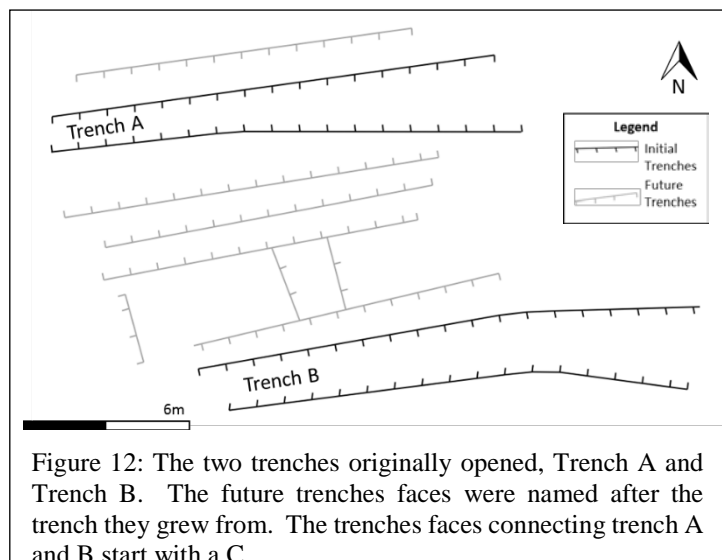
Phase 3 began when the trenches were prepared for interpretation. Bedding horizons and faults were the components of the fault zone that were interpreted. The range of scale on the features was quite broad, so the faults were methodically identified in a hierarchical manner. The largest structures (>1m) were interpreted first to identify the major independent fault blocks. Then, the structures confined inside the individual fault blocks (<1m) were identified. Lastly, the minor faults (cm sized) were interpreted.

Correlating the structures across the trench was completed by first identifying discontinuities on one trench, following it to and across the floor section, then up the next trench. This method was not possible on all trench faces mainly because not all surfaces intersected the floor or were unidentifiable in the floor's photo resolution. Some surfaces have a higher degree of uncertainty than others.

Once all the faults and horizons were interpreted, the fault sticks were joined using ordinary Kriging to create geologically accurate surfaces that fit the interpretations. The compilation of the surfaces and the resultant geological model can be used for further analyses (e.g. seismic and reservoir modeling). Each of these steps will be discussed in more detail in the following sections.

Field Work

Before we arrived to the location, the paleoseismology study that discovered this fault strand established the location for digging. In preparation for our arrival, the University of Alicante excavated and cleaned two preliminary trenches named Trench A and Trench B (Figure 12). The trenches built on later are named after the trench they were expanded from. To



open up the subsequent trenches, heavy machinery was brought onto the location where it would scrape away approximately 1 m of earth from the side of the trench thus expanding the

trench and exposing a new trench face. This was the most efficient way to remove the earth; it took up one hour to complete. Due to the size of the equipment, the precision at which the material was removed was low. One meter of earth removed was the goal; however, the actual amount was variable. Also, the arm on the equipment extended out only about half the distance of the trench. Therefore, the equipment was limited to working on one side at a time. It would scrape material on one side, then move to the opposite side and work. Consequently, the trench faces tended to bend, as demonstrated in Figure 12. However, this was accounted for in the final model, as the LiDar scans would capture this geometry. Once the excavator was finished, there was an exposed trench face approximately 4 meters high and 12 meters across. Four meters was the height limit, any deeper would compromise the stability of the trenches. When the excavator finished, the next step of cleaning and prepping the wall commenced.

Before the trench faces could be documented, they needed to be cleaned and prepped after the excavator. As the excavator open each new trench, it would smear the soft sediments and kick up dust that would coat the trench face hiding the rocks underneath. The first step was to clean the debris away using a hand scraper and removed the top 1-2 mm of the surface (Figure 13). This exposed the clear bedding and structures seen in the dataset.



Figure 13: The team working together to remove the debris from the fresh surface using hand tools.

The next step was setting up the grid. The grid used for this project was 1 m by 1 m cells. Four corner nails set into the trench face mark each cell. The nails were positioned using a meter long level for accuracy. Then, each nail was labeled with a two-digit coordinate to identify where on the trench face the nail is located. This is a vital step for reconstructing the photomosaics in the data processing phase. When the photomosaics were constructed, each photo could be scaled correctly. The result of this step was a clean trench with nails assigned

to an arbitrary coordinate system (Figure 14). Once this was completed, the trench was ready to be photographed.

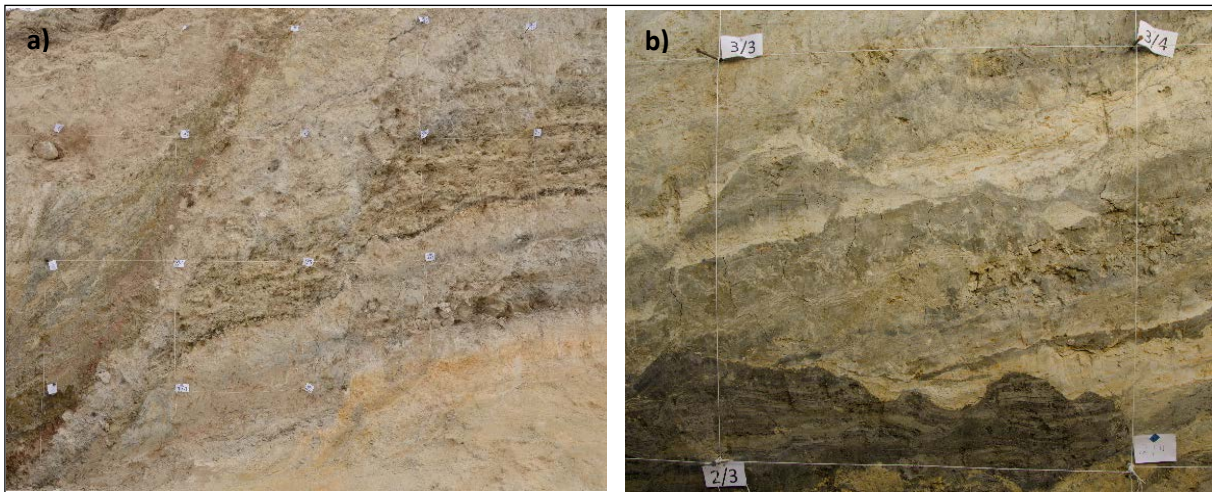


Figure 14: These pictures demonstrate the coordinate system that was set up on each grid face. (a) Shows the scale from a distance. Each nail has a piece of string tied around and pulled taut. (b) This is a single cell in the coordinate system marked with labels.

High-resolution photographs were taken of each trench after all the preparation work was completed. Each 1x1m cell was photographed at close range to maximize the resolution. Each photograph captured all four nails marking the corners of the cell. The pictures were taken as orthogonal to the trench face as possible to minimize the perspective distortion that is inevitably introduced. Every trench face was photographed using this method. At the end, there were about 350 photos to be processed.

The last step on each trench was completing the LiDar scan. Each trench was scanned from at least three different perspectives to ensure a full 3D view of each trench face. The University of Alicante provided and operated the LiDar equipment.

These were the methods used for documenting the vertical trench walls during the field campaign. When all the vertical trenches were finished, the floor section was the next step. The methods here were slightly different. To see the floor section, all the material needed to be completely removed from the trench. It took the excavator several hours to complete this, but the cleaning by hand took even longer. This process started during the first campaign and completed by another crew. Using hand tools, shovels and buckets, all the excess debris was removed. Once the floor was sufficiently clean, a drone was utilized to photograph the floor. The floor area was also scanned using the LiDar equipment for a complete dataset.

Trenching is a destructive process, meaning the subject of the study is destroyed during the data collection process. This is why a meticulous and detailed mentality for the duration of data collection is vital. There is only one chance to do it correctly. During the fieldwork for this project, accurate and careful notes, documentation, and data were collected. By the end of the field campaign, there was nearly a complete dataset. Missed data from the trenches were limited to locations too dangerous to photograph properly. These only occur on the margins of the trenches and have a minimal impact on the overall study. As soon as the field campaign was finished, the processing of the data began.

Data Processing

Upon returning from the trip, the next steps involved organizing the data, correcting distortions in the photographs, building the photomosaics, constructing the LiDar meshes, and draping the photos onto the meshes. The produce of these steps was a geometrically accurate reconstruction of the field excavation.

Before utilizing the photos, they needed to be corrected. The first correction was to remove distortions. Since this is largely a geometrical reconstruction, the amount of error introduced from photos should be minimized. Removing the lens distortion was the first correction applied to each photo. Due to the convex shape of the camera lens, the photo will have a barrel shaped distortion. The image has the greatest distortion on the margins where it appears to bulge or round. As light enters the lens, it passes through a curvature, which is greatest on the brims of the lens. As the curvature decreases towards the center, the distortion in the photo also decreases. Correcting this requires a sophisticated algorithm incorporated in the Adobe Photoshop platform. In camera raw mode, the lens and camera settings are hard coded in the image file. This lens information was used to remove the distortion introduced by the shape of the lens.

Orthorectification is the next adjustment. This removes the distortion from the perspective. Ideally, the photos should be taken orthogonal to the center of the subject. However, this is very difficult to do without specific instrumentation for measuring and adjusting the position and orientation of the camera. If the photo was taken looking in an upwards direction, the top of the photo would be stretched out relative to the bottom. Since every cell was measured to be

a perfect square, this distortion was relatively easy to remove. Again, this was done in Adobe Photoshop using the upright tool. To use this tool, lines are drawn on the photo that should be perpendicular, but are not in the image. In this project, the lines connecting the four nails that define the cell are digitized. Once the lines are drawn, the image is warped so each corner of the cell is a right angle. Figure 15 shows the initial photo, and then the same photo after both lens distortion and perspective distortion have been removed.

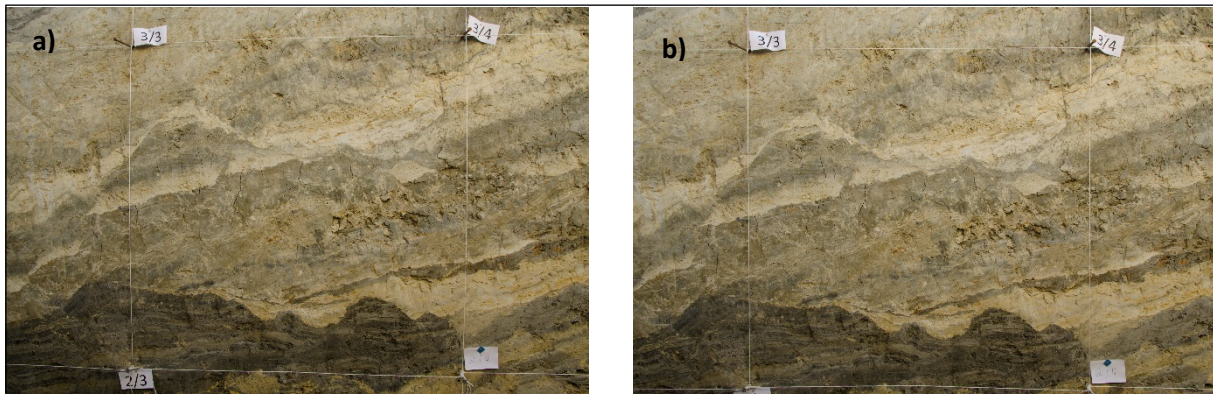


Figure 15: This is an example of the corrections applied to the photo. (a) Shows the original photo and (b) shows the same image after lens distortion has been removed and orthorectification has been applied.

After removing the distortion from all the photographs, they can be utilized to construct the photomosaics. I used the software Huggins (version 2016.2.0) to stitch the photos together. This software searches each photo for correlation and automatically identifies matching points. The photos are then knit together into a single cohesive image. The workflow for this process starts with first inputting the photos into the program. Then, the software runs an algorithm that finds matching points in each photo (Figure 16). Before executing the stitch, each photo connection must be checked and mismatches removed. Then the program will build a sample image illustrating how the final photo will appear. This also should be checked for accuracy. This process is repeated until the sample image contains no errors. If there are not enough matching points between two adjacent photos, working in smaller batches of photos works just as well. The last step before finalizing the photo is applying the color matching. Here, one can select an ‘anchor’ image, and the colors and exposure are adjusted on the rest of the photos to match that of the anchor. This process was repeated for all the trench faces.

When building photomosaics from photos taken from a surface that is not completely flat, parallax error is inherently introduced. Parallax error is the apparent displacement of an object

when viewed from two different perspectives. In this project, this a result of taking photos from different angles, capturing a single object from two perspectives. When the object is farther away from the subject, it will appear to move between the photos. The effect is more pronounced with increasing distance between the object and the subject. This is particularly problematic when the error exists where the two photos stitch together. The manifestation of this error affects mostly the objects that were placed on the trench face (e.g. nails, labels, jagged rocks, and concrete blocks placed on the top of the trenches). These objects appear to be either bent, stretched, or show up twice in the photomosaic. In order to completely fix this, distortion must be introduced elsewhere in the image. Since the accurate geometry of the subject is crucial to this study, the accuracy of protruding objects was sacrificed. Thus, this effect remains in the dataset.

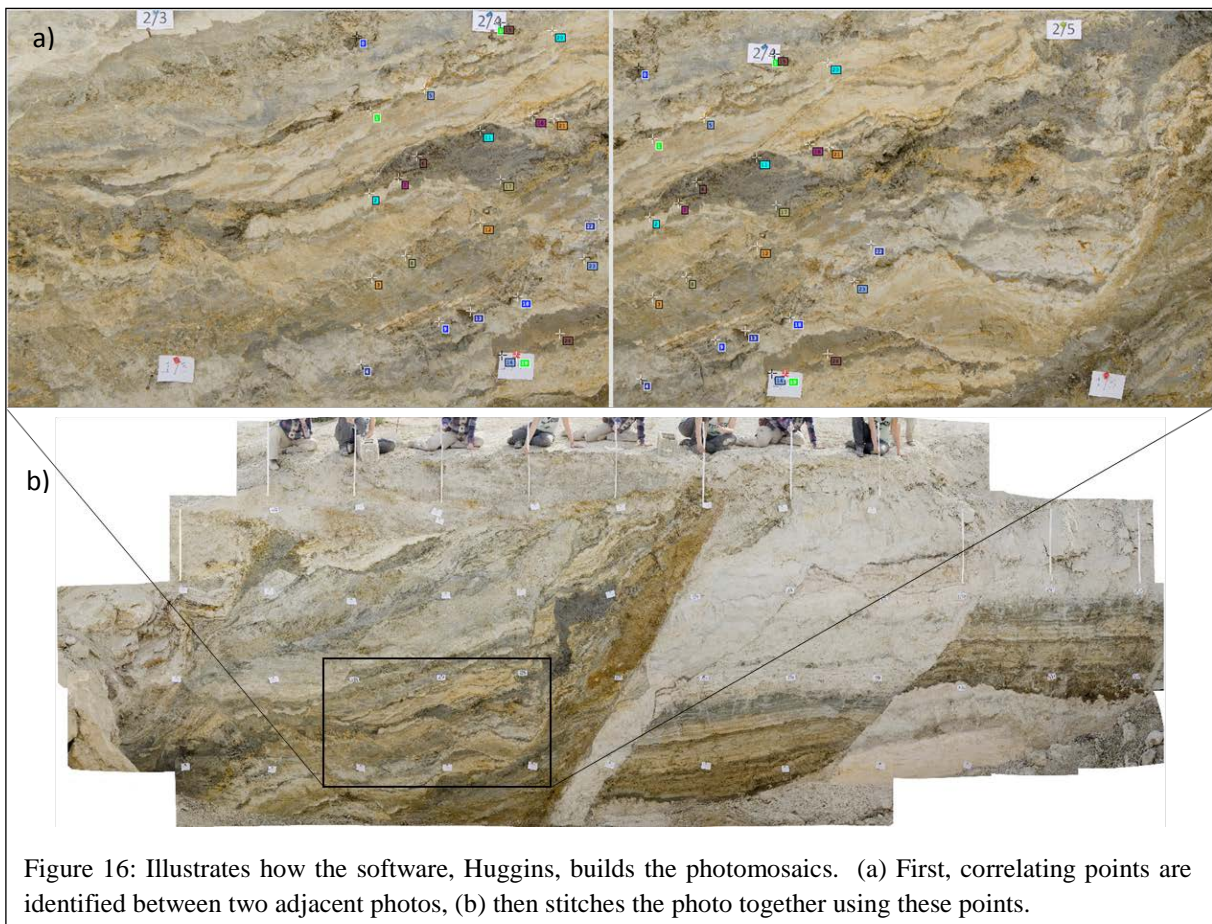


Figure 16: Illustrates how the software, Huggins, builds the photomosaics. (a) First, correlating points are identified between two adjacent photos, (b) then stitches the photo together using these points.

Another issue encountered in some photomosaics was shadows. The photos were taken periodically throughout the day. Naturally this introduced different shadows and affected the exposure in each photo. This can be removed in Adobe Photoshop by selecting the shaded area and adjusting the light balance to that area only. However, since the exposure can be drastically

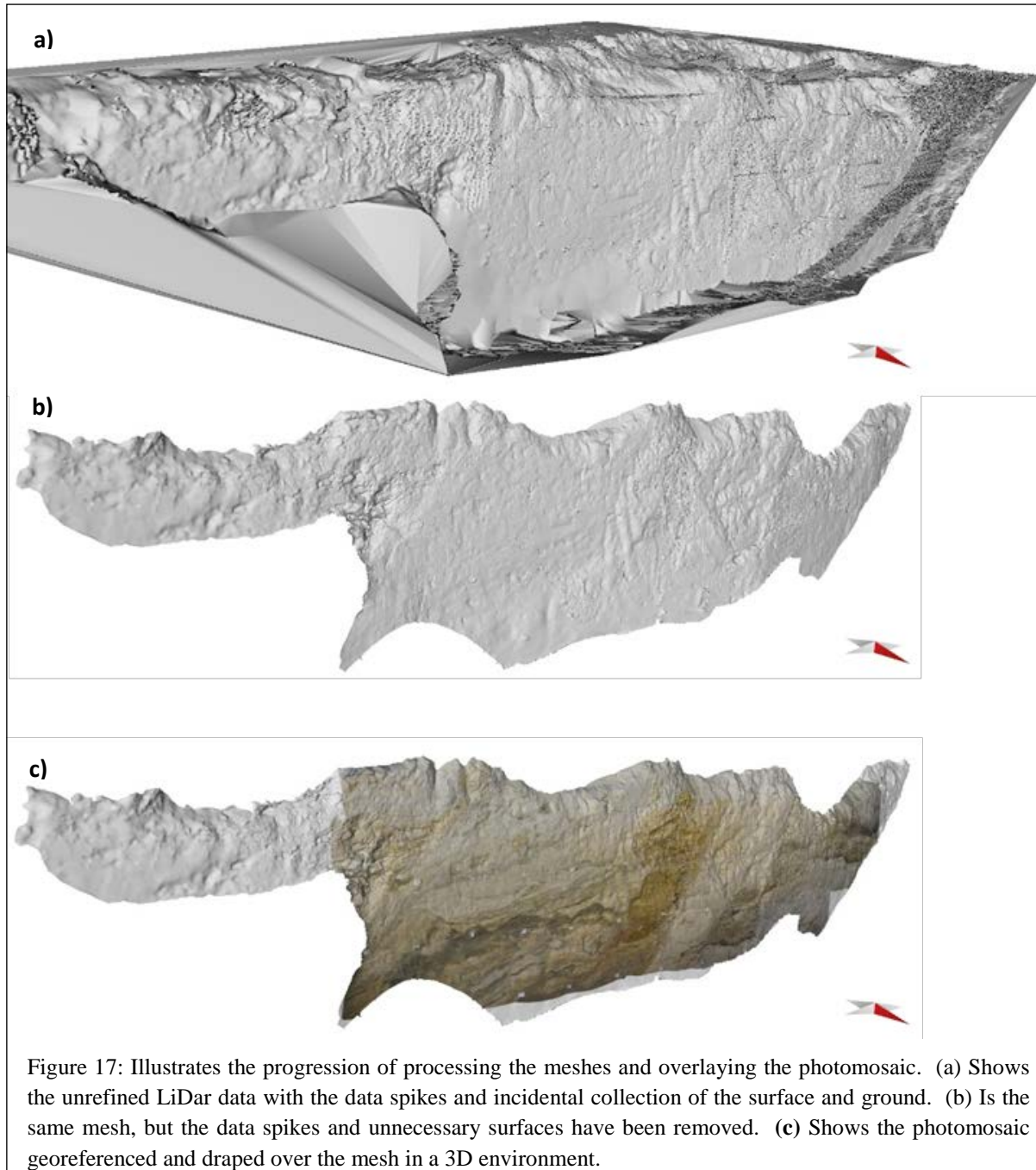
affected in the shade, it can be quite difficult to completely match the colors. In some places, the colors were only adjusted enough to clearly see the lithological boundaries, but the colors could not be matched to an adjacent photo. This was most prominent on the trench C1.

The next step in reconstructing the data is preparing the LiDar meshes. The University of Alicante conducted data acquisition and preliminary processing of the LiDar data. The LiDar data was acquired from a relatively rough surface with a great deal of interference caused by dust, falling debris, or even people walking in front of the subject during acquisition. This manifested in the data as sharp spikes in the meshes. To clean these spikes from the data, the points (.pts) file was opened in the software Move. Here, specific unwanted points were selected and deleted from the file. The area above the trench face and the floor, which were incidentally collected, could also be removed in this platform. This produced a relatively clean surface that also showed the location of nails as small protrusions, which were used later in the georeferencing step.

The progression of processing the meshes in 3D is shown below in Figure 17 for one of the trenches. Figure 17a shows the raw LiDar mesh imported from Move. The geodetics expert Benjamin Dolva at Uni CIPR (Center for Integrated Petroleum Research) in Bergen assisted in further removing unnecessary surfaces and spikes from the point clouds (processed mesh in Figure 17b). The process of draping the photomosaics over the processed meshes was quite difficult, but with the help from Simon Buckley at Uni CIPR, a solid workflow for georeferencing the photomosaics for display on the meshes in 3D was developed. The software used for this was LIME (LiDar Interpretation and Manipulation Environment). This software was chosen for the ability to interpret directly on the meshes, which is ideal for geometrical accuracy.

The workflow started with opening the meshes in the software as a 3D model. Then, a panel parallel to the trench was created and the image of the mesh was projected to it. This panel could then be extracted as an image file to be used in other software. In ArcGIS, both the panel image and the photomosaic image were opened and georeferenced. The photomosaic was then clipped to the extent of the panel image, which put both images were on the same arbitrary coordinate system. The photomosaic could now be added as a panel overlay in LIME and projected back onto the mesh. This was repeated for every individual trench face. Each overlay was completed in an individual LIME project to maintain reasonable file sizes. Once all

trenches were completed, the meshes with the overlays of each trench were brought into a single file by editing their project .xml files in a text editor. Figure 17c shows an example of the photomosaic georeferenced and overlain onto the mesh.



This is the final step for data processing. At this point, all the data collected in the field has been analyzed, corrected and compiled into one file that has the acquired data spatially referenced as accurately as possible. This was the most time consuming phase in this thesis. From here, the interpretation can start.

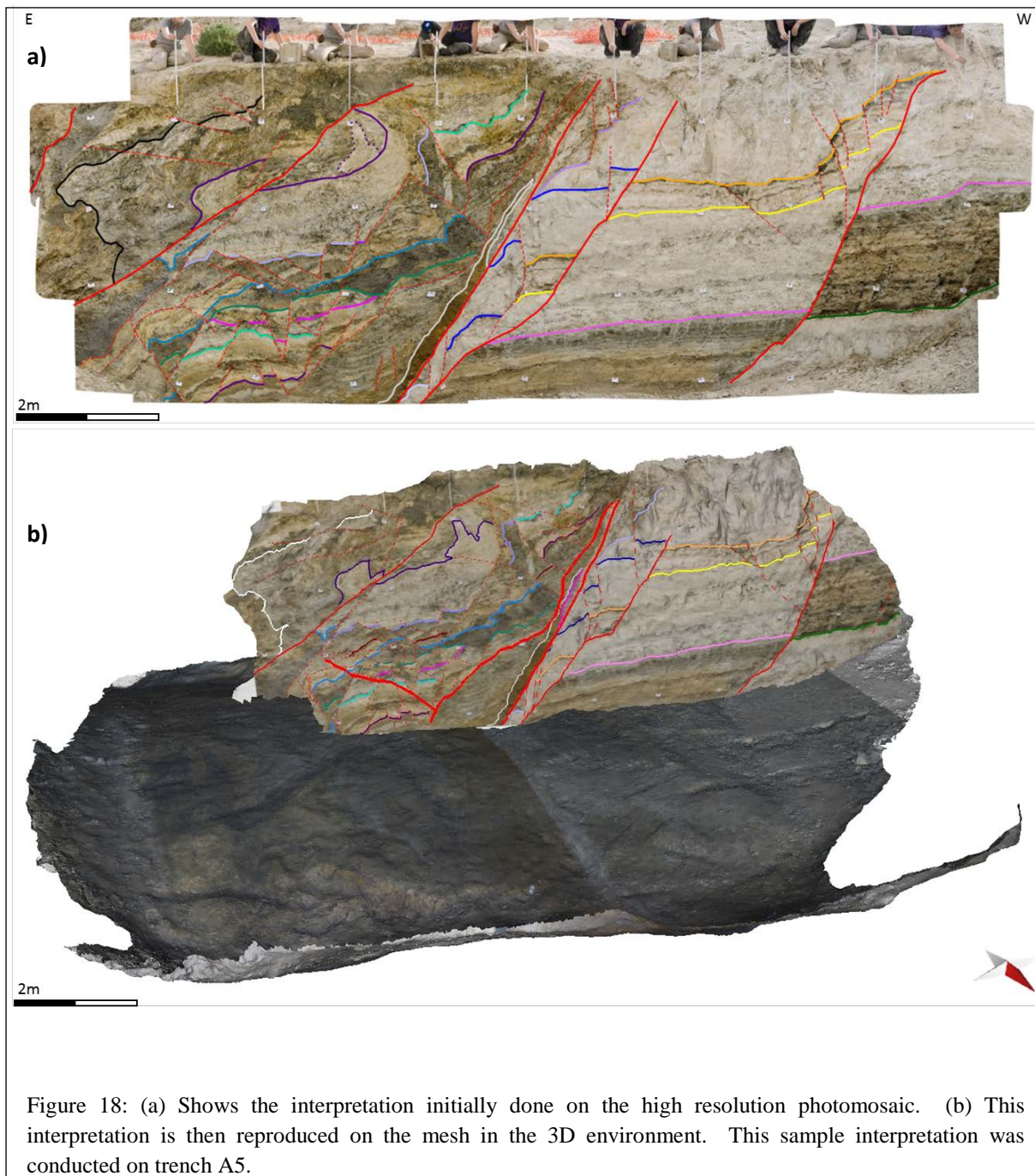
Interpretations

Phase 3 of this project is the interpretation of the dataset processed in phase 2. One drawback of the method previously discussed for draping the photomosaic over the LiDar mesh is that the resolution of the photomosaic undergoes a slight reduction in resolution. The file containing the photomosaic is a very large file (up to 200 MB) and must be optimized to function properly in the LIME platform. The consequences of this revision is that some of the smaller structures (cm sized or smaller) can become difficult to identify. To overcome this limitation, the interpretation were first conducted on the high-resolution photomosaics, then reproduced on the 3D meshes in LIME.

A hierarchical system was established to organize the interpretations. First, the largest structures were identified. These were classified as faults with larger than 1 meter offset, which bounded the major structural bodies. These structures were then correlated to the next trench by tracing the discontinuity down the floor, across the floor, and up the next trench. This ensured consistency and logic in the interpretation. Next, the smaller structures were interpreted. First, the bedding surfaces were identified by distinguishing features and traced until a discontinuity was reached. The discontinuity (or fault) was marked and the bedding trace was continued. Each bedding horizon was interpreted independently on each structure block. If the surface intersected the floor section, it was traced across the floor to the next trench. If there was no intersection, the bedding was correlated by identifying the same distinguishing features and adjacent structures. This was repeated on all the trenches. Then, the interpretations were reproduced in LIME on the LiDar meshes, which put the interpretations in a 3D context (Figure 18).

Difficulties in interpretations were primarily related to correlating across the trenches, especially when there was no apparent intersection with the floor. In some cases, even though there was an intersection, the reduced resolution from the drone photos made it difficult to differentiate between the different colors and identify the discontinuities. Also, smaller structures tend to have high variability along strike thus it was nearly impossible to correlate across greater than 1 meter distance between the trenches. Other difficulties related to the interpretation arose from the fact that many of the structures are not planar. The fluid injection structures have highly irregular geometries that change very rapidly depending on the

preexisting structure. This was also true with the clay smears and other various ductile deformation structures.

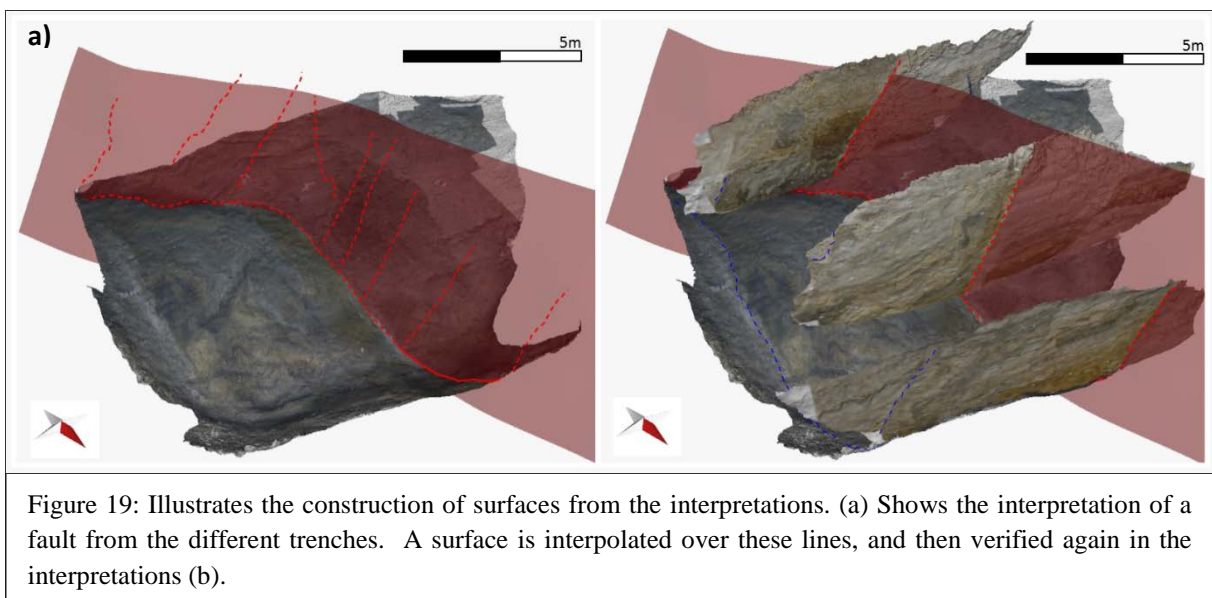


Once the interpretations were transposed into the 3D meshes, the data was then prepared for the 3D model construction. The next phase was to import the interpretation into Move to create the surfaces representing the interpretations.

Build Model

The software used for creating the faults and lithological boundaries surfaces was Move (version 2017.1). The interpretations completed in the previous phase were exported from LIME as ASCII files and then imported into Move. Then, a geostatistical interpolation algorithm generated the surfaces that constitute the stratigraphic horizons and fault surfaces in the model. Each surface was then reviewed for consistency and logic.

Surface construction for this project was facilitated by the ‘create a surface’ function available in Move. First, the interpretation lines for a particular surface were isolated and collected into the function. Then, using interpolation, a surface was generated to fit the data points. The interpolation method selected was ordinary Kriging. The distribution of data is uneven in this dataset. Areas with sparse or no data points need to be interpolated from the areas with dense data distribution. Ordinary Kriging was the chosen method because of its ability to interpolate smoothly over dense and sparse data distributions. This would generate a more geologically realistic surface compared to the triangulation methods. The interpolation grid was set to the inclination of the data, and resized to cover the entire study area. Anisotropy was activated and the default settings were used for constructing the variogram. The function was then executed using these parameters (Figure 19).



One issue from this method was that some of the surfaces pinched together over the data dense areas. This was introduced from interpreting on an uneven surface, the 3D LiDAR meshes. This

produced jagged lines that were used in interpolation. This was remedied by applying one iteration of the smoothing function in Move with a 0.5 m radius and a 50% ratio. This smoothed out the surface yet retained the uneven characteristic of the faults. However, this function is designed for gentle surfaces and it did not work well on the vertical fault surfaces. Therefore, the faults were rotated around the strike to the horizontal, smoothed, and finally returned back to their original orientation. In the end, the surface was a smooth, geologically realistic surface that fit the interpretations completed previously and populated the space where the data was sparse.

This method was repeated for all the faults and horizons over the study area. Many of the faults and all the horizons intersected another surface and needed to be split along this intersection. Since the Move software is designed for seismic scale study areas with surfaces covering kilometers, it did not function very well for this study, which exists on the centimeter scale. In order for the program to properly operate, the entire model was scaled to 100 times larger. This enabled the program's surface editing functions to work properly. The surfaces were then split along the intersections and trimmed to cohere to what the data suggested.

At the end of this phase of the project, there was a completed 3D model of the data collected from the Baza Fault. The process of collecting, processing, interpreting the data and constructing the model have concluded and the model is now available for further studies and analysis relating to internal structure and properties of a fault zone. The next section will be a detailed discussion on the dataset used for this project and the results that were gleamed.

DATASET

The raw data utilized for the reconstruction of the Baza Fault are the photographs and LiDar scans collected from the field as described in the methods section. A total of eleven trenches were excavated. These are all shown in a schematic trench map, Figure 20. Eight of the eleven sections strike east-west, which is approximately perpendicular to the strike of the fault. The other three sections strike north-south which is approximately parallel to the strike of the fault. Trenches A1-A5 are expansions of trench A and trenches B0-B3 are expansions of trench B. Trenches C1-C3, the north south striking trenches, connect trench A to trench B. The floor section spans the area between B3 in the south and A1 in the north.

Table 2 details the geometrical specifications for each individual trench. This includes information regarding the orientation of the trench face (using right hand rule), the size of the trench face in meters, and how many photographs were compiled in the photomosaic. The chart also includes a thumbnail of the photomosaic and LiDar scan.

Enlarged images of each photomosaic are included in Appendix A.

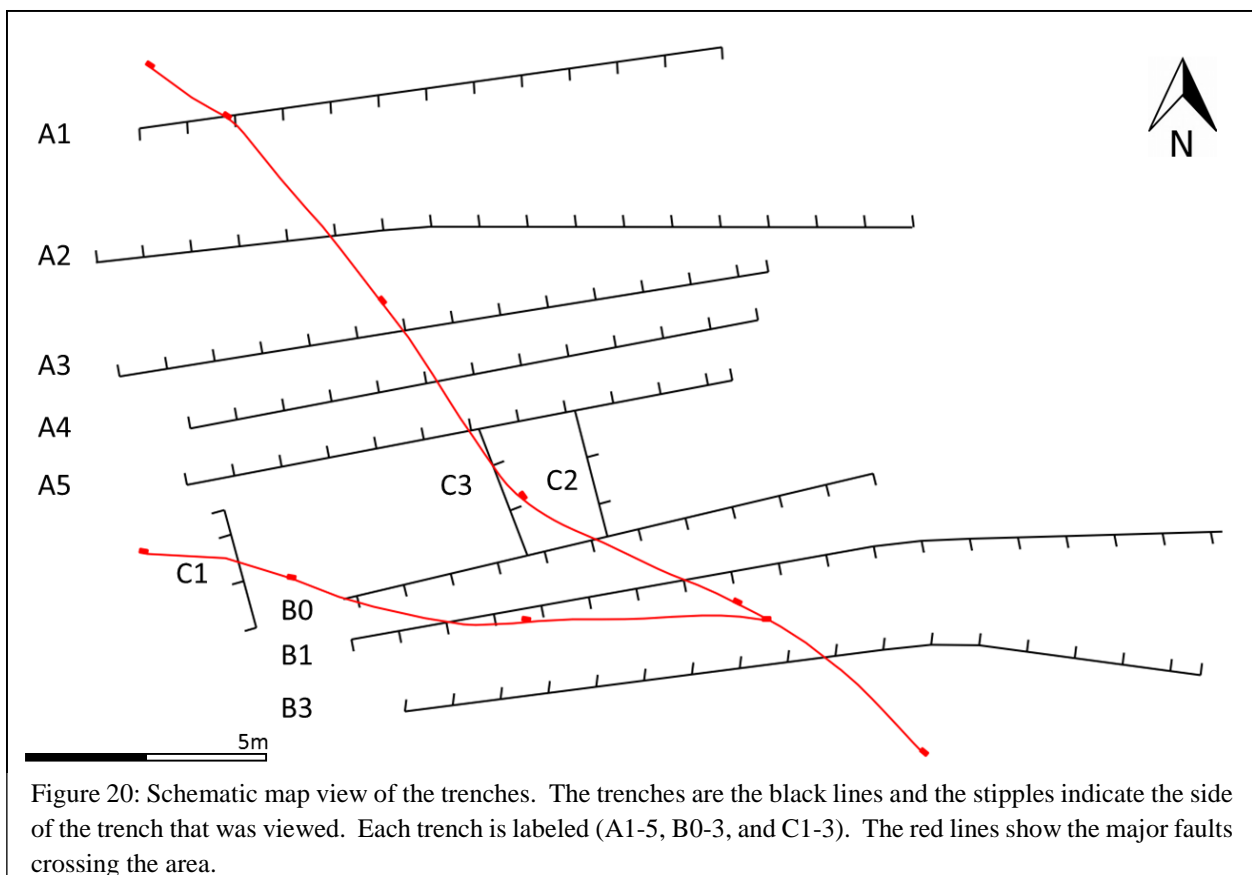






























Table 2: Description of the dataset.

Name	Orientation	Size (m)	Photos	Photomosaic	Lidar
A1	82°	9 x 3	34		
A2	163°	13 x 4	47		
A3	160°	12 x 4	51		
A4	159°	11 x 4	47		
A5	159°	11 x 4	39		
B0	76°	10 x 4	36		
B1	80°	11 x 4	35		
B3	162°	13 X 6	38		

Continues on next page.

Table 2 Continued

C1	165	3 x 3	8	N		S		
C2	345°	3 X 4	12	S		N		
C3	339°	3 x 4	9	S		N		
Floor	NA	13 x 12	NA					

OBSERVATIONS

Every trench was carefully studied to identify the lithological boundaries and structural components. The boundaries utilized for this interpretation were previously discussed in the geologic setting (Figure 10). Identifying these horizons was crucial to the interpretation because it established the sense of movement and cumulative offset along the faults. Each trench was divided into independent structural units, and then the horizons of each structural unit were determined. Lastly, the interpretations were correlated across trenches to determine a 3D context of the fault zone structure.

Lithologic Units

The stratigraphy of the fault zone is not only important to establish relative movement; it also provides insight into the mechanical behavior within the units. The description of each trench includes the offset of horizons by faults and how this offset varies between trenches. Along the main fault strand, the stratigraphy is completely different on either side. Thus, there is insufficient data to accurately measure the total offset of the fault zone. However, regional studies estimate the offset at 30m.

The horizons from the footwall stratigraphy are assigned alphabetic names beginning with AA. This is the stratigraphically lowest and oldest layer exposed in the trenches. Generally, the units that are found on the footwall (from AA-F, Figure 10) tend to have chalk to limestone composition with hard and crumbly texture yet fine grained, massive, and light colored with intermittent color changing laminations. These units could be related to the marginal facies of the Baza Formation associated to a palustrine depositional environment.

The layers on the hanging wall are named numerically beginning with -1. This is the lowest and oldest layer in the hanging wall stratigraphy. The subsequent layers numbered in order until horizon 10 (Figure 10). These lithological units tend to be finer, softer and have substantial water content. A reason for this difference could be related to the age and depth of these units. The younger hanging wall rocks are juxtaposed against the older, deeper buried rocks of the footwall. The footwall units have been exposed to a greater overburden and have likely undergone dewatering and compaction relative to the hanging wall units. These

differing sedimentological textures, lithologies, and rheological properties influence the structural style on each side of the core of the fault zone affecting the propensity towards brittle or ductile deformation.

Structural Units

The structural interpretation of the fault zone was done through a hierarchy. The highest order of faults marks the major structural units (S). These are defined as bodies of rock that move independently from the other structural units. They can also be correlated across multiple trenches and generally have a volume larger than 1 m³. These were identified first in the interpretation to establish the general structural framework. They will be individually discussed for each trench.

The minor structures are the second order of structures in the hierarchy. These are much smaller units occupying less than 1 m³. They are confined within the major structural units and are not correlatable between more than two trenches. Because of the small scale of these structures, many times they disappear or diverge into several faults between trenches. This makes them very difficult to correlate. These structures are identified in 2D only on the trench face interpretation. However, they are important for this study because they express the character of the deformation undergone in each structural unit.

There are also smaller faults that offset only one sedimentary layer. These are categorized as micro-structures. The displacement of these structures is usually less than 5 cm and always less than the thickness of the horizon offset. Due to their size, these structures are not always identifiable, thus are likely inconsistently interpreted. They are not used to characterize the structure of the fault zone, only to assist in the identification of the lithological units. As one looks closer and closer to the trenches, more and more faults can be interpreted. Even the folded structures are actually composed of hundreds of smaller faults. However, at some point the fault interpretation needs to stop. Faults with offset lower than 2 cm were not considered. The purpose of the structural unit hierarchy is to constrain the interpretations to the scope of the study.

Trench Descriptions

In this section, each trench will be described in detail. First the macro structural character will be described, followed by a comprehensive description of each of the structural units and changes that occur between the trenches. The discussion will include the lithologic units and their structural characteristics (hereafter referred to as S's). An arbitrary grid overlays each figure as a guide for locating objects. It is important to remember that the trenches are not perfectly perpendicular to fault strike. Therefore, the dips mentioned in the text are apparent dips. The discussion will begin with the northernmost trench A1 and moves southward. For the relative location of each trench please refer to the trench map (Figure 20).

Trench A1

The main fault strand on in the trench is labeled as Fault 0 on Figure 21. This fault separates the hanging wall and footwall stratigraphy. It dips 60° E and is one of two faults that are traced through the entire section. The footwall contains two major structural units divided by fault -1, which dips 42° E. The footwall unit farthest west is nearly cut off in this trench, but horizon A is visible in the top left corner of cell J0. This is S1. S2 is in the hanging wall of fault -1. This unit starts with horizon E and ends in horizon G. These beds dip gently eastward with progressively steeper dip up section. There is also evidence of clay smearing from this unit along fault 0 as seen in cell H1.

The first S in the hanging wall of fault 0 is S3. The lowest lithological unit here is the gravel from cell E0 to G0. The sequence continues to horizon 4, which is visible at the top of the section, between cells F3 and G3. S3 has substantially more brittle deformation, especially along horizon 1. This horizon is strewn with minor and micro conjugate normal faults along its length. The faults mostly accommodate small offsets, less than 10 cm. There is one large, low angle normal fault dividing the structural unit in half. This fault extends from cell H2 to E1, dips 27° E and cuts through the strata between horizon 2 and 3. This layer exhibits ductile deformation along this fault. Above this fault, the beds have undergone brittle deformation that is more concentrated on larger faults.

Fault 1 is the other very prominent feature traced through the entire study area. It is located from cell F3 through cell D0 dipping 52° E. This fault defines the western boundary of S4. S4

generally shows gently dipping bedding at 5° E. Cell E1 contains horizon 3 which overlays the lowest stratigraphic unit and continues up to horizon 7 in cells E3 and F3. Horizon 3 has the characteristic ductile deformation seen in the previous structural unit. This is likely a result of more plastic properties to the clay. The other sediments up to unit 7 appear to be relatively undeformed outside of the conjugate normal faults offsetting them. The layer above horizon 7 has been highly deformed.

S5 is the next unit to the east. It is cut off halfway up the trench by fault 8, which dips 40°E. S5 is in the hanging wall of fault 7, which dips 55°E in cells D2 and D1 becoming gentler in cell C0. Horizon 3 is the lowest horizon in S5 and the units below are a narrow band seen in cell C0. This unit is then overlain by horizons 4 and 5. All four of these lithological units have been deformed to very narrow strips. The plastic black unit occupies most of the space. It is a thick body near the top around cell D1, and then thins along a minor fault cutting this unit in two. The minor fault dips 62°E and is located from the bottom left corner of D2 to the center of C0.

S6 is in the hanging wall of Fault 8. The horizons within this unit are dipping 32°E, although horizons 8 and 9 exhibit ductile deformation. At the top of this S, the lithological boundaries become less apparent.

In the far west, there is S7. This unit appears consistent across all trenches as the light colored hard limestone lithological unit. The horizons fold upwards along Fault 10 forming drag folds. Moving away from the fault the horizons return to horizontal and apparently undisturbed.

Trench A1

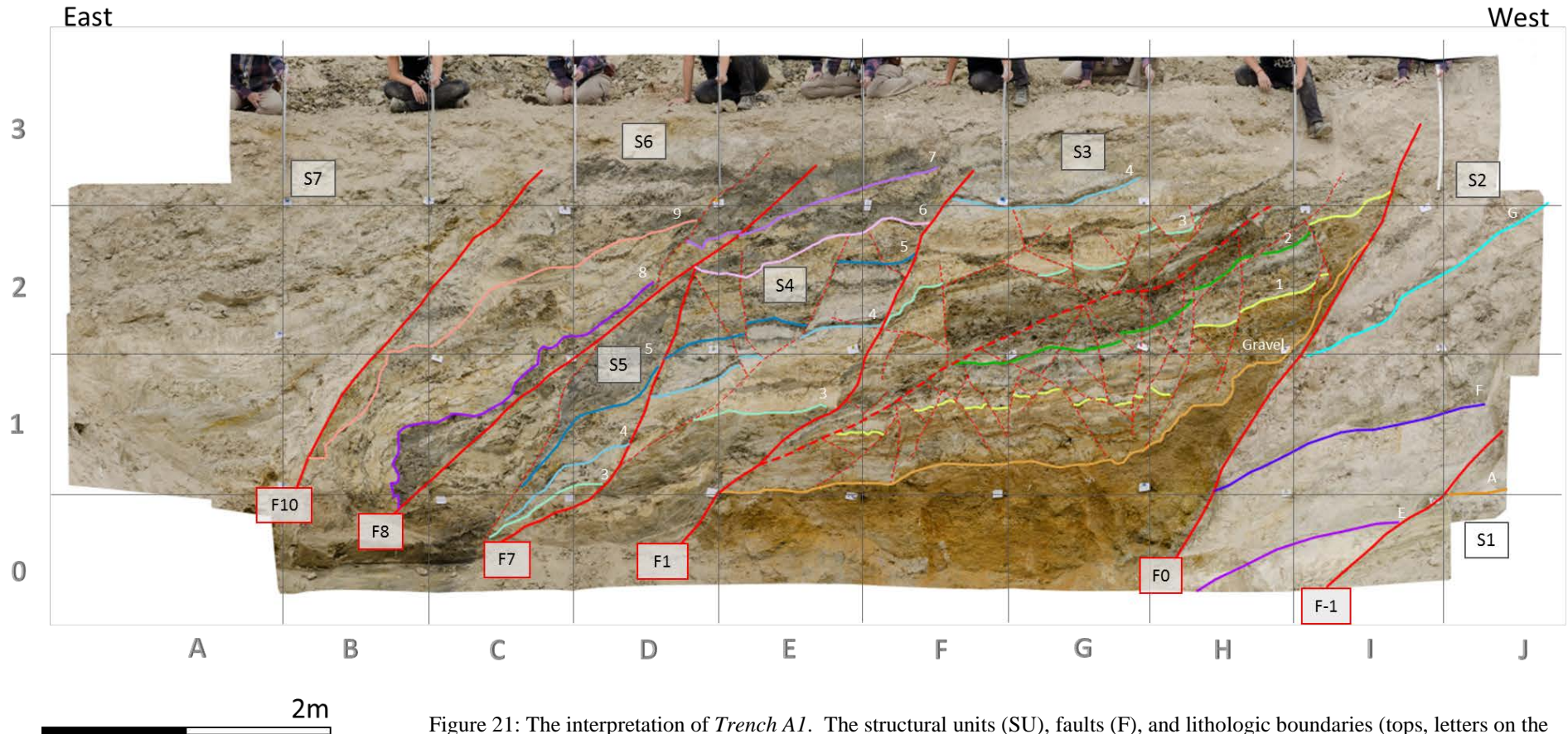


Figure 21: The interpretation of *Trench A1*. The structural units (SU), faults (F), and lithologic boundaries (tops, letters on the footwall and numbers on the hanging wall) have been labeled on the figure.

Trench A2

There are vast differences between trench A1 and trench A2. Most notably, the width of S3 has decreased, faults 7 and 8 disappear, and there is greater exposure of the footwall stratigraphy. Trench A2 was divided into 8 different S's. These are labeled accordingly in Figure 22. The majority of the faults identified in this trench dip eastward with an exception of faults 2 and 4. All the faults labeled represent the highest order in the structural hierarchy.

The major fault, F0 is located from cell I4 to G1 and dips 57°E, which is similar to the previous trench. The easternmost structural unit in the footwall is S0. This S contains a large normal fault running from cells L3 to K1 dipping 50° E and accommodates a considerable offset of 35 cm. Horizons AA to A are generally horizontal and undisturbed bedding surfaces. S0 and S1 are separated by fault -2 which dips 52°E (cells L2 to J1). There is approximately 1 meter off offset on this fault. The surface is quite irregular, curving westward in cell K3. Fault -1 extends from K3 to H1, dipping 46°E, which is gentler than the adjacent fault -2, thus decreasing the width of S1. The offset of this fault is about 3.5 m measured on horizon C. This is located on the hanging wall in cell H1 and the footwall at the top of cell K3. The last footwall S is S2. Here, the horizons are dipping steeper than the other horizons, up to 29°E. This change is likely due to the proximity to the fault 0, which has considerably more offset. This starts with horizon C and goes to horizon E. The total offset in the footwall section is 4.85 meter.

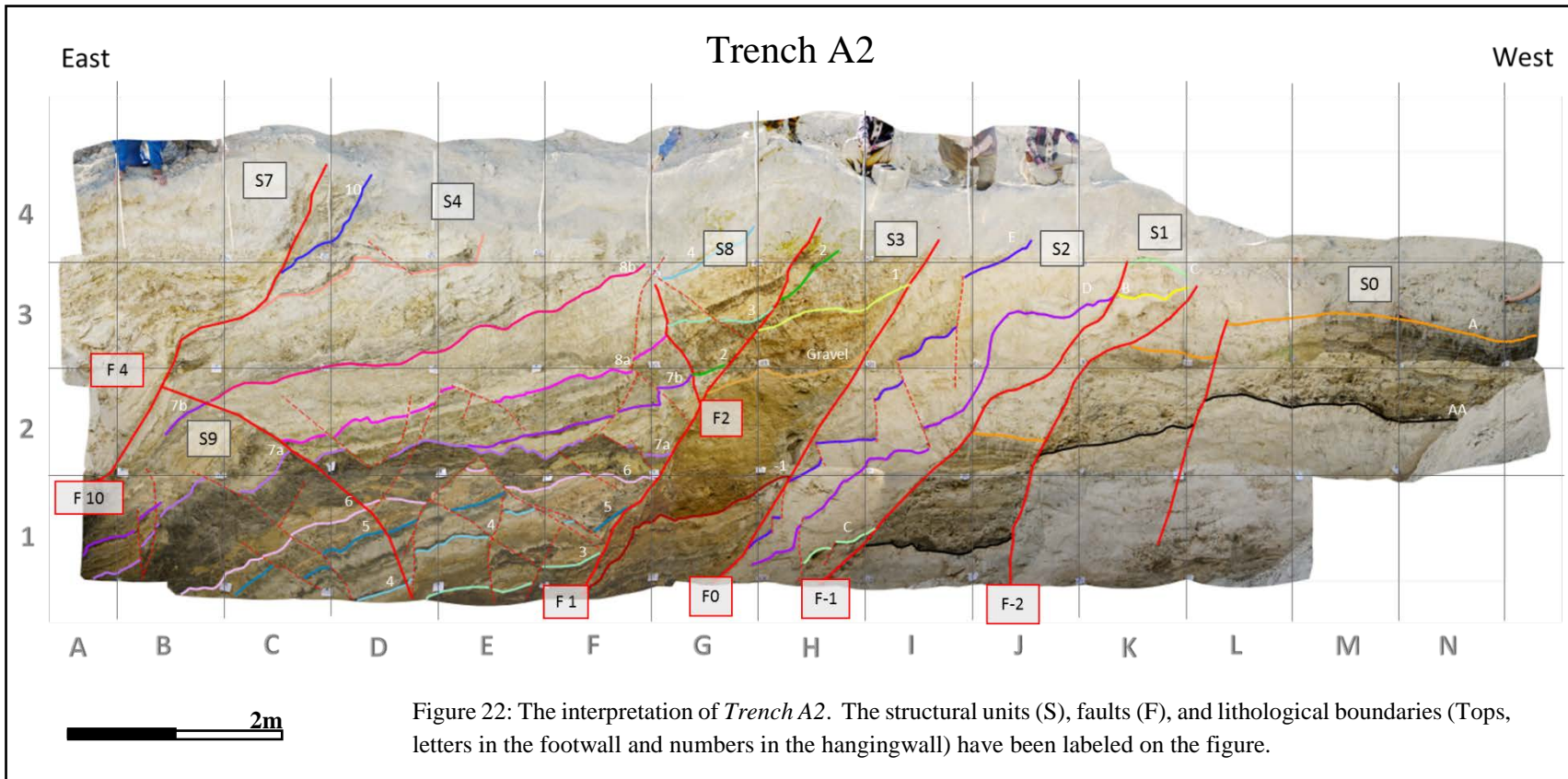
S3 lies in the hanging wall of fault 0. This structural unit starts with horizon -1 below the gravel, up through horizon 2 in cell H3. Within this structural unit, the beds are gently dipping about 10°E. There is also strong evidence of drag folds forming in the gravel unit, which are best seen in cell F1. Here, the gravel seems to be stretched along the fault plane. The next fault eastward is fault 1, which dips 57°E and runs from cells H4 to F1. Fault 1 dips steeper on this trench and it has an offset of about 3.8 m. This is estimated by projecting the thickness of the layer above horizon 2 which would be horizon 3. The offset is then calculated from that point to horizon 3 in the hanging wall in cell F1.

Above S3 closer to the surface is S8. This relatively small structural unit has been offset about 0.75 m from S3 along fault 1. S8 lies in the hanging wall of both faults 1 and 2 as a graben. Fault 2 is an antithetic fault dipping 34°W (cells G2 and G3). The lowest horizon in S8 is horizon 2 located in the top of cell G2, and ends with horizon 4 located in the top left corner of cell G3. The beds dip gently to the east.

S4 is in the largest structural unit in this trench. The horizons dip 13°E and are deformed by conjugate faults offsetting the minor structural blocks. The lowest stratigraphic horizon is horizon 3 located in the bottom of cell E1. The stratigraphy continues up through unit 10 located in the bottom right corner of cell C4. Brittle deformation is more prevalent in the bottom half than the top half. There are more faults in the bottom accommodating very little displacement. The highly deformed dark horizon 7b, is less deformed in this trench than seen previously

S9 begins to encroach into S4 behind fault 4. Fault 4 dips 43°W and starts in B2 and ends in D1. There are steeply dipping at 54°W beds in the bottom right corner of B2. The dips become less down section. In cell D1, the dip is only 13°W. This change could possibly be a consequence of internal faults progressively rotating the beds. Those on the outer edge of the rotation have been affected more than those closer to the center of rotation. The lithological horizons in this section begin with horizon 4 in cell D1 and continue through horizon 7b in cell B2. There is a dramatic thickness change between horizons 7a and 7b.

The easternmost unit S7 is the continuation of that identified in trench A1, lying in the hanging wall of fault 10. Fault 10 dips about 68°E and runs from cells C4 to A1. Again, the bedding here is relatively undeformed. There are breached drag folds just above fault 10, but the bedding returns to horizontal just meters away. The fault is developing a curve seen in cells B3 and C3 around a much harder limestone layer. Overall, there is much less ductile deformation in trench A2 than in trench A1.



Trench A3

There are many similarities between trench A3 and trench A2. On trench A3, most of the faults dip to the east (Figure 23). S3 narrows even more from the previous trench and S10 and S11 appear for the first time in the hanging wall.

Fault 0 again divides the trench into two, it starts in cell H5 and ends in F1, dipping 61°E . There are no significant changes in S1 and S0 from the previous trench. There is a small normal fault in cell I4 offsetting horizon C just under 20 cm. Fault -2 offsets S0 and S1 about 1 meter and dips 56°E (cell K4 to I1). Fault -1 dips 54°E and is located from cell I5 to cell F1 with an uneven surface similar to the previous trench. S2 begins from horizon C located in the top center of cell G2 through horizon E located in the top half of cell H4. These units are offset by a series of steeply dipping normal faults. The deformation here is much more prevalent than in S0 and S1. This is likely related to the proximity to fault 0.

S3 begins with horizon -1 and continues through horizon 1 located in the bottom of cell G5 dipping 34°E . This S is narrower than previously seen with a higher degree of internal deformation. It is offset by a series of eastward dipping normal faults. There is some ductile deformation both above and below the gravel unit, although it is likely that it exists in the gravel unit as well. S8 appears again at the top of S3, separated by fault 1. The lithological units are from horizon -1 to horizon 1. The east fault on S8 is fault 2, which dips about 78°W and extends from cell F5 to cell G4.

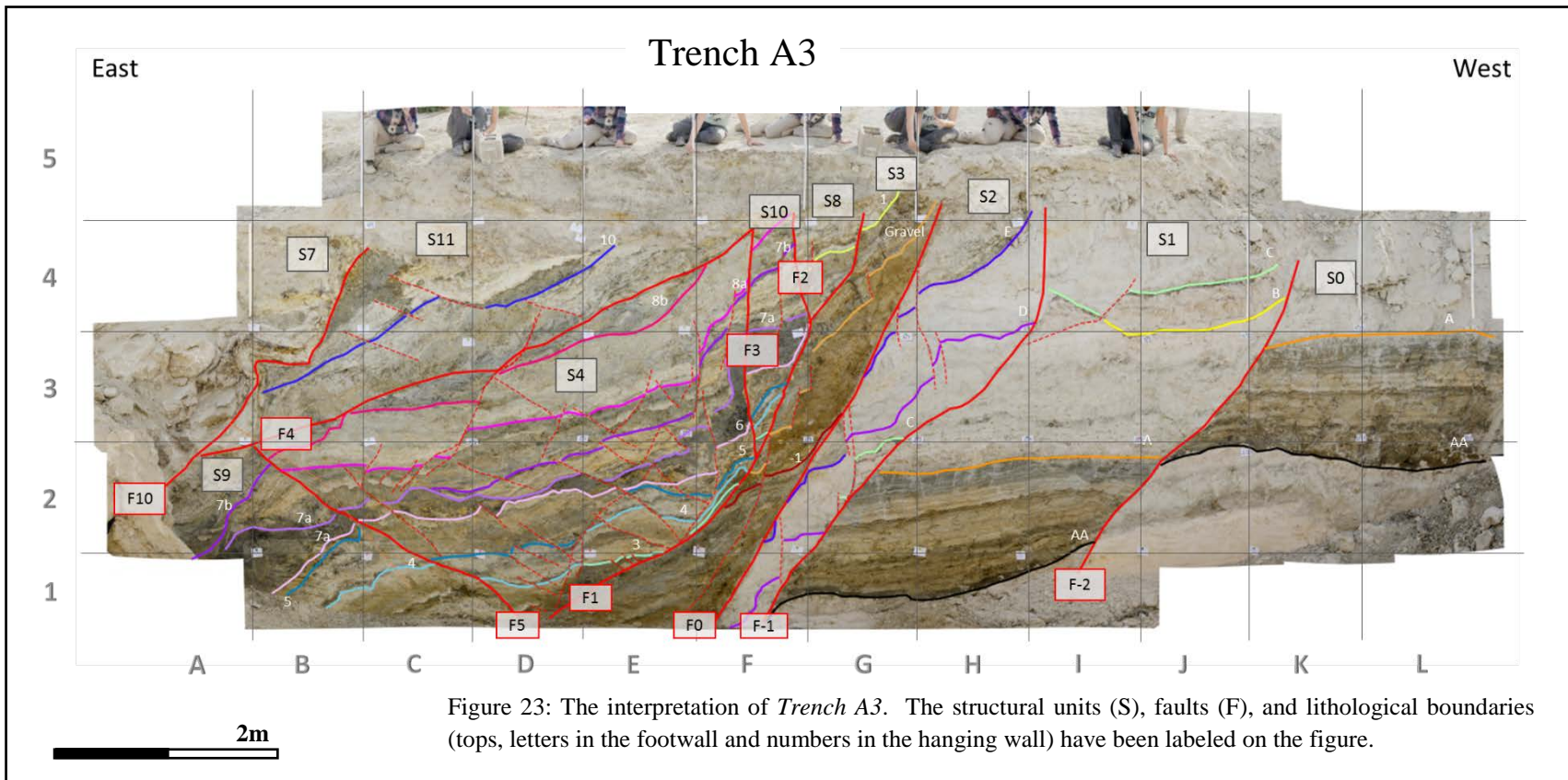
S10 is a new structural unit bounded by fault 2 in the west and fault 3 in the east. Fault 3 is a normal fault dipping steeply 83°W . It extends from cell F4 and ends on fault 1 where it connects in cell F2. The lowest horizon in S10 is the highly deformed horizon 3, which is barely visible in cell F2. The next horizons, 4, 5, and 6, are also very narrow bands that end with a fairly thick dark horizon 7. The beds are dipping 34°E .

S4 has the same characteristics as in the previous trenches. It lies in the hanging wall of two conjugate normal faults, fault 1 and fault 5. Fault 5 dips 41°W and is located from cell A3 to cell D1. The lowest horizon is horizon 4 located in cell D1. It continues to horizon 8 below the contact

with fault 4. There is significant low angle normal faulting in the lower half of the S where the two bounding faults approach each other. There is brittle deformation in the lower units and more plastic behavior in the upper units.

Fault 5 separates S9 from S4. S9 is also in the footwall of fault 10, which dips about 50°E. This is significantly gentler than in trench A2, which was measured to be 68°E. Fault 10 is located from cell B4 down to cell A1. The curving of the fault surface is more prominent here than in the previous trenches. The horizons in S9 dip 37°E.

S11 is a new structural unit in this trench. From the geometry of the fault, it is likely in trench A2 as well, but it was not observed there. It could have been obscured by layers dipping the same as the fault. In this trench, it lies over both S9 and S4. It is separated from S4 by fault 4, a low angle normal fault dipping 21°E. Fault 4 starts in cell F4 and ends in cell A2 where it stops at fault 10. This fault cuts and offsets the layers under horizon 9. Horizon 10 has been significantly offset (0.5 m) by a low angle normal fault located in cell C4. This area has a pattern of low angle faults with higher displacements compared to those in S4. This is a fairly consistent pattern across all trenches. The last structural unit is S7, on the hanging wall of fault 10. Here the curving of the fault surface is even more prominent than in the trenches.



Trench A4

There is roughly 1 m between trenches A3, A4, and A5. The interpretations and correlations between these trenches are very reliable. The major difference between A3 and A4 is that S0 becomes more prominent.

The westernmost structural unit is S0, which is unchanged from the previous occurrence except that it is much more exposed. S0 and S1 begin with horizon AA at the base and only go to horizon C. Fault 2 which separates S0 and S1, is located from cell K5 to cell I1, dipping 60°E and offsetting the horizons about 1 m. In cell K4, the fault curves to the east. It is difficult to understand why because the trench ends shortly afterwards. It could be because there is an obstacle deflecting the fault surface. The bedding remains relatively horizontal and undisturbed. Fault -1 is located from cell I5 to F1 dipping 47°E.

In S2, the beds remain relatively horizontal and offset by a series of steeply dipping normal faults with offsets 5 to 20 cm. Horizon 3 thins eastward likely due to the proximity to fault 0. Fault 0 is located from cell H5 and ends in cell F1 dipping about 51°E.

In S3, the gravel unit appears as a narrow strip from cell F1 to cell F2 overlain by horizon 1. S3 appears more deformed in this trench than previously seen, especially near the top when the thickness of the unit is at its narrowest. Faults 0 and 1 come very close and almost join. There is no identifiable structure in the core of the fault at this point. Fault 1 is located from cell H5 to cell F1, very close to fault 0. This fault surface is more irregular as it progresses north.

Horizons within S8 have a gentle dip of 24°W in otherwise undisturbed stratigraphy. S8 lies in the hanging wall of both faults 1 and 2. Fault 2 is located from cells F5 to G4 dipping steeply at 75°W.

Moving southward, the offset of S10 decreases indicating the proximity of the fault 2 tip line. S10 is bound by faults 1, 2 and 3. It lies in above fault 3, which is located from cell F4 to cell F3, dipping 68°E in cell F4.

S4 begins with horizon 4 in the bottom right corner of cell E2, and continues through horizon 8b along the boundary with S11. This S contains westward steeply dipping faults near the

bottom where the two bounding faults 1 and 5 approach each other. The upper section contains more ductile deformation. Fault 5 extends from cell C3 to cell E1 dipping 26°W . The horizons are gently dipping at 21°E with less deformation than previously seen. The degree of deformation in this block is decreasing as we move southward. This is different from the other blocks which are increasing in deformation to the south.

S9 lies in the footwall of fault 5. The beds in this section have been offset by another fault with significant displacement. This fault is located from cell B2 to cell B1 dipping 58°W . The horizons dip 11°E in the hanging wall of this minor fault and change to 40° on the footwall with approximately 60 cm of offset. There also appears to be significant rotation on the footwall of this block. This fault could potentially be a defining major structural block, however it was not correlatable between the trenches and thus remained categorized as a minor structural feature.

S11, which lies above S4, is bound by faults 10 and 4. Fault 4 is located from cell F5 to cell A1 dipping 22°E . This block contains horizons 9 dipping 20°E . There is one major fault located in cell C4, which offsets horizon 9. This offset is measured to be about 30 cm, which is a significant decrease from the fault noted in trench A3. The injection structure from horizon 9 becomes more prominent. It is located from cell B3 to B4 and C4. Here, it intrudes farther onto the underlying layers.

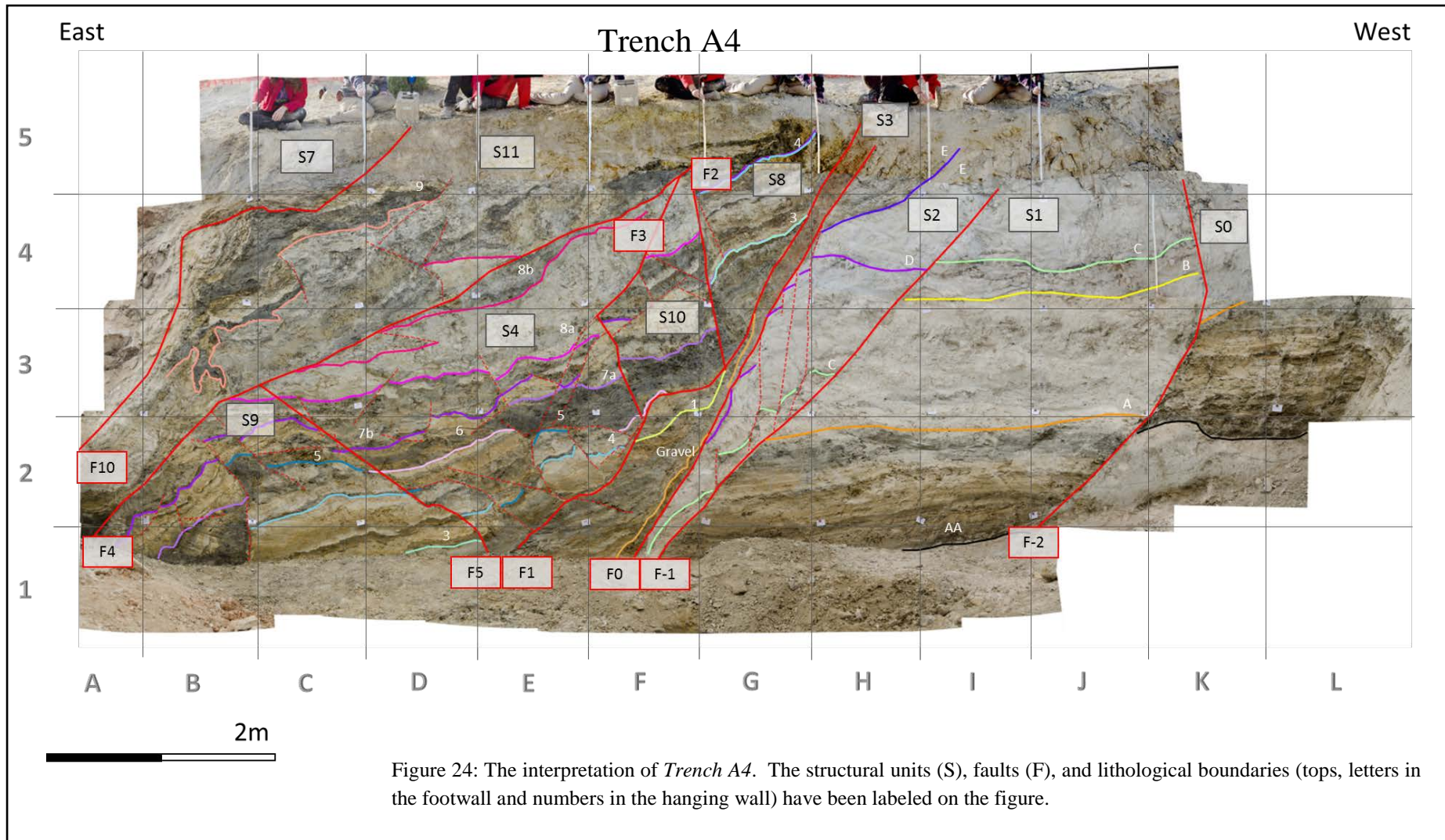


Figure 24: The interpretation of *Trench A4*. The structural units (S), faults (F), and lithological boundaries (tops, letters in the footwall and numbers in the hanging wall) have been labeled on the figure.

Trench A5

S0 and S1 have the same characteristics as previously discussed. The lithological units remain nearly horizontal, and are divided by fault -2. Fault -2 is located from cell K4 to cell I1, dipping 56°E. In S1, there is a series of westward dipping normal faults offsetting horizons C and D. These have small offsets, less than 5 cm. However, the combined offset between the faults and rotation of the blocks sums to nearly 1 m.

Fault -1 is located from cell H4 to cell E1, dipping 49°E. This fault marks the western boundary of S2, which contains horizons B to F. Again, horizon E appears to thin dramatically as it approaches the east-bounding fault. The internal beds generally are horizontal. Fault 0 is located from cell G4 to cell E1 dipping 57°E.

S3 is again narrow because the two faults, 0 and 1 are nearly joining. Fault 1 is located from cell G4 to D1 dipping 53°E. The lowest horizon in S3 is the gravel unit and horizon 1. The deformation has again increased from the previous trench.

S8, which lies on top of S4 contains horizon 3 and 4, which are dipping 43°E. S8 is bound to the east by the westward dipping fault 2 that is located from cell F5 to cell G3 dipping 51°W. This is significantly shallower than in the previous trenches. Again, there appears to be no major internal deformation in this zone.

The next structural unit is S4, which has been continuous across all the major structural units. S4 is bound by 4 faults, fault 1, 3, 4 and 5. Fault 5 is located in cell B1 dipping 59°W. S4 contains horizons 3 to 9 where it is cutoff by fault 4. There appears to be more high-angle brittle deformation in the lower part of S4, compared to the more ductile deformation above. Most of the faults offsetting the horizons here have no more displacement than a few centimeters. The black, ductility deformed horizon 7, has varying bed thickness indicating mobilization.

S9 lies underneath S4. This unit consists of horizons 7b through horizon 9. Here the beds have been rotated to dip about 45°E. This unit is bound to the east by fault 4, which is located from cell E4 to cell A1 and dips 33°E.

S11 lies above S4 and S9 and is bound by the shallow dipping fault 4 below and fault 10 above. Fault 10 is barely visible in this trench. It is located in cell A3. S11 contains horizons 9 and 10. Most of the deformation occurring here is associated with the ductile deformation and the prominent injection structure located in the top right corner of cell A2.

The next trenches that will be discussed are trench series B. These have significantly different structural components because of their larger distance from trench series A.

Trench A5

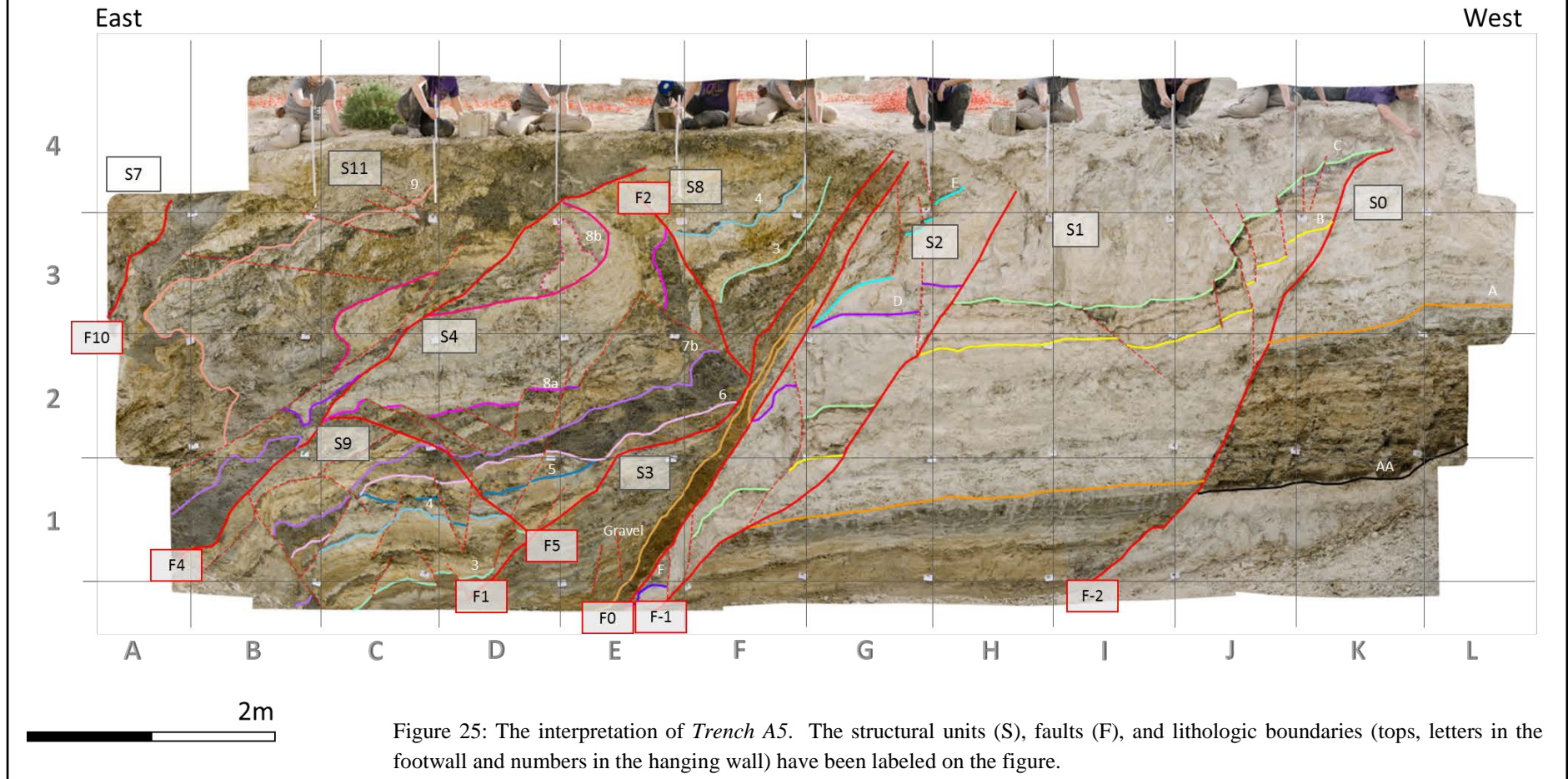


Figure 25: The interpretation of *Trench A5*. The structural units (S), faults (F), and lithologic boundaries (tops, letters in the footwall and numbers in the hanging wall) have been labeled on the figure.

Trench B0

The structural units in the B trenches are similar to those from the A trenches. In trench B0, there are S0, 1, 2, 3, 7, 9 and 11 (Figure 26).

S0 and S1 are similar to those seen previously. They contain the horizons A through C and are separated by fault -2 (cell K5 to I3) which dips 54°E. Fault -1 is located from cell I5 to cell E1 dipping 50°E.

In S2, the beds are relatively horizontal with the typical thinning of unit E as seen in G4. Some minor faults dipping 59° E in cells E1 and E2 offset the lower part of S2. This unit is bound on the east side by fault 0, which extends from cell D5 to cell D1 and dips 62°E.

S3 is in the hanging wall of fault 0. This unit contains horizons -1 to 3. The beds here dip 28°E, and are relatively undisturbed. Fault 1 is located from cell D4 to cell D1 and has quite an irregular shape, bulging around the gravel unit as seen in D2 and D3. S8 is not present in this trench, nor any of the following.

S11 is bound by faults 1 and 10. Horizons 8 and 9 are within this unit and are quite chaotic. There was significantly less moisture in this trench, which makes more difficult the interpretation of the structures. In S11 there is mostly ductile deformation and a clear injection structure in cells D3 and D4.

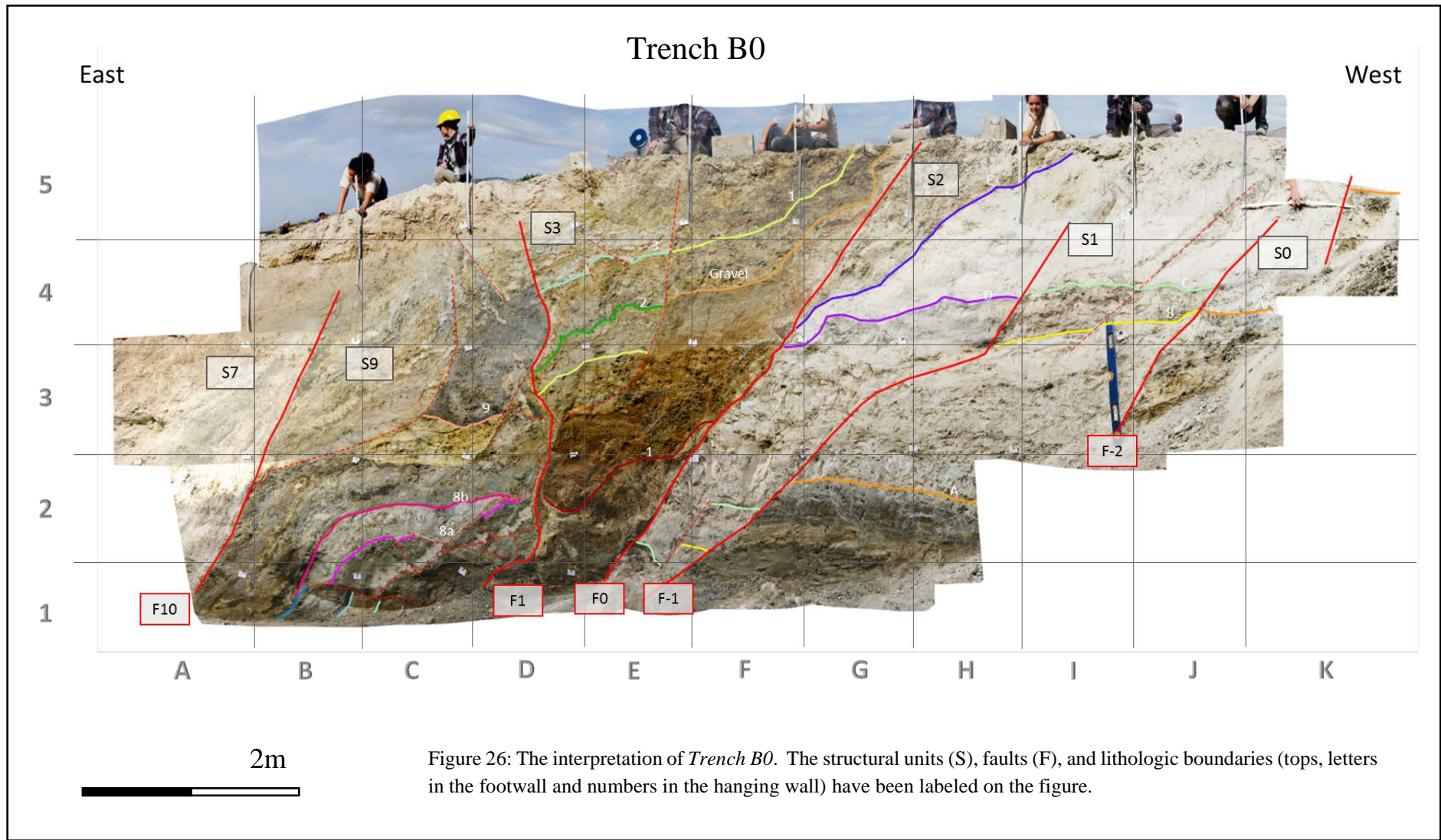


Figure 26: The interpretation of *Trench B0*. The structural units (S), faults (F), and lithologic boundaries (tops, letters in the footwall and numbers in the hanging wall) have been labeled on the figure.

Trench B1

Trench B1 has much fewer visible lithological boundaries. For instance, inside S9 it is almost impossible to identify lithological boundaries. This area has been highly subject to internal deformation and the faults are approaching each other. When this occurs, there is less volume to distribute the deformation, thus it becomes concentrated. This trench has been divided into 8 different structural units, and the first appearance of S12, which is on the footwall of fault -3.

The first structural unit to the west is the new unit S12 associated with fault -3. The beds here are the same stratigraphy and generally the same structure that was seen previously in S0 and S1. The sequence begins with the horizons from AA through C. The fault appears to splay in cell J1 to create two separate faults and a lens of material between them. The dip of fault 3 is about 56°E and is located from cell L4 through cell J1. Fault -1 is in cells G3 to E1 dipping 52°E. Fault -1 is now connecting with the next fault, fault 0.

S2 is in the hanging wall of fault -1. The lithology is highly deformed and the horizons units are indiscernible. This is a very narrow structural unit highly affected by fault 0. Fault 0 is located from cell H4 to cell D1 dipping 43°E. The surface is slightly uneven as shown in cell E2.

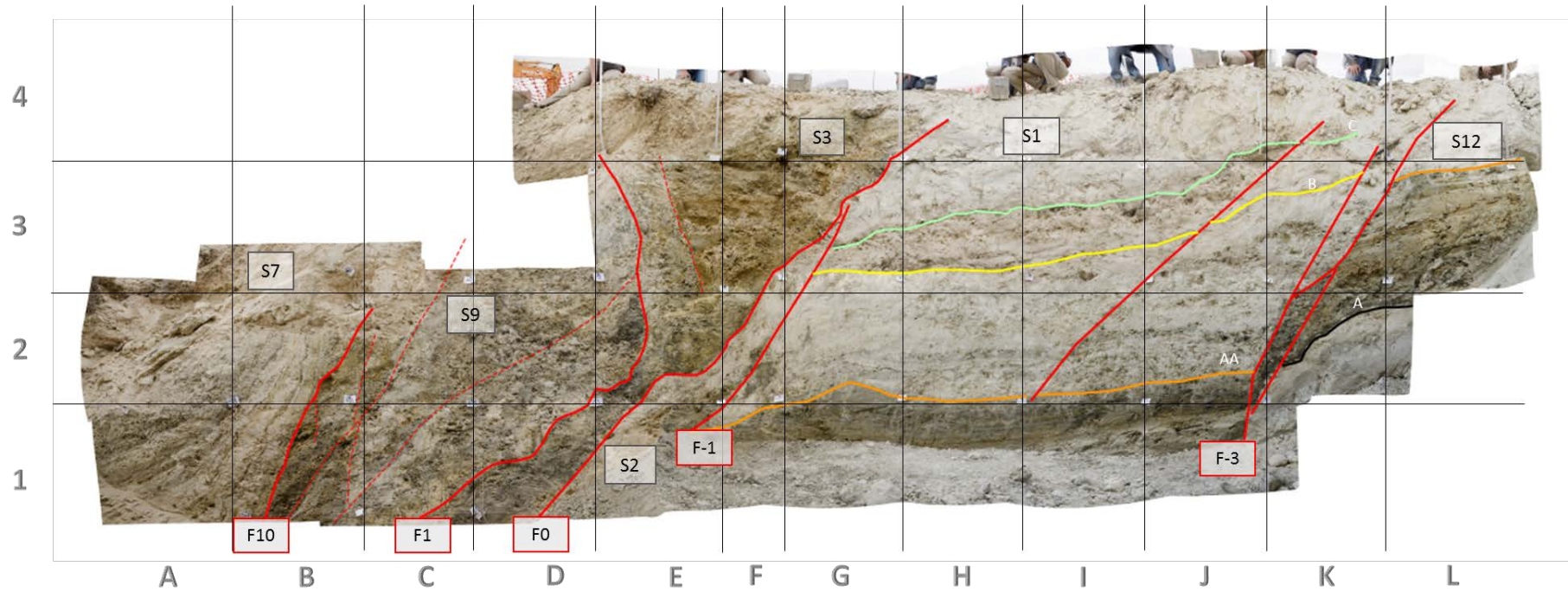
S3 lies in the hanging wall of fault 0. The shape of S3 is similar to the previous trench with a very wide area at the top slimming towards the bottom. The material in this unit is also highly deformed with indiscernible horizons. The gravel unit is found in near the top (cell F3) and horizon -1 occupies the lower part. The fault that bounds this unit to the east is fault 1, which has a more uneven surface.

The next structural unit is S9. This unit looks much different and more narrow than in the other trenches. The internal structure is too chaotic to identify horizons. There is mostly ductile deformation that deformed this unit beyond recognition.

Trench B1

East

West



2m

Figure 27: The interpretation of *Trench B1*. The structural units (S), faults (F), and lithologic boundaries (tops, letters in the footwall and numbers in the hanging wall) have been labeled on the figure.

Trench B3

As we move from trench B1 to B3, it is clear the fault zone is narrowing, as faults 10 and 0 are less than a meter apart. This is best seen in in cell E1. In this area, the structural units may still present but so close together and deformed that they are difficult to differentiate. The horizons in S12 remain the same, horizontal with exposure of horizon AA up to horizon C. As we approach the very narrow region, which is likely composed of C through E in the hanging wall of fault 1, there is S11 where the material has been mixed to the point where the faults can no longer be identified.

Fault 10 marks a very clear boundary between S9 and S7 dipping about 58°E and deforming the rocks of S7. B3 is the northernmost trench.

The next interpretations will briefly discuss the north-south facing trenches **C1, C2 and C3**.

Trench B3

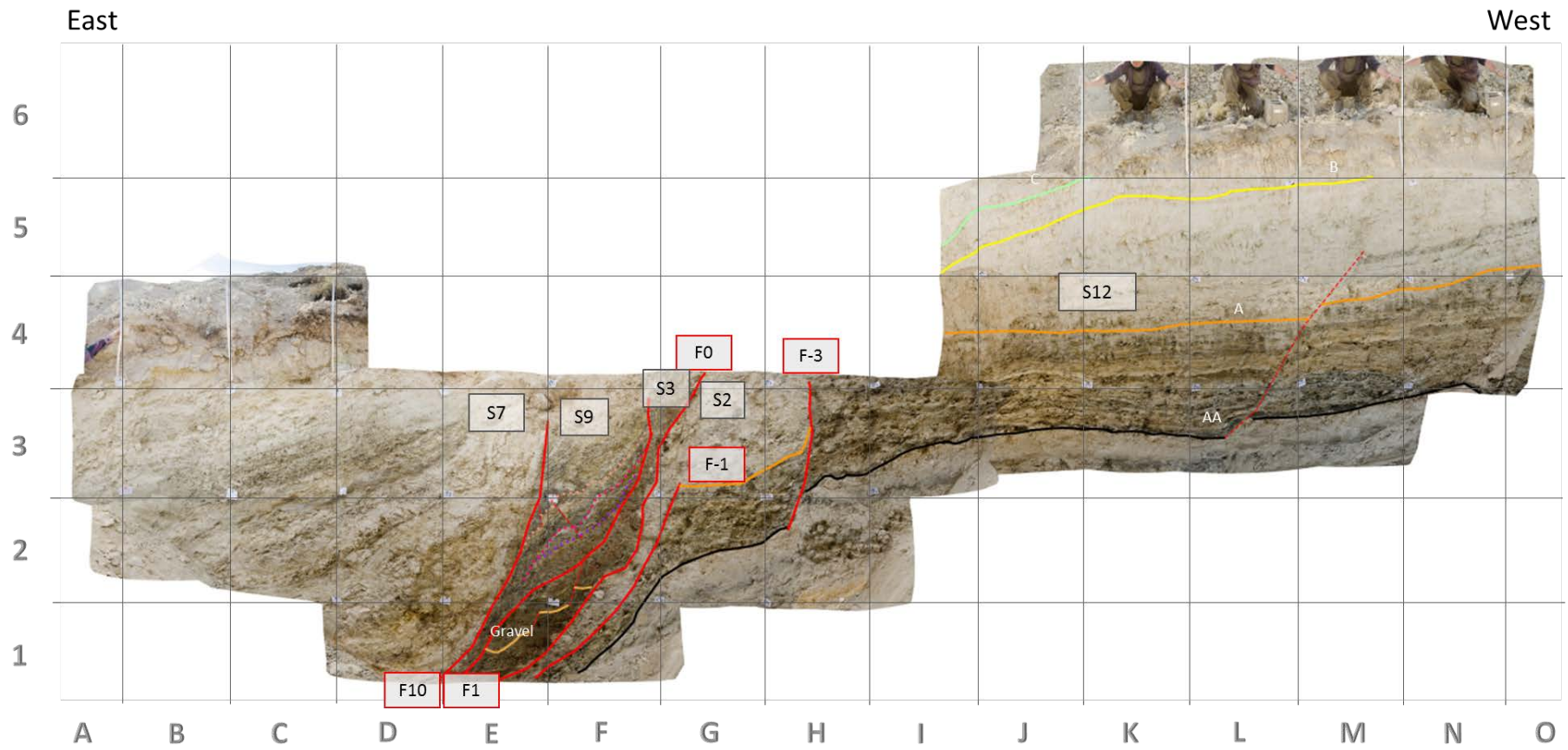
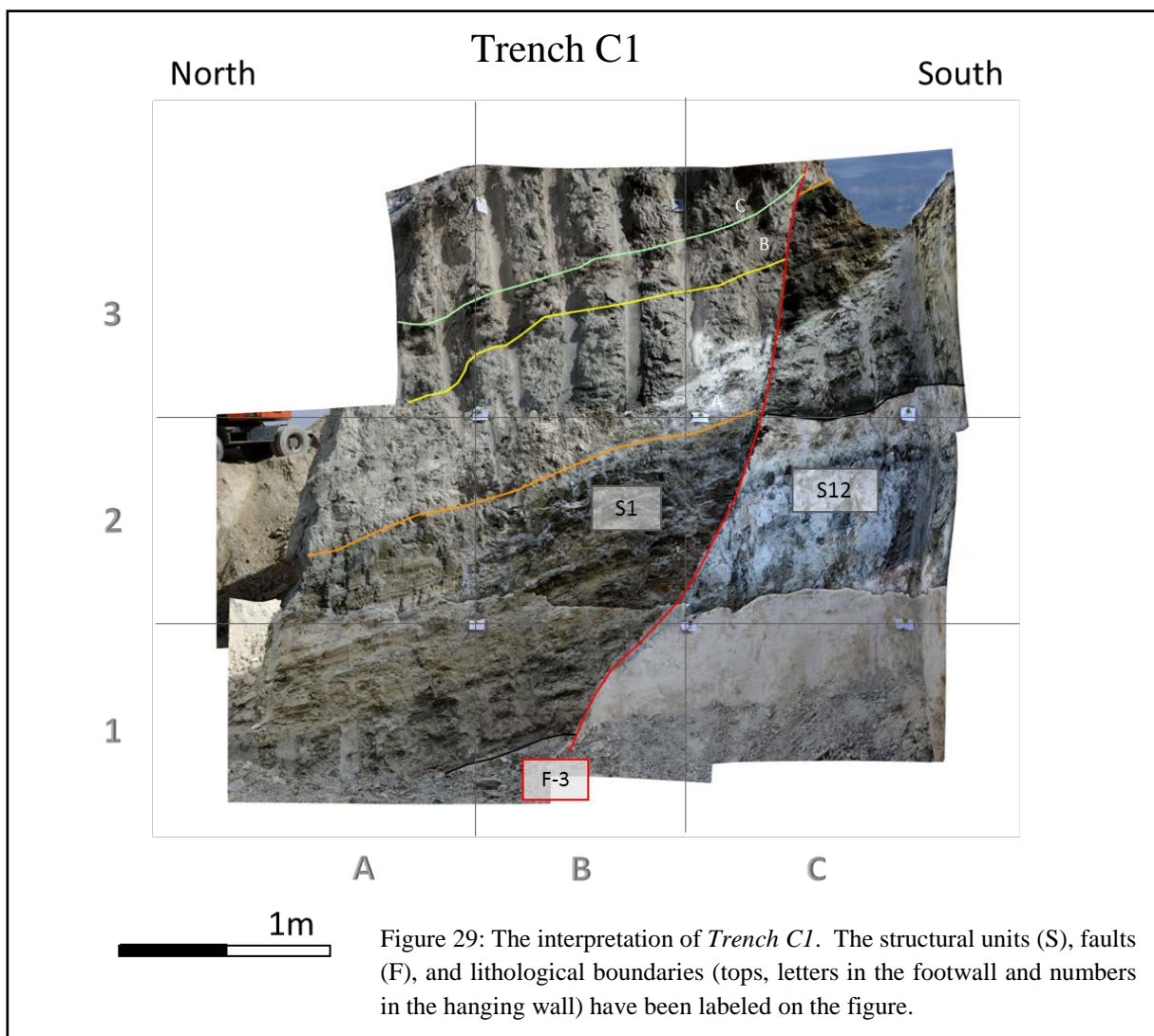


Figure 28: The interpretation of *Trench B3*. The structural units (S), faults (F), and lithological boundaries (tops, letters in the footwall and numbers in the hanging wall) have been labeled on the figure.

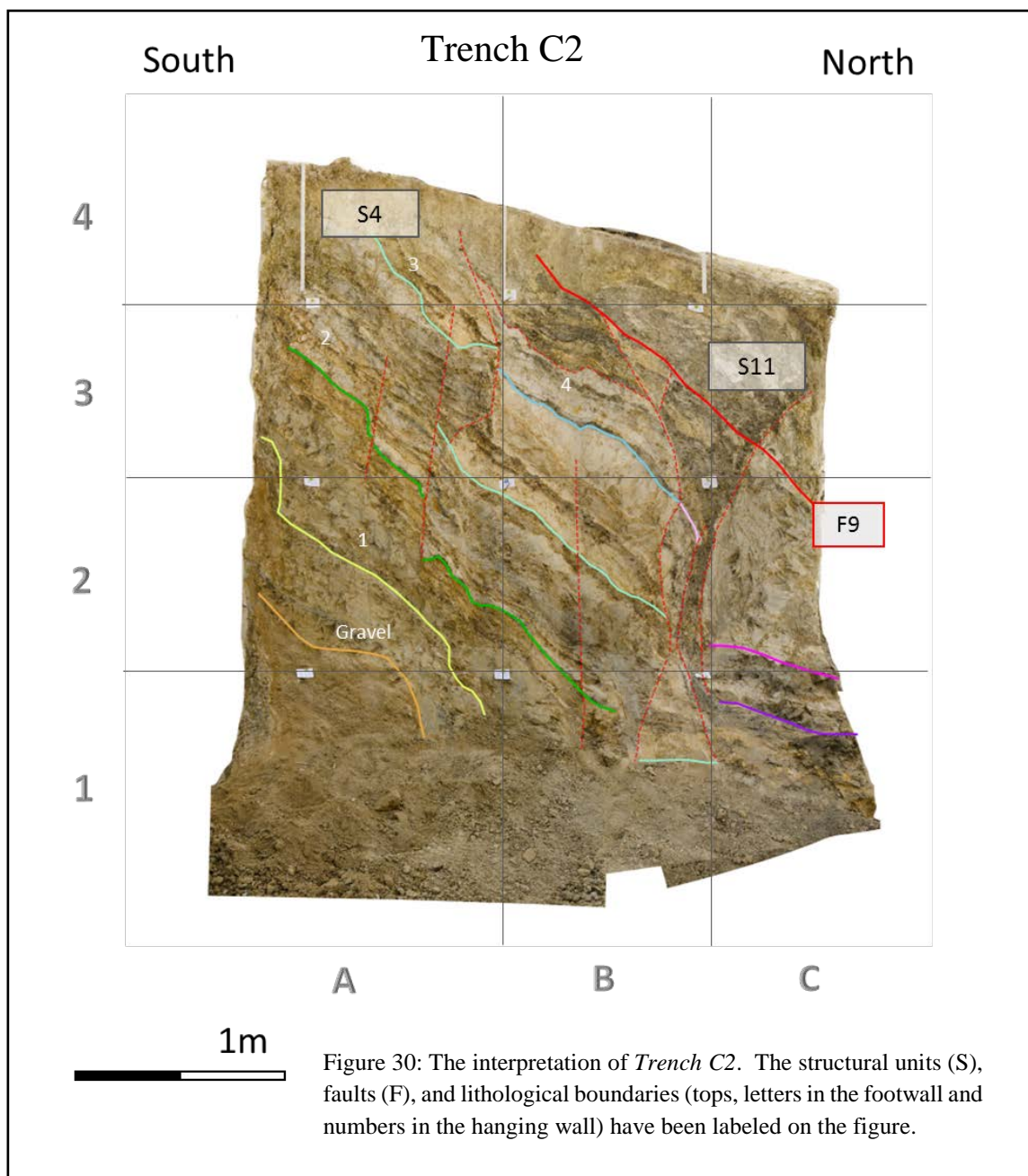
Trench C1

C1 is a nearly orthogonal view of fault -3 in the footwall. Fault -3 is located from cell C3 to cell B1. It dips about 80°N offsetting the horizon AA about 1.3 meters. The beds here have an apparent dip of 18°N.



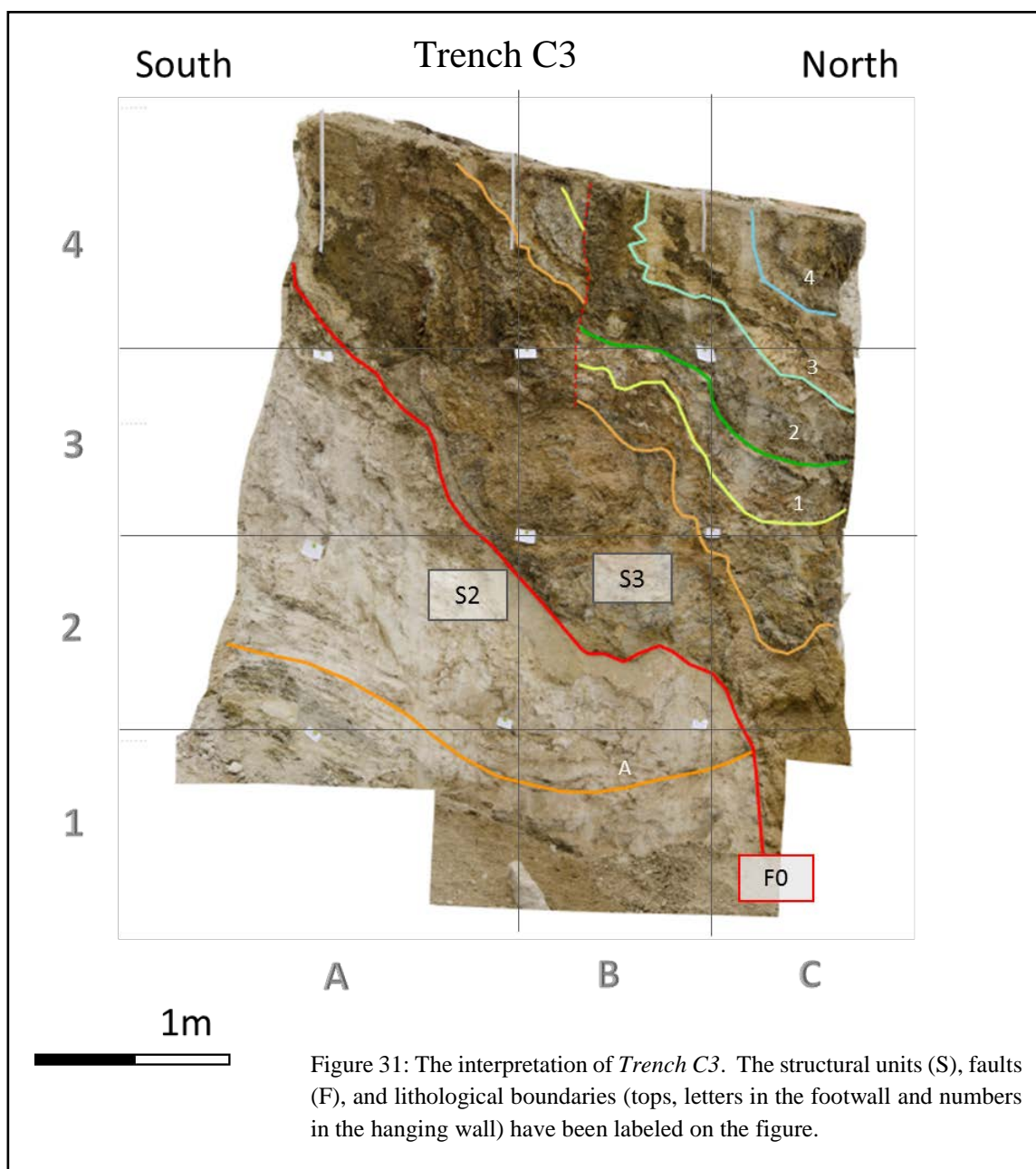
Trench C2

C2 is oriented opposite of C1. Here we have a very good stratigraphy from the gravel in cell A1 through horizon 4 in cell B3. Fault 9 is from cell B4 to C2 separating S11 from S4.



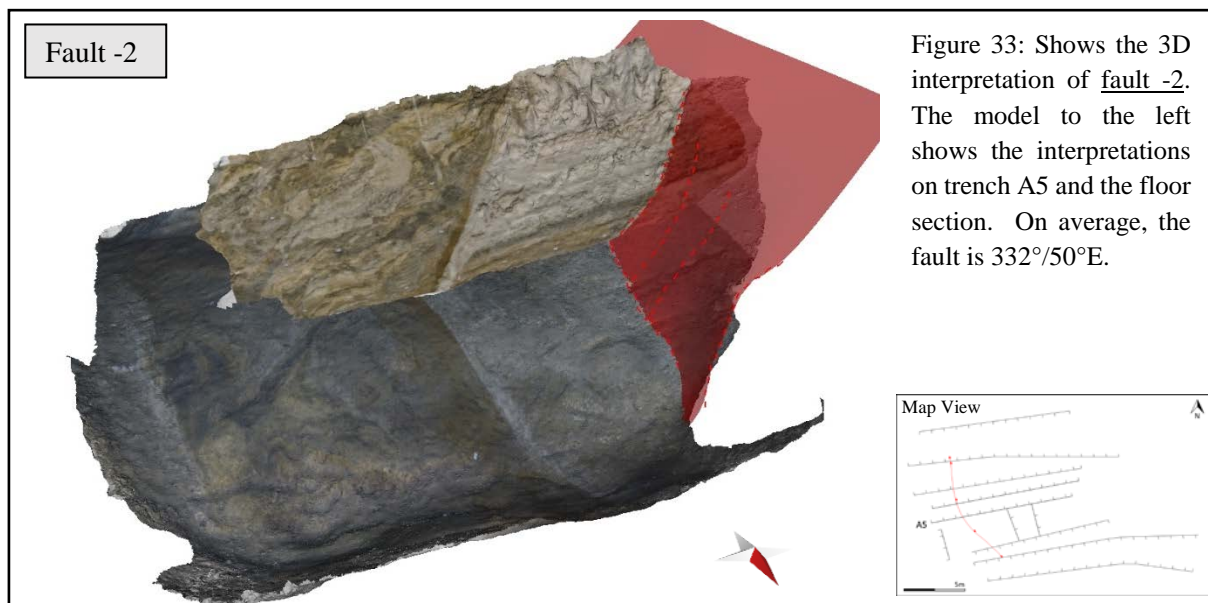
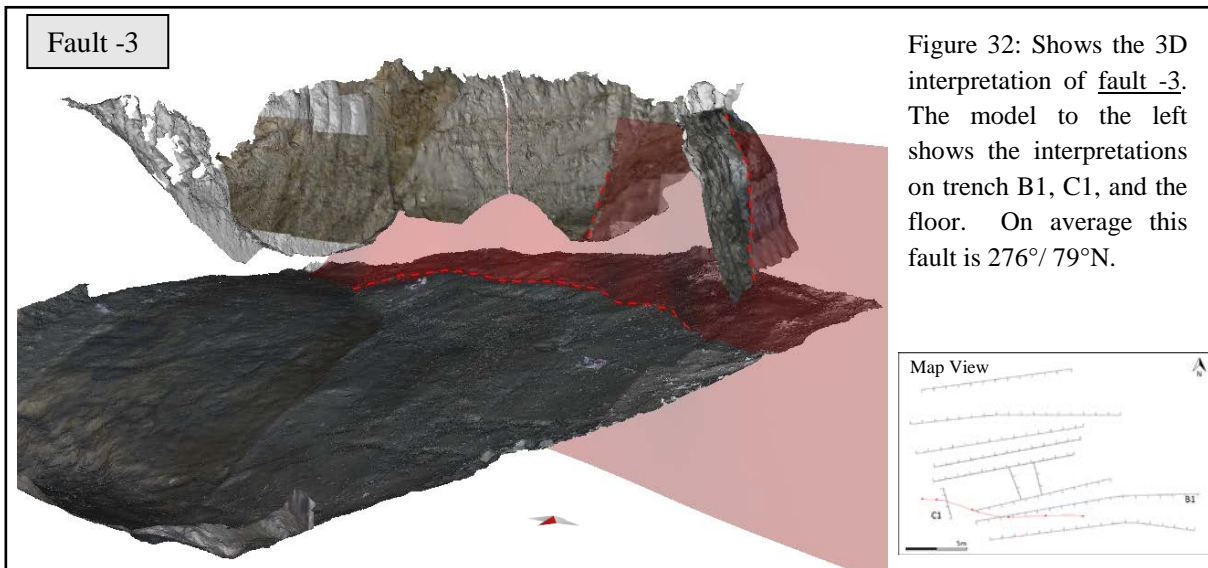
Trench C3

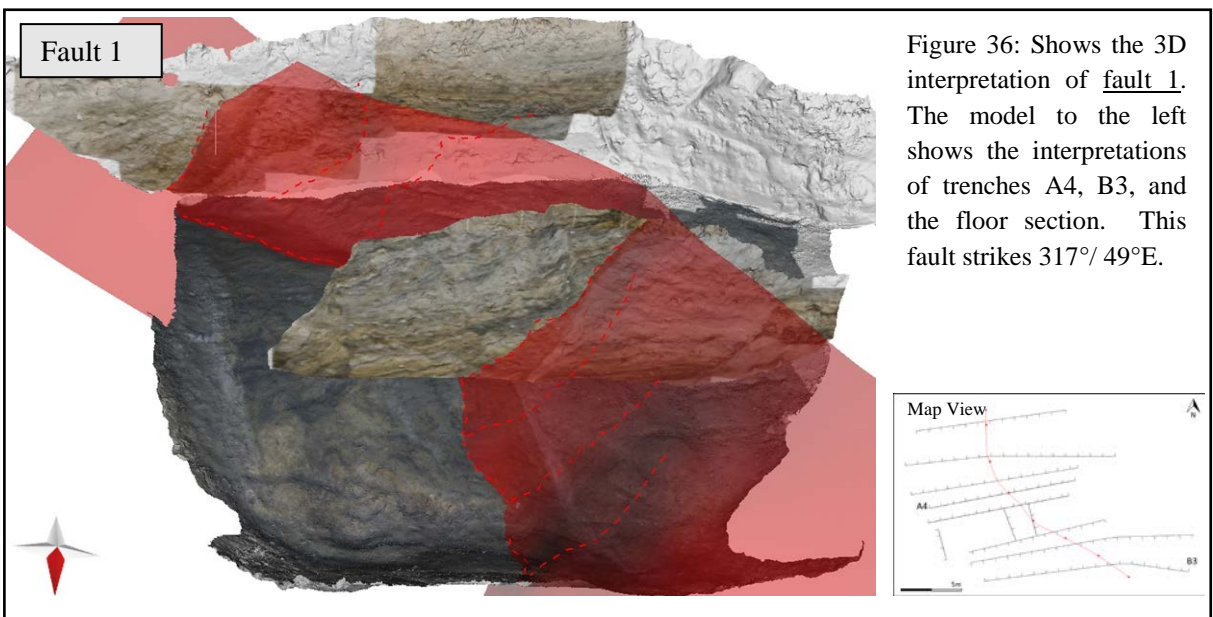
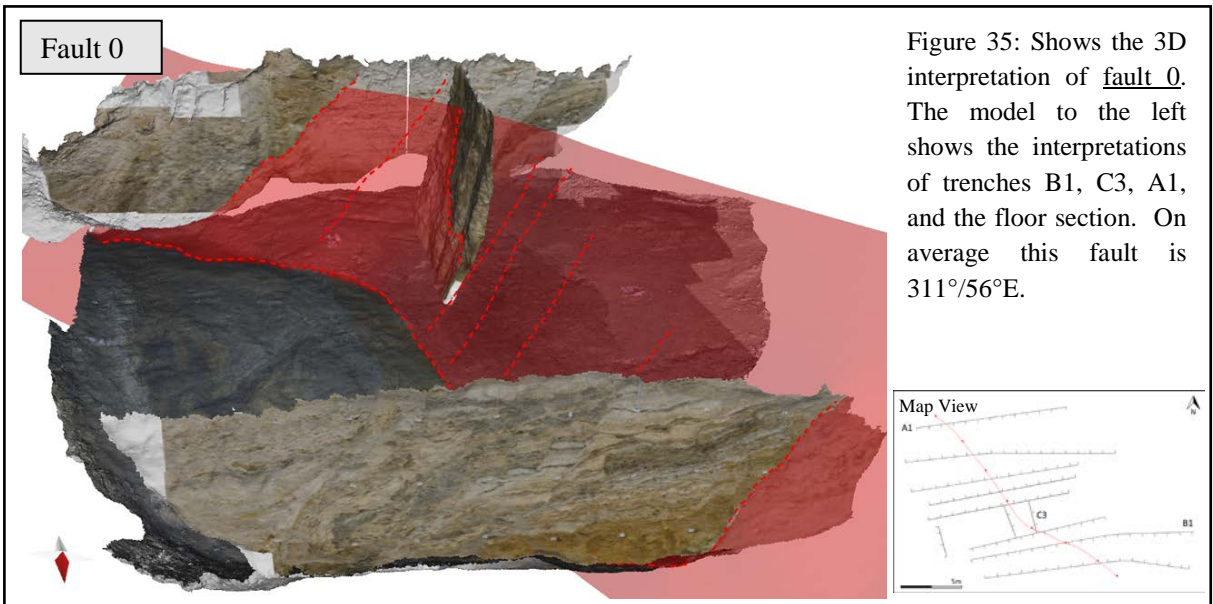
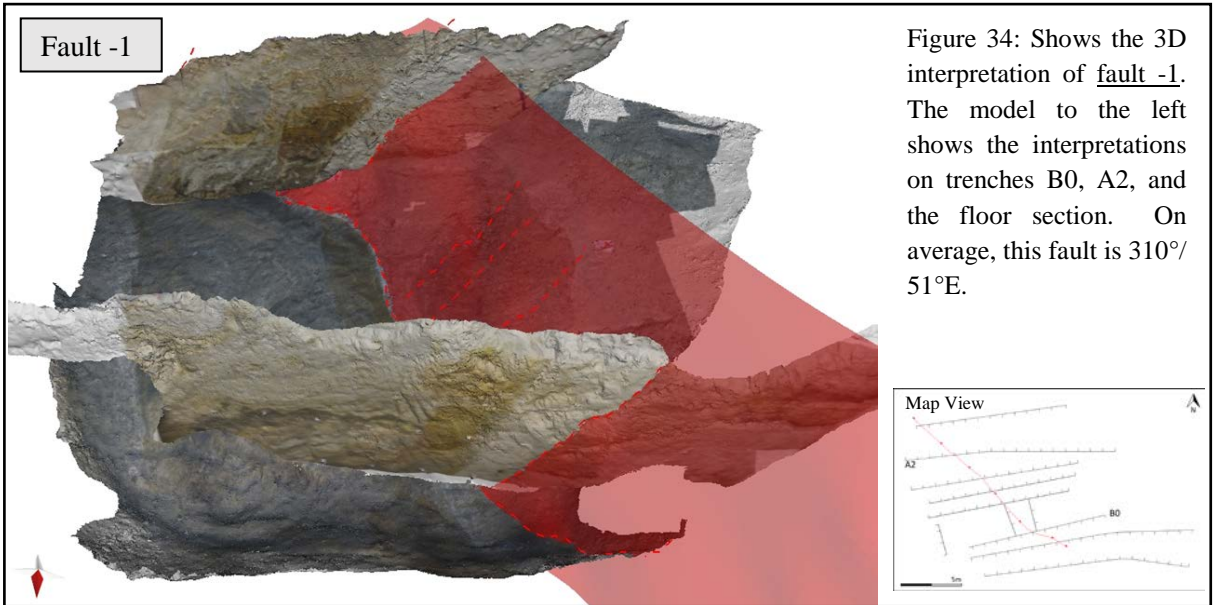
C3 is oriented south to north looking up dip on fault 0, approximately parallel to the strike of fault 0. This is the best view we were able to get of fault 0. S3 is in the hanging wall and S2 is in the footwall. Horizon A is visible in cell B1. The hanging wall contains horizons from the gravel unit to horizon 4 in cell C4.



MODEL

This section describes the resulting 3D model developed from the interpretations of the trenches. Figures 32 through 42 illustrate the different surfaces created from the fault traces identified in the interpretations. Each figure shows the 3D model of key trenches with the fault traces drawn in dotted red lines. It also contains a red transparent surface that passes through the fault traces. In the bottom right of every figure, there is a map view of the reconstructed fault (in red on the map), which shows how each fault is oriented in space and between the trenches. The surfaces representing the lithologic boundaries are displayed in a similar manner. The horizons of the footwall stratigraphy are shown in Figure 43 and the horizons in the hanging wall stratigraphy are shown in Figure 44. Each horizon is displayed separately with the adjacent faults labeled.





Fault 2

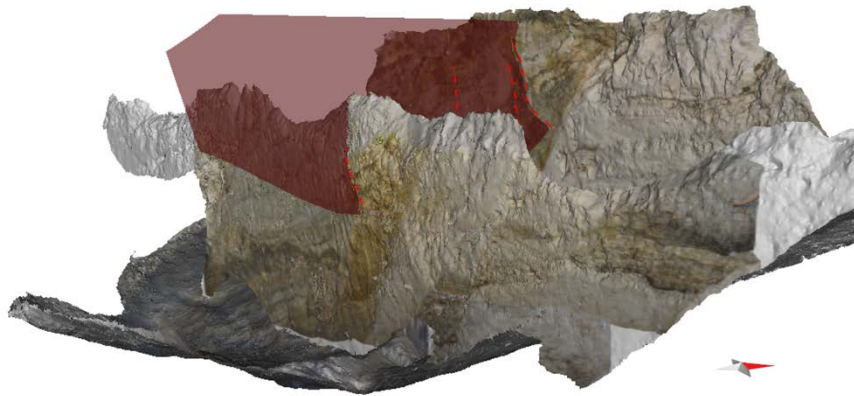
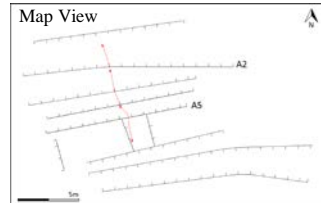


Figure 37: Shows the 3D interpretation of fault 2. The model to the left shows the interpretations of trenches A2, A5, and the floor section. On average, this fault is $163^{\circ}/78^{\circ}\text{SW}$.



Fault 4

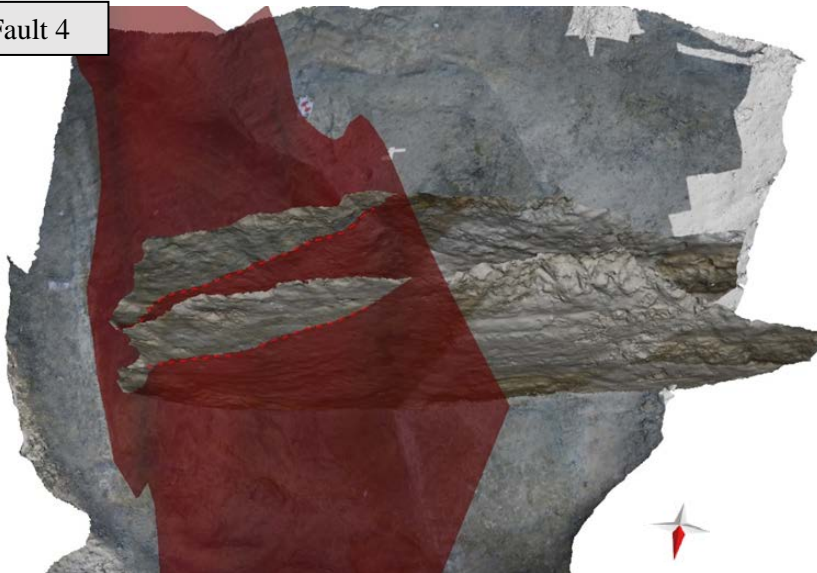
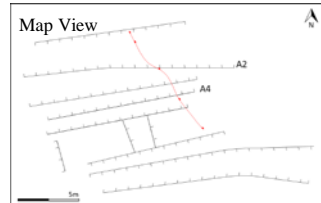


Figure 38: Shows the 3D interpretation of fault 4. The model to the left shows the interpretations of trenches A2, A4, and the floor section. On average, this fault is $321^{\circ}/33^{\circ}\text{NE}$.



Fault 5

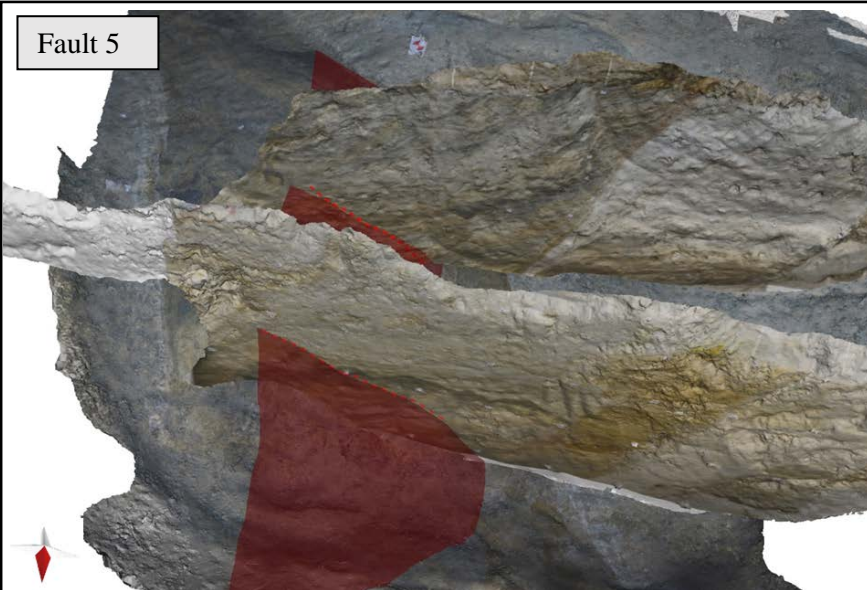
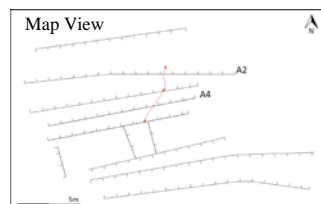
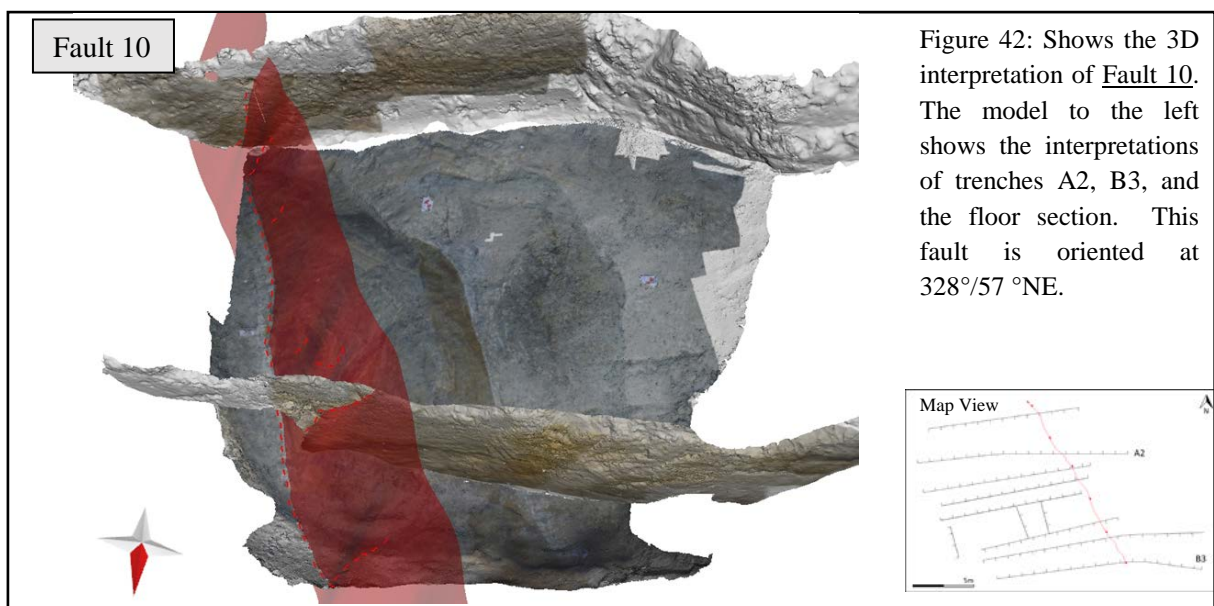
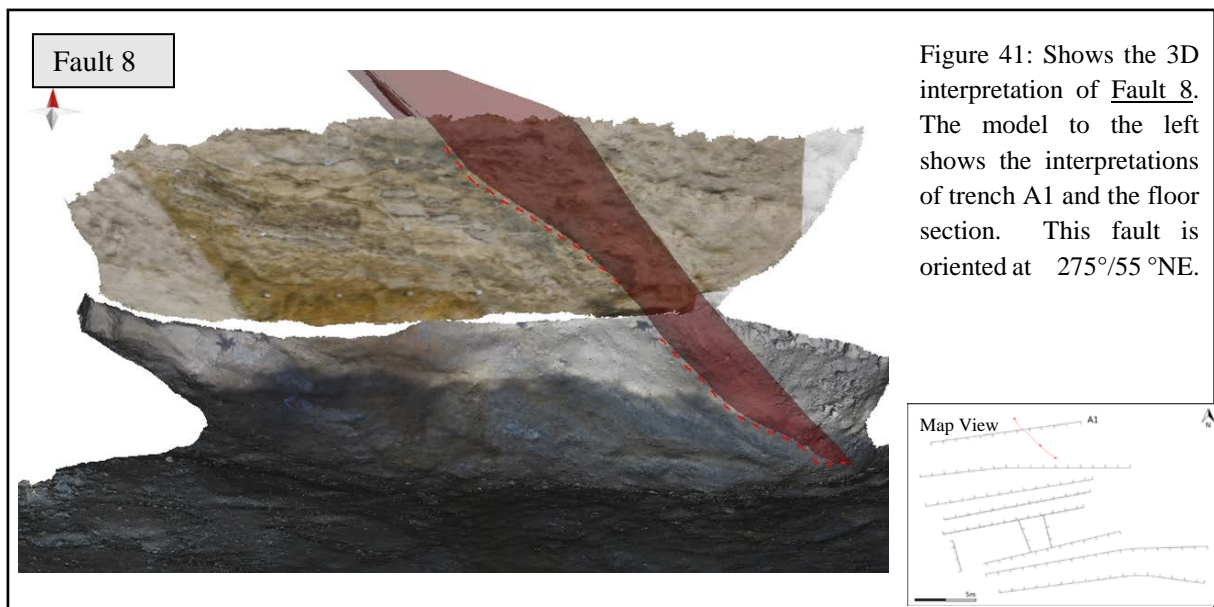
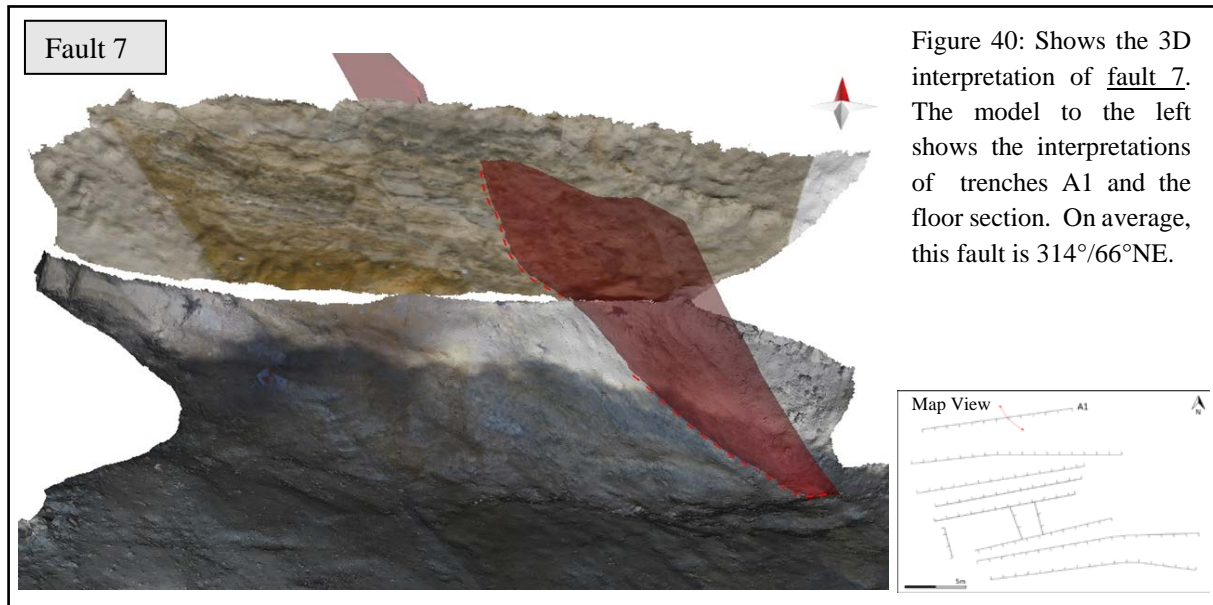
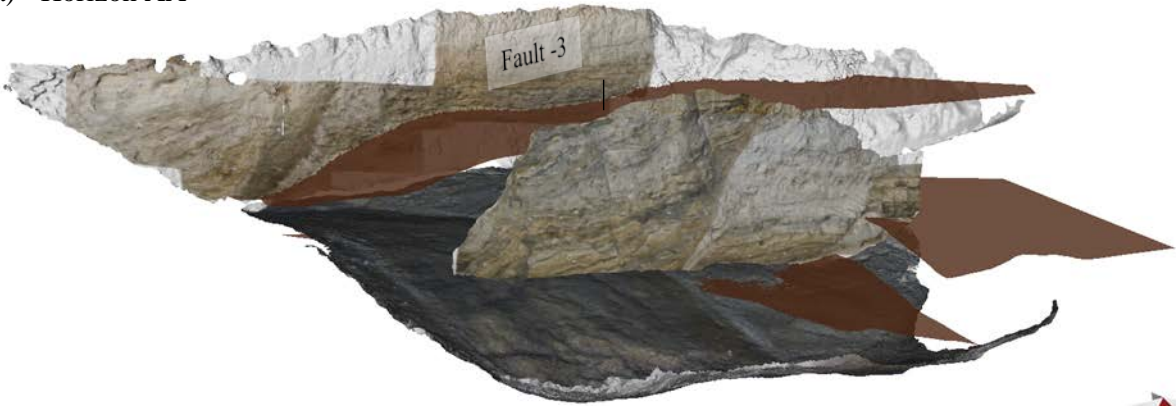


Figure 39: Shows the 3D interpretation of fault 5. The model to the left shows the interpretations of trenches A2, A5, and the floor section. On average, this fault is $287^{\circ}/23^{\circ}\text{NW}$.

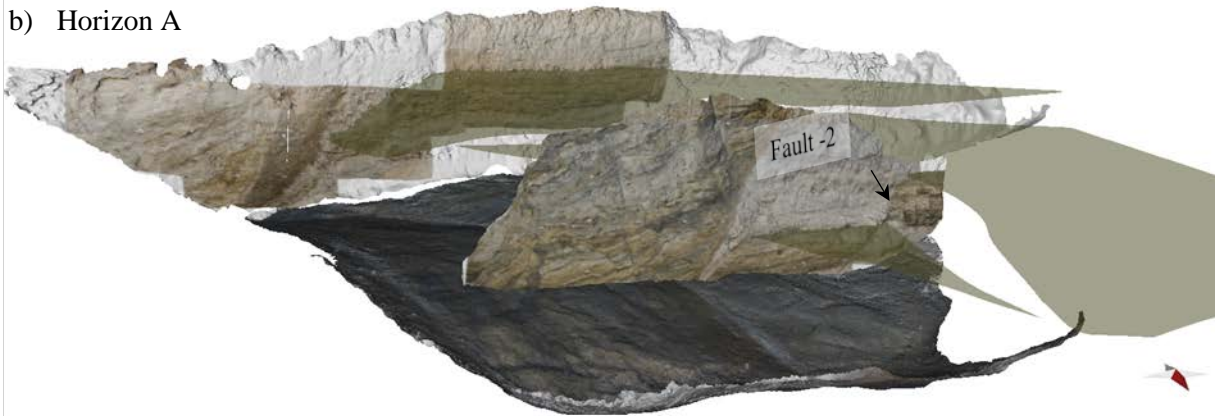




a) Horizon AA



b) Horizon A



c) Horizon C

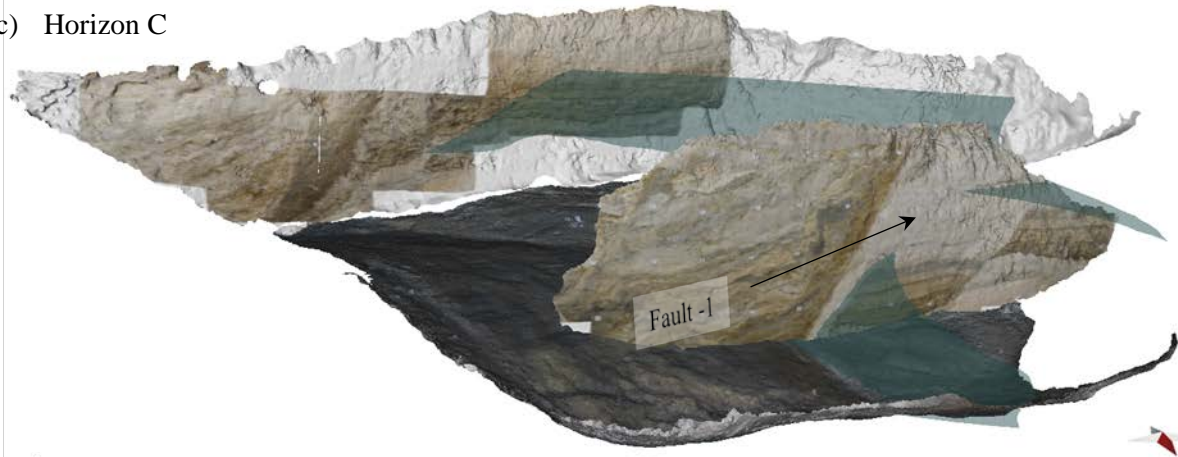


Figure 43: The lithologic boundaries of the footwall stratigraphy. Three horizons were included in the model, (a) Horizon AA, (b) Horizon A, and (c) Horizon C. (a) and (b) have three separate segments. These have been offset by faults -3, and -2. There was no exposure of these horizons in the hanging wall of fault -1. Horizon C (c) only contains 2 separate segments. These have been offset by fault -1. In the footwall, this horizon is horizontal and undisturbed. In the hanging wall, the horizon appears to have been smeared along the fault plane. In the other segments (e.g. footwall of fault -2 and -3), this horizon would be above the model.

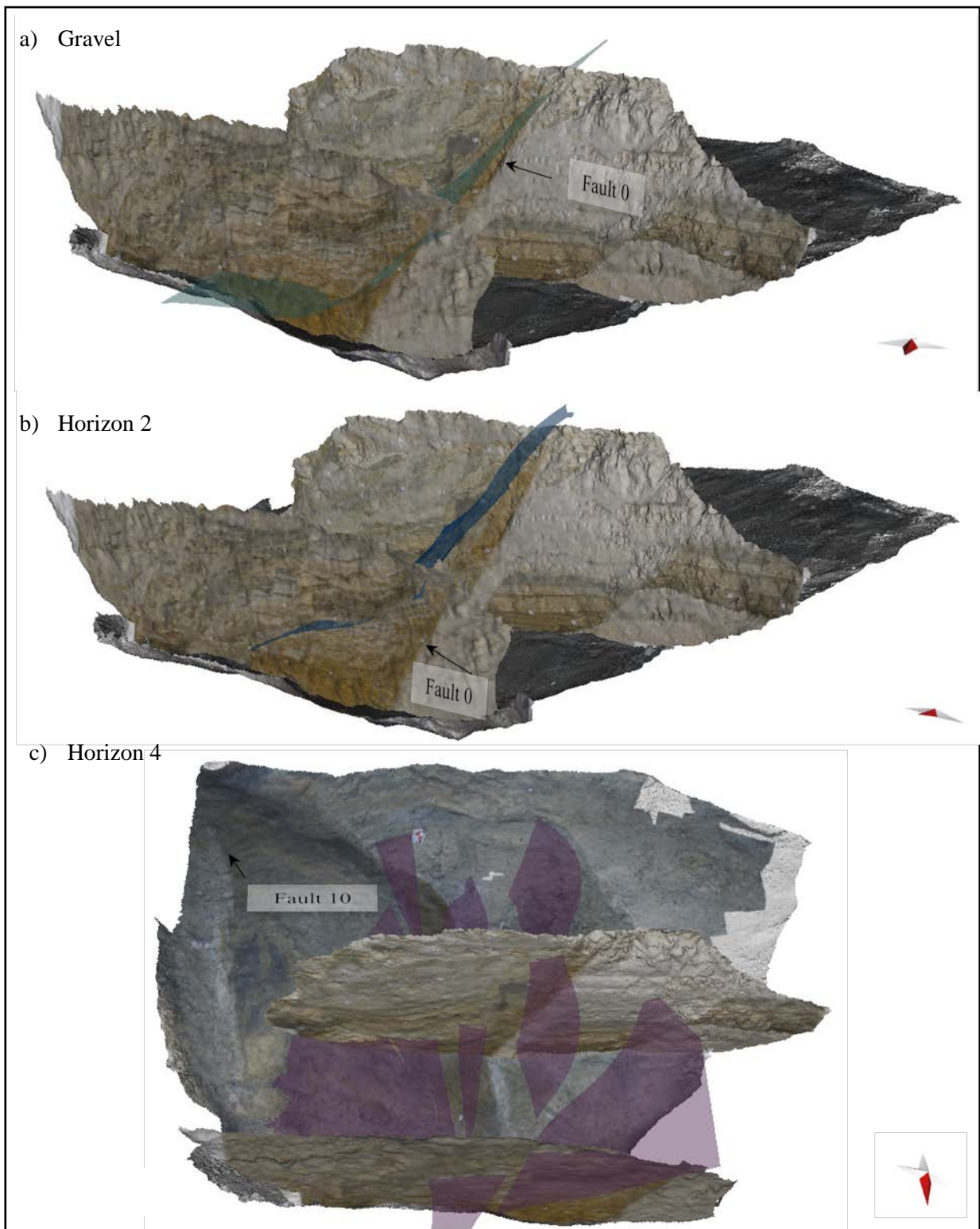


Figure 44: The lithologic boundaries in the hanging wall stratigraphy. Six horizons were included in the model, (a) Gravel , (b) Horizon 2, (c) Horizon 4, (d) Horizon 7, (e) Horizon 8, and (f) Horizon 9. These horizons are contained between fault 0 and fault 10. The gravel unit and Horizon 2 (a and b) had similar geometry. They appear to have been smeared up fault 0 in the direction of fault movement. Horizon 4 (c) however looks much different from the other two. This unit has exposures in almost every hanging wall structural unit so it has many different segments. The unit is generally dipping about 30 degrees to the east and offset by the series of faults in the hanging wall. *Continued on the next page.*

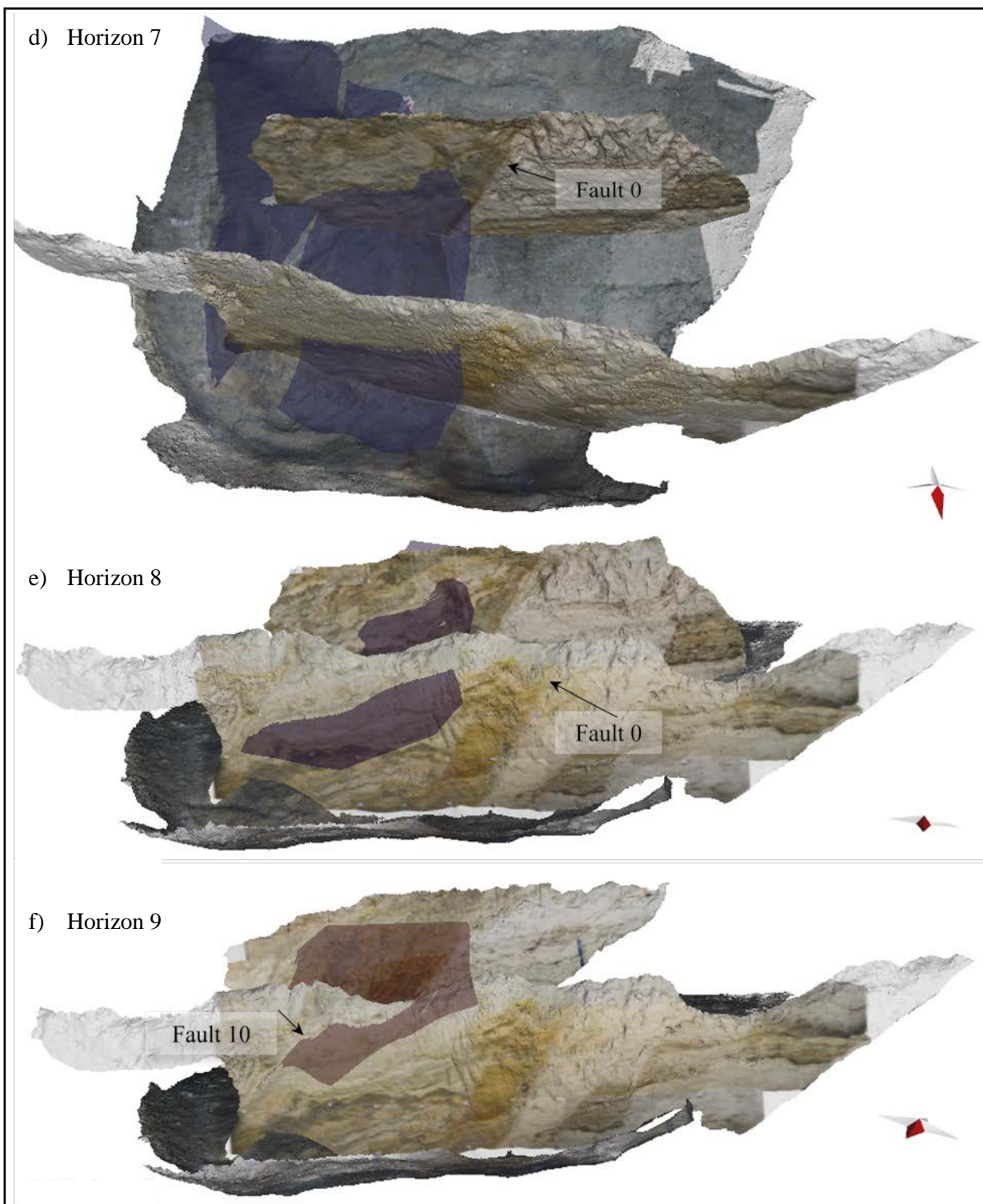
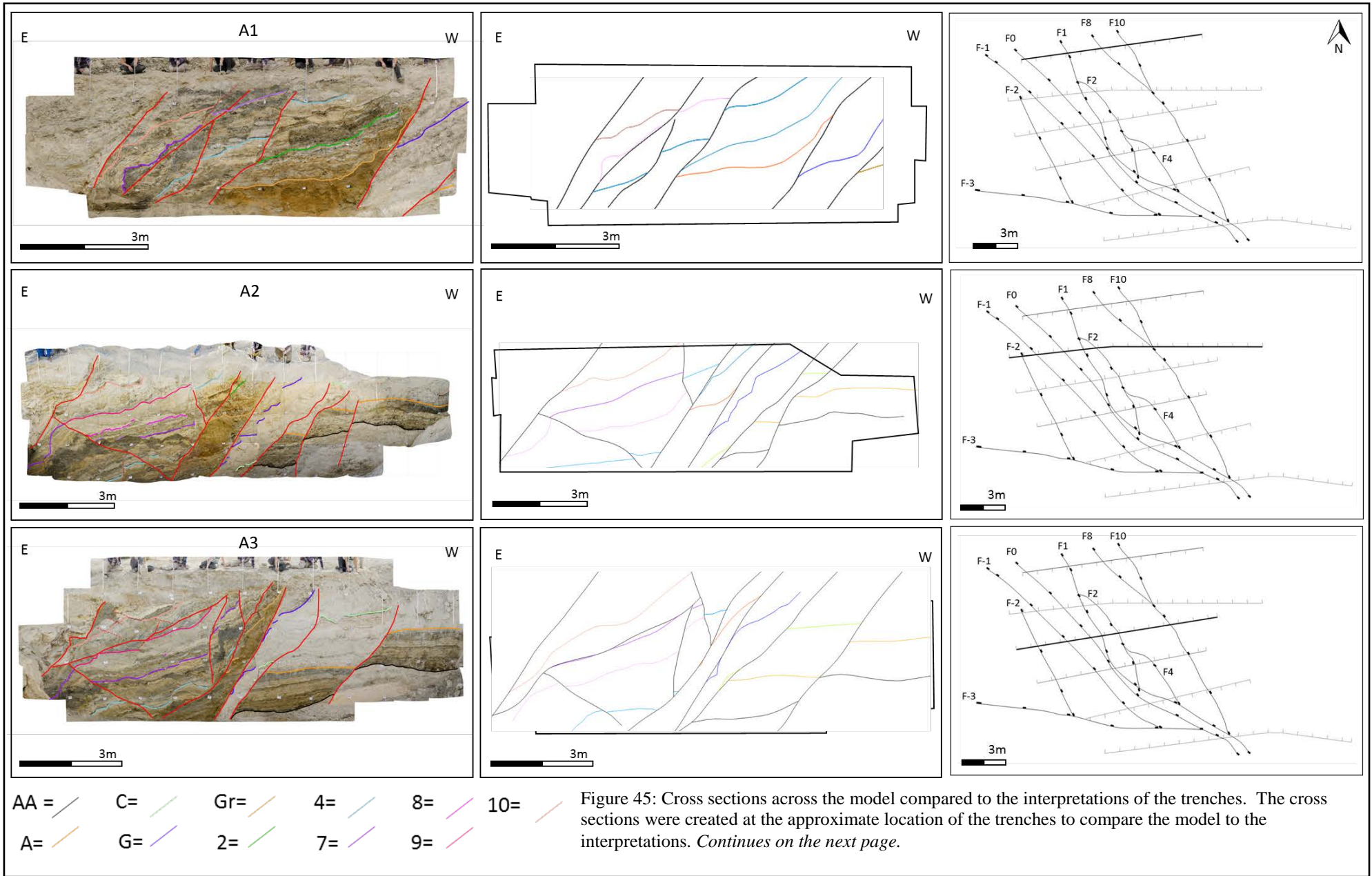
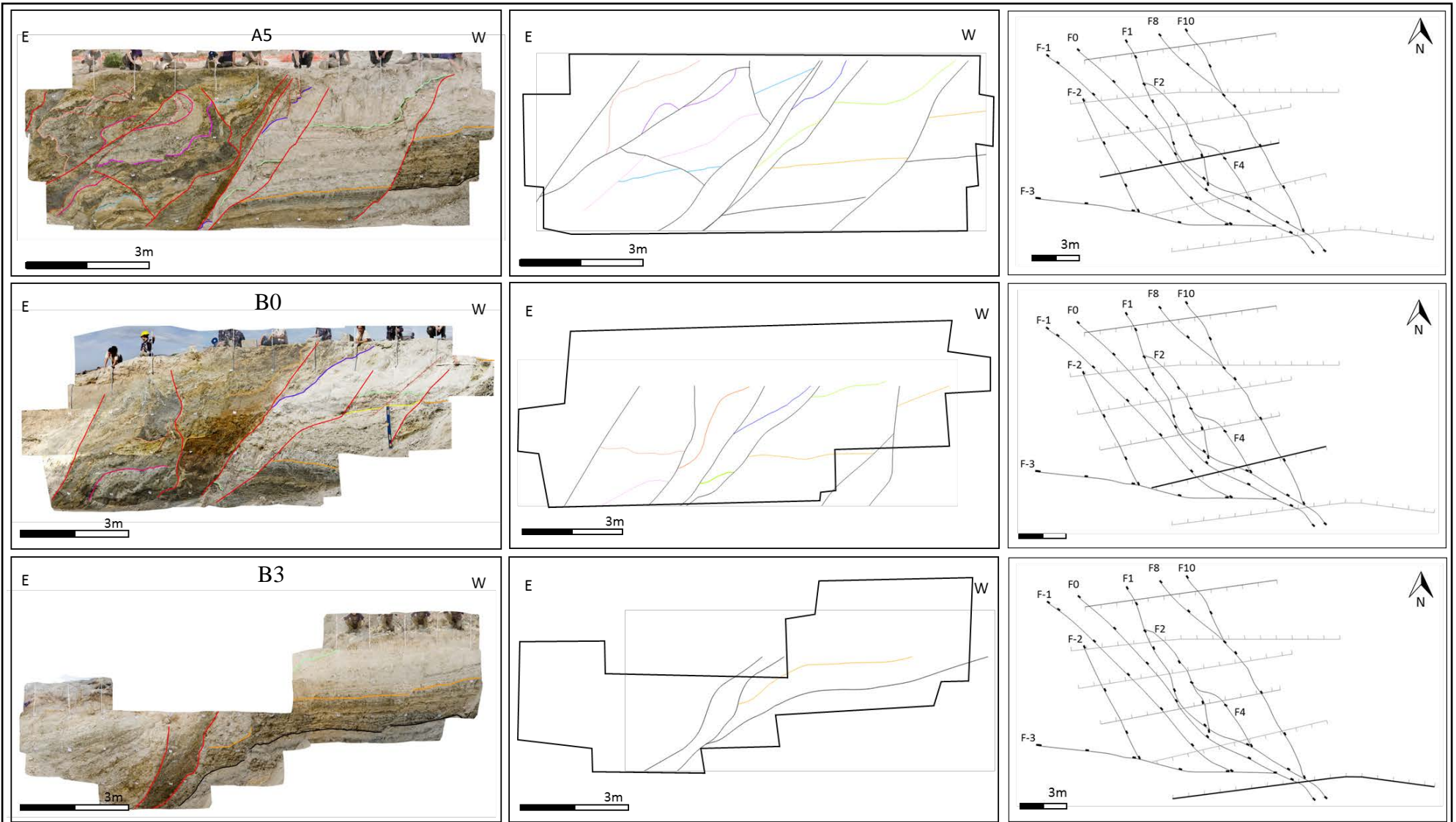


Figure 44 *Continued*: Horizon 7(d) is a highly deformed unit that forms some of the injection structures seen in the southern portion of the study area. This formation dips gently to the east between faults 0 10. Horizons 8 and 9 (e and f) are also highly deformed units that lie both above and below fault 4. These horizons only exist in one of the structural units to the south of the study area.

All of these surfaces constitute the model. The faults define the structural units and the horizons are interpreted inside of these structural units. In an attempt to better display the consistence and validity of the model, Figure 46 shows cross sections through the model at the approximate location of the trenches. In the figure, the interpreted trench is shown first. Next to the trench image is a cross section taken from the model. The lines displayed here are not the interpretations, but intersections of the surfaces with the section. Similarities between the interpreted faults and horizons on the trench and the model's intersections of the cross section show that the 3D model fits the interpretation well. The map on the far right shows the location of cross section highlighted in black. Generally, the model is consistent with the interpretations. The lines tend to be smoother in the model. This results from the process of creating the surfaces using Kriging.





AA = / C= / Gr= / 4= / 8= / 10= / *Figure 45 Continued*
 A= / G= / 2= / 7= / 9= /

DISCUSSION

This case study presents a comprehensive data set and interpretation of an active normal fault zone at the sub-seismic scale. The fault zone was excavated in a trenching campaign in southern Spain. The field data was processed and compiled into a virtual outcrop that was visualized in LIME. Using this platform, the trenches were interpreted in 3D and used to create surfaces representing the faults and horizons. This resulting model is a compilation of all the data and interpretations. It can be used for visualizing and studying the internal structure of a ~30 m throw strand of the Baza fault. It can also be used for further experimentation studying the effects of a fault zone on subsurface imaging, permeability structure and fault seal analysis.

The model is best illustrated in Figures 46 and 47. Figure 46 is a series of horizontal sections through the model. There is one meter between each. Figure 46b is closest to ground level, and the subsequence maps are progressively deeper. This demonstrates the vertical variability in this fault zone. Between each section, there are dramatic structural changes, most notably in the hanging wall where the assemblage of structural units (S) changes from meter to meter. Lines drawn across each horizontal section in Figure 46 indicate where corresponding cross sections are located in Figure 47.

Figure 47 shows vertical cross sections through the model perpendicular to the average strike of the structures. Each cross section is approximately 3 meters apart starting with Figure 47a, which is farthest north. These cross sections demonstrate the lateral changes in the structural units (S) along the strike of the fault. The lines drawn across each cross section in Figure 47 indicate where the horizontal sections intersect.

According to the definition of fault zone elements from Caine et al. (1996), the fault core would be defined as a very narrow band within fault 0. Here is where the majority of fault displacement is accommodated and the volume is occupied by incohesive material with no visible rock fragments or distinguishable structure. According to the modified Sibson's classification scheme, this rock material would be fault gouge (Scholz et al., 1991).

This strand is likely interacting with many other strands with complicated relationships on a larger scale. It is difficult to identify an isolated damage zone in this context. This difficulty is enhanced by the limitations of this study and window of exposure through this trench.

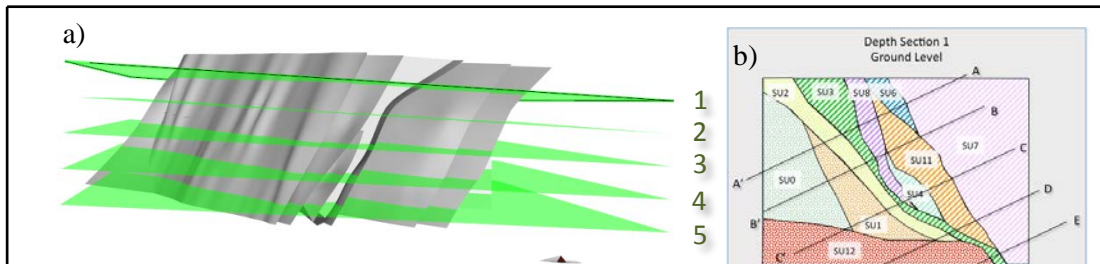


Figure 46: Horizontal sections through the fault model illustrating the vertical variations of the structural units. (a) Shows the location of sections 1 (b), 2 (c), 3 (d), 4 (e), and 5 (f). Sections are 1 m apart.

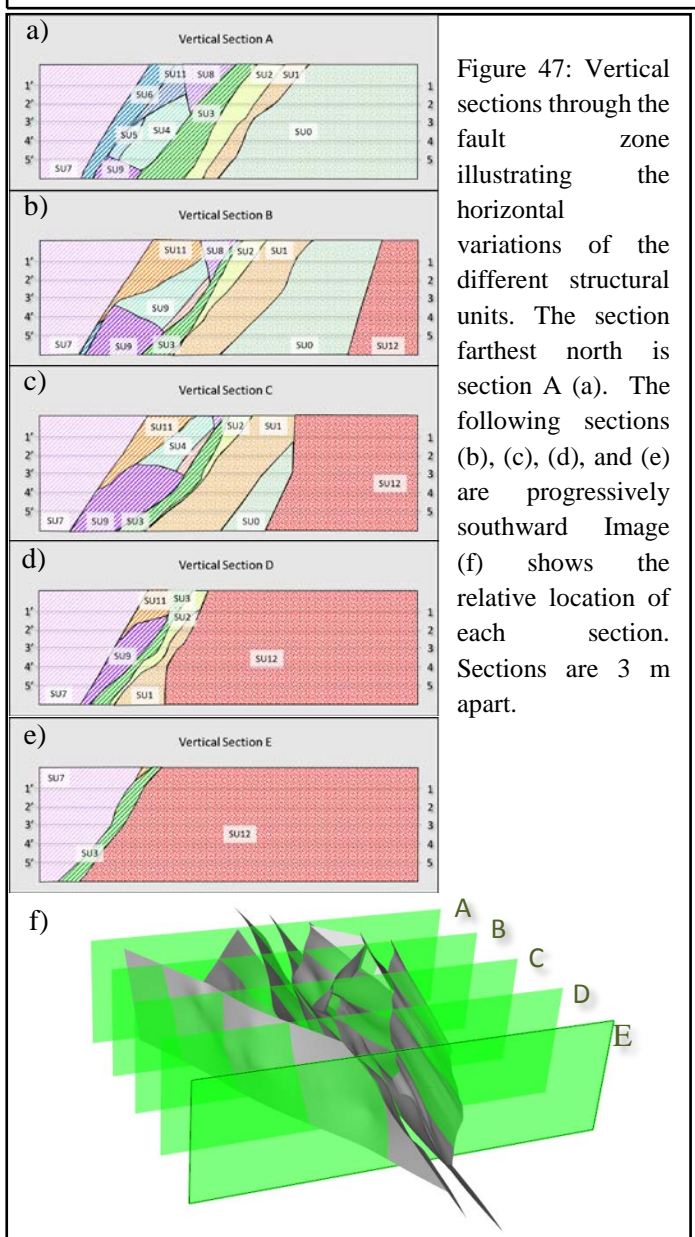
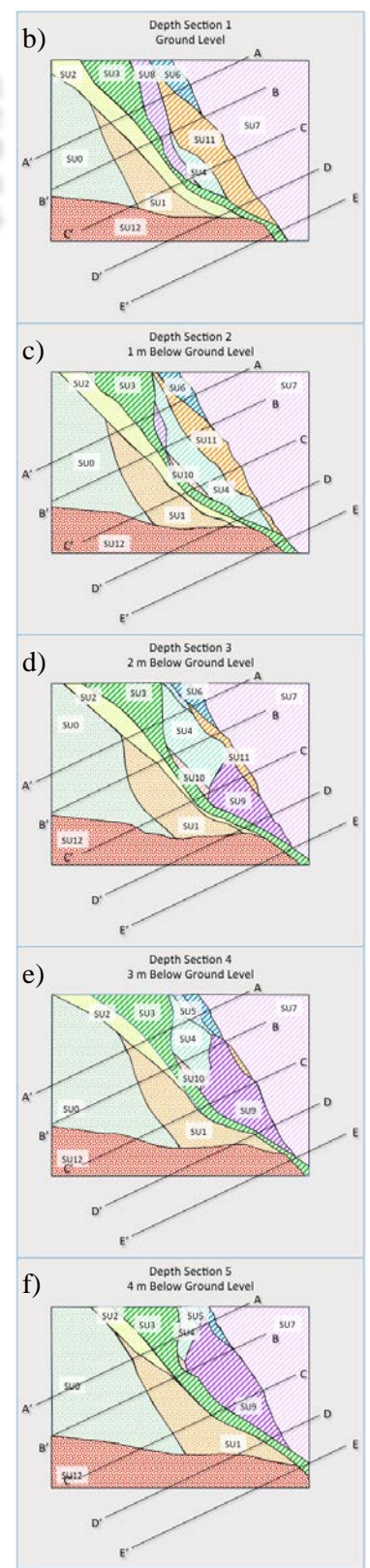


Figure 47: Vertical sections through the fault zone illustrating the horizontal variations of the different structural units. The section farthest north is section A (a). The following sections (b), (c), (d), and (e) are progressively southward. Image (f) shows the relative location of each section. Sections are 3 m apart.



However, for the purpose of this report, the fault zone will be defined as between the two outer most faults, fault -3 in the footwall and fault 10 in the hanging wall. There are likely more structures outside of the study area, but these were not observed thus not considered in this model.

The footwall and hanging wall of the fault zone had very contrasting characteristics. The footwall was not deformed to the same degree as the hanging wall. However, there are significant kinematically related fault segments offsetting the main structural units. The structural units of the footwall wall include S0, S1, S2, and S12. These are indicated by the stipple pattern in Figures 46 and 47. Three major faults separate these units with occasional minor faults, but, the volume of rock bounded by these faults are largely undisturbed.

The characteristics of the hanging wall damage zone are significantly different. These structural units are indicated by the diagonal stripe pattern in Figures 46 and 47. The cataclasis, rotation, and shearing of the rock volumes create a highly brecciated configuration. However, it is difficult to identify these units as a fault breccia as there is no determination of clast size separating a fault breccia and fault bounded rock volume (Childs et al., 2009).

The first structural unit on the hanging wall is S3, which starts as a broad unit. It then thins and nearly disappears when moving from north to south. The structural character of this unit changes from a broad, brittle deformed unit with very distinct lithological boundaries to a narrow unit that has been deformed so entirely that the lithological boundaries become indistinguishable.

There are two small structural units between S3 and the rest of the hanging wall units. These are S10 and S8. There is no significant internal structural deformation on the volume of these units and minimal offset between the two. There is even less offset between S10 and the adjacent unit S4 (Figure 24). Possibly, these units began as one, which through further deformation it was offset by faults resulting in two young structural units. S10 and S8 disappear to the south (figure 47c and 47d) as the splay closes.

S4, S9 and S11 are the largest units in the hanging wall, and have similar trends as S3. These structural units have vertical variations related to the low angle faults dividing them. The internal deformation changes from very brittle deformation to ductile moving southward. In

the south, there are also fluid injection structures that become more prominent as the bounding faults approach each other. There is an emerging trend of the deformation style shifting from brittle to ductile with decreasing structural unit width.

There are two structural units, S5 and S6, that only appear in the northern most trench and the floor section (Figure 40 and 41). These units have undergone significant plastic deformation relative to the adjacent S3. S7 is the farthest unit to the east and the most distal structural unit from the fault core. Here, detachment folds related to fault 10 were identified on the hanging wall. There was very limited observation into these beds so it is impossible to know whether or not there are more fault related structures farther away, similar to what was seen in the footwall.

The faults trend NE-SW and dip between 50 and 60 degrees eastward. The low angle faults interpreted in the hanging wall are cross cut by the high angle faults, which establishes a relative age relationship. This suggests that the low angle faults are older features offset by the younger high angle faults. There were no low angle faults on the footwall, but they could possibly be higher in the footwall section and eroded away.

The two most prominent faults in this fault zone are 0 and 1. These are relatively smooth surfaces which indicate relative maturity. These are likely the faults that bound the fault rocks in S3. The neighboring faults are then a result of successive fault propagation. As this strand of the Baza Fault propagated, inherited geometrical features from breaching segments formed the adjoining structural units. In the footwall the strain is concentrated in fewer slip surfaces, resulting in larger more rigid and intact rock volumes. In the hanging wall, the strain has been distributed throughout the formation of many faults with small displacement resulting in brecciated character. This is likely a result of both preexisting structures and the rheological differences of the hanging wall and footwall stratigraphy. The processes of growing the fault in both length and width previously discussed (figure 5) results in a highly variable fault zone not only along the strike, as observed in this study, but also along dip.

When the fault zone displacement is plotted versus thickness on a linear scale, the variations are so broad that there appears to be no statistical relationship between the offset and thickness (Evans, 1990). However, when shown on a log-log scale (Figure 48), a weak relationship

emerges. The thickness of the fault zone and fault rock from this study overlain on compiled data from Childs et al. (2009), show this faults in the higher end of studies conducted.

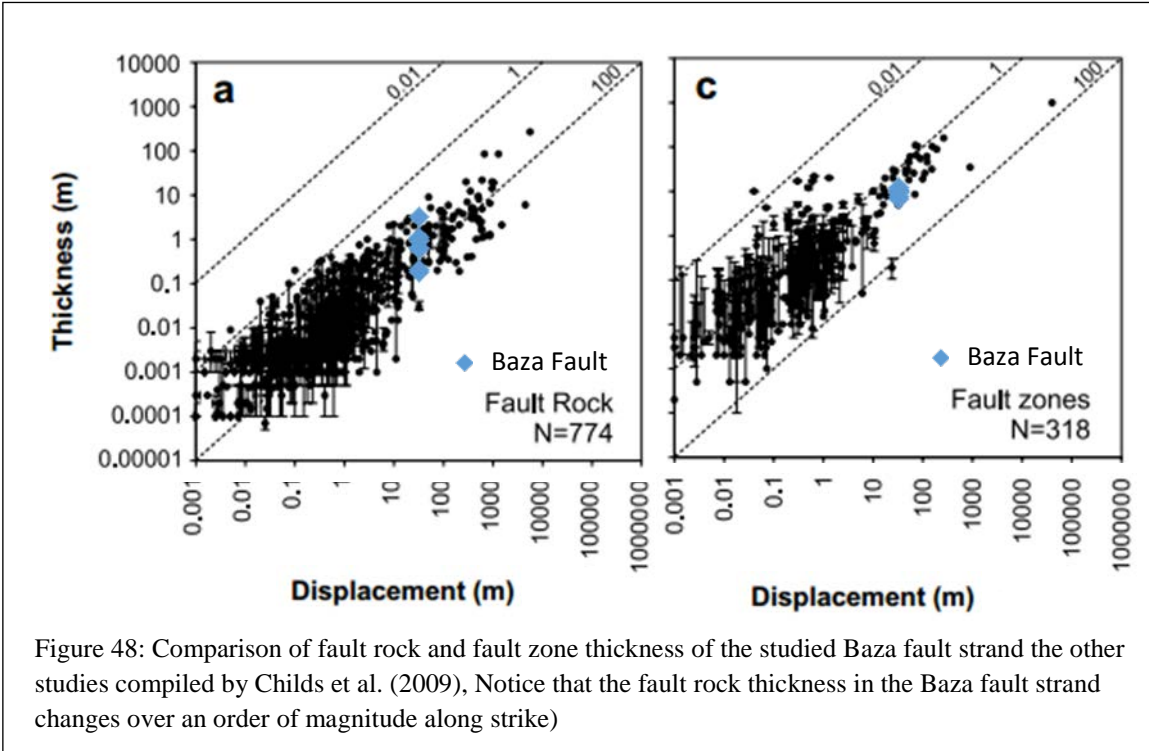
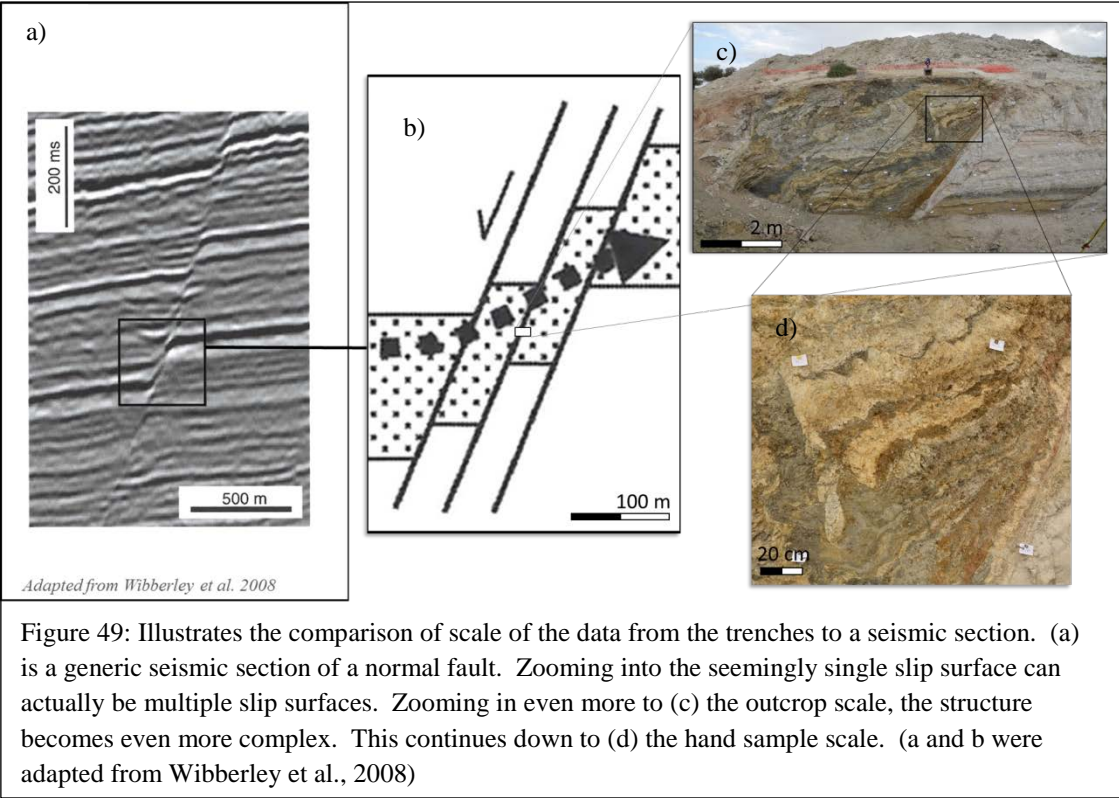


Figure 48: Comparison of fault rock and fault zone thickness of the studied Baza fault strand the other studies compiled by Childs et al. (2009), Notice that the fault rock thickness in the Baza fault strand changes over an order of magnitude along strike)

Fault zone thickness is an important aspect of fault zone geometry for reservoir flow models. The current models used today to determine this parameter are weak at best (Manzocchi et al., 2010). As shown in this study and many studies before, the thickness can vary drastically over short distances. By studying the geometrical structure of fault zones through outcrops, and larger scale mapping, more data can be available to establish a relationship and improve the prediction of fault zone thickness. This would thus improve the accuracy of flow models. Resolving this issue is of course, outside the scope of this project. However, the data presented here can be compared to other case studies and provide more data and used to unlock this relationship.

The size of this fault is below the resolution of most seismic data (Figure 49). What is seen in an outcrop scale is roughly the thickness of the line that would be interpreted on a seismic dataset. Because of this scale issue, modeling the properties of the volume of a fault zone cannot be done deterministically. However, the methods used to represent the faults in reservoir models can be improved through the observations from outcrop studies. Also, by modeling the response of fault zones, or acquiring high-resolution seismic or GPR data, we can begin to relate

the seismic character to the zone character. Figure 50 shows an example from one data from this trench (the modelling was performed by Isabelle Lecomte at UiB). Here, elastic properties have been assigned to the different lithologies and the seismic response was modeled showing both perfect illumination and perhaps a more realistic limited illumination.



There are many other future studies that can be done to improve upon this research. This is only one trench on one strand of a much larger structure, the Baza Fault. To get more information and understanding of this particular system, there needs to be more trenching along this strand, and more trenching along other strands. It is possible to model the seismic response to this trench as shown in figure 50. However, it would be really interesting to acquire seismic data over another trench, create a model of that trench and see how the modeled seismic matches the acquired. The Baza fault is an excellent location to study how the geometry of a fault zone varies, how the internal structure of the volume of rock changes and how these changes impact a reservoir system.

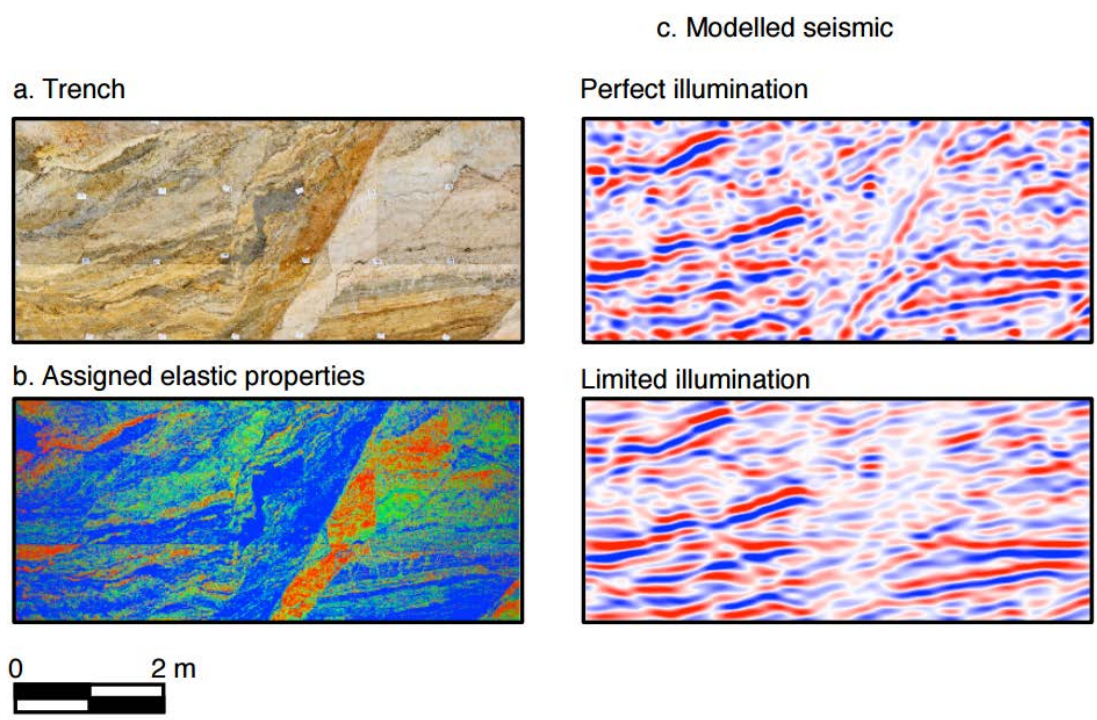


Figure 50: Seismic Modeling of trench A3 by Isabelle Lecomte at UiB. The input to the model is the trench lithology (a) which has been assigned elastic properties (b). (c) Is the modeled seismic response using a ray-based pre-stack depth migration simulator (Lecomte et al., 2015, 2016) with perfect and limited illumination. The modeled image is equivalent to high frequency seismic and ground radar (courtesy of Isabelle Lecomte, unpublished).

CONCLUSION

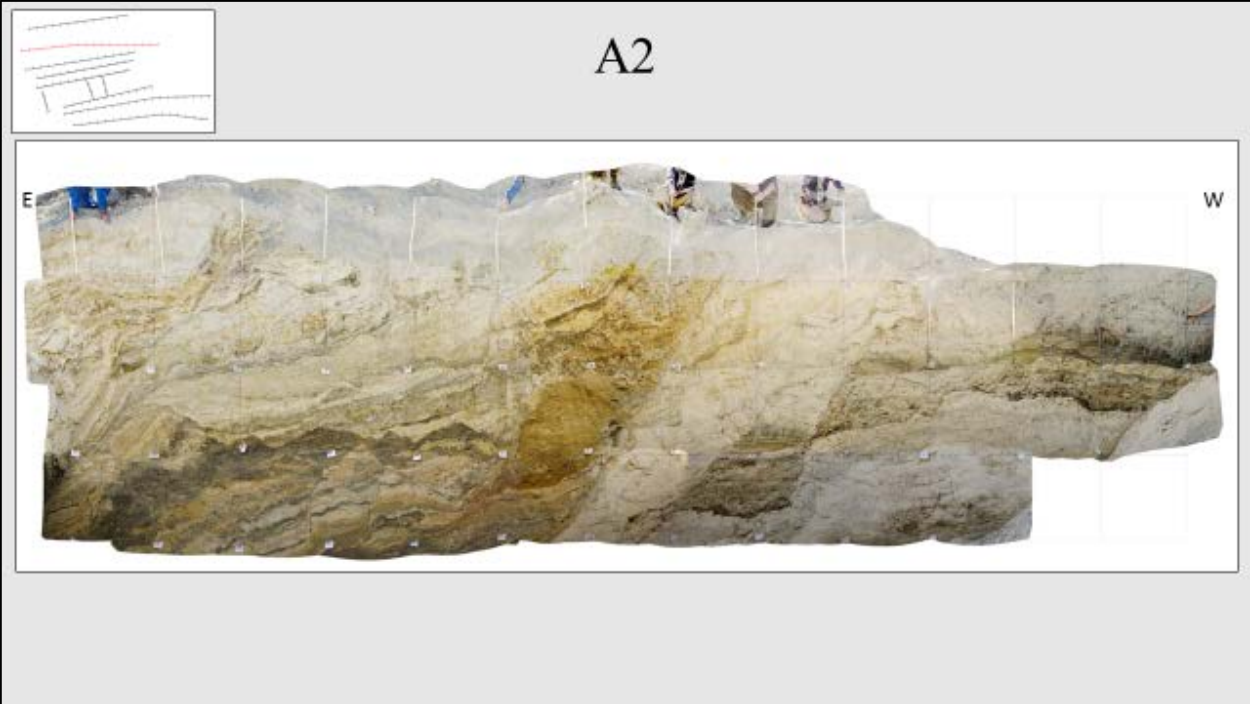
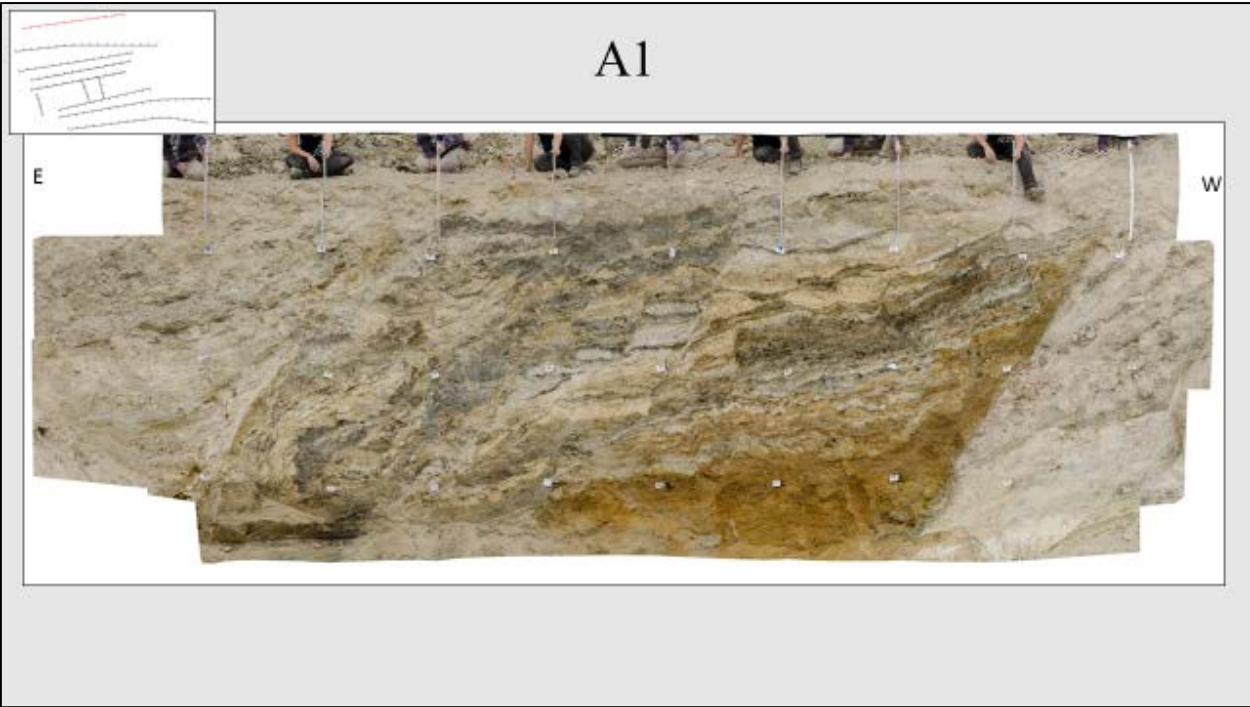
It has been well established that faults are rarely a two-dimensional surface, but rather occupy a 3D volume with a structure and evolution that often are poorly understood. This problem extends from the multitude of parameters that affect the formation of the fault zone and the fact that there are few outcrops that truly expose fault zones in 3D. By having more detailed outcrop studies, such as the one presented here, we can gain insight into how these structures form and how rock properties such as permeability are distributed across them. This study, although local, has been very revealing. The findings from this project include:

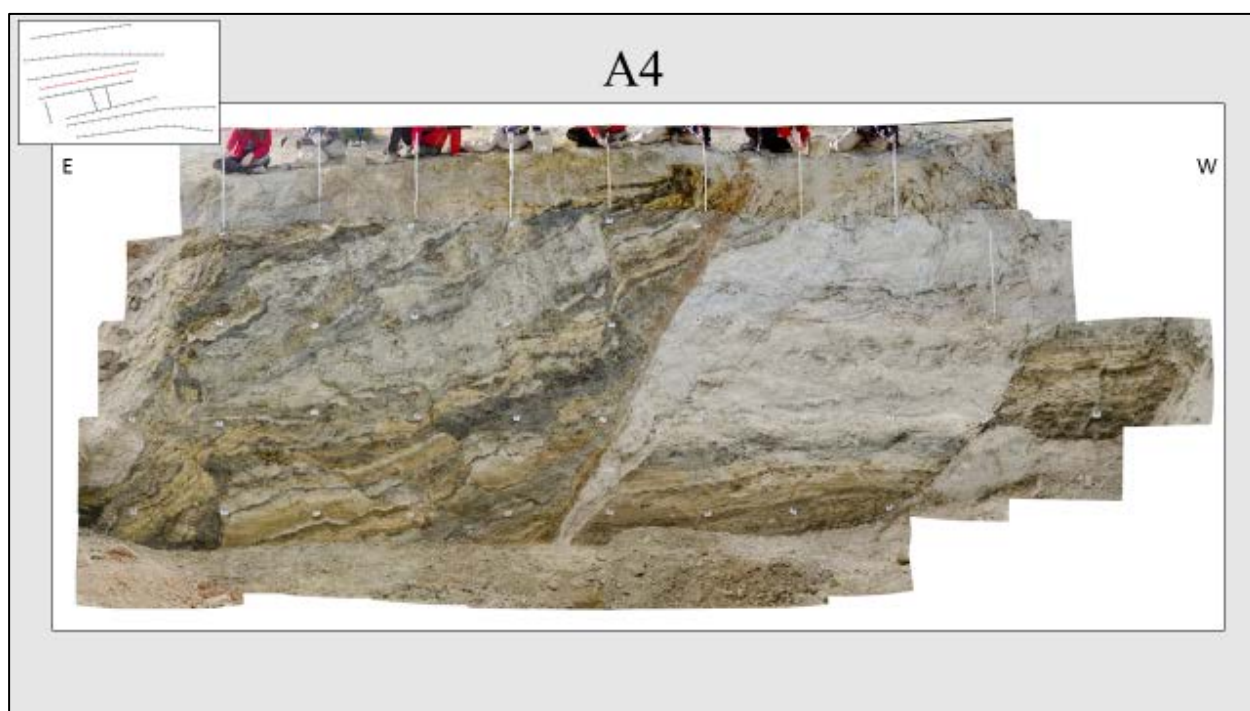
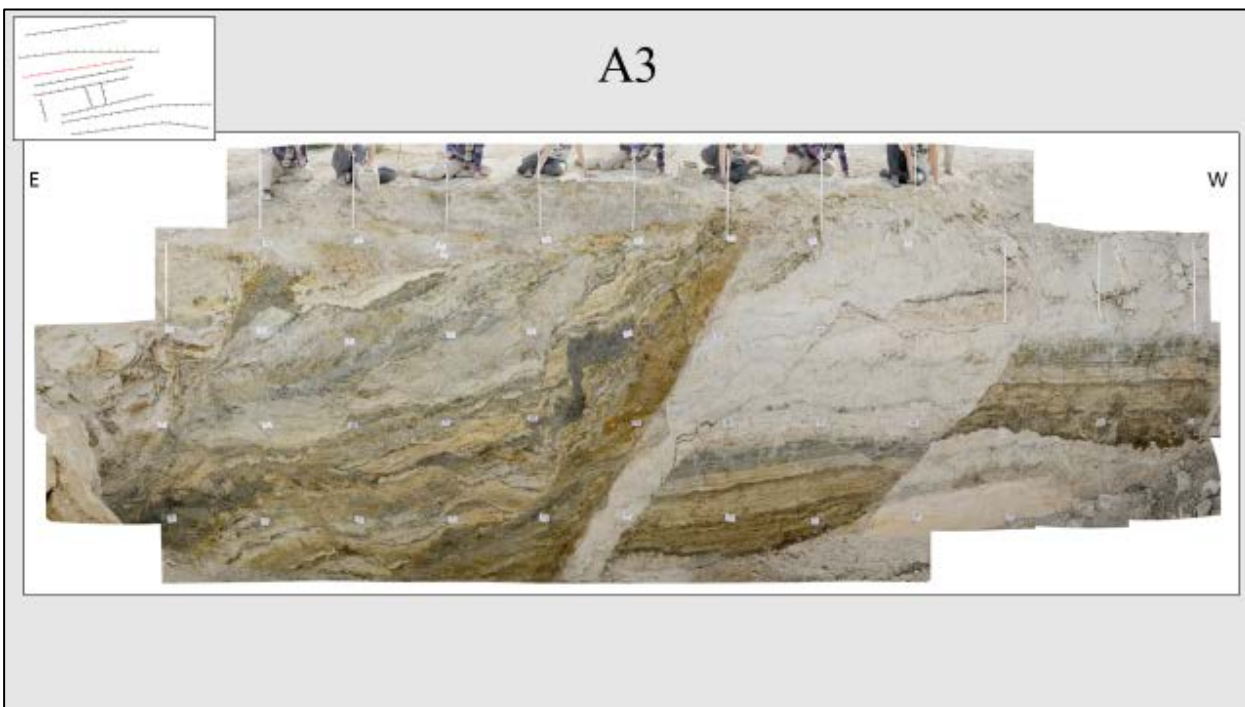
- On a ~30 m throw strand of the Baza fault, identification of 11 fault surfaces striking NE-SW and dipping to the east. These start as a broad zone in the north and merge towards the south. There are minor structures between these faults that change dramatically over just a meter distance.
- There are various forms of deformation mechanisms affecting this area and there is a correlation between the deformation mechanism and the geometry of the structural units.

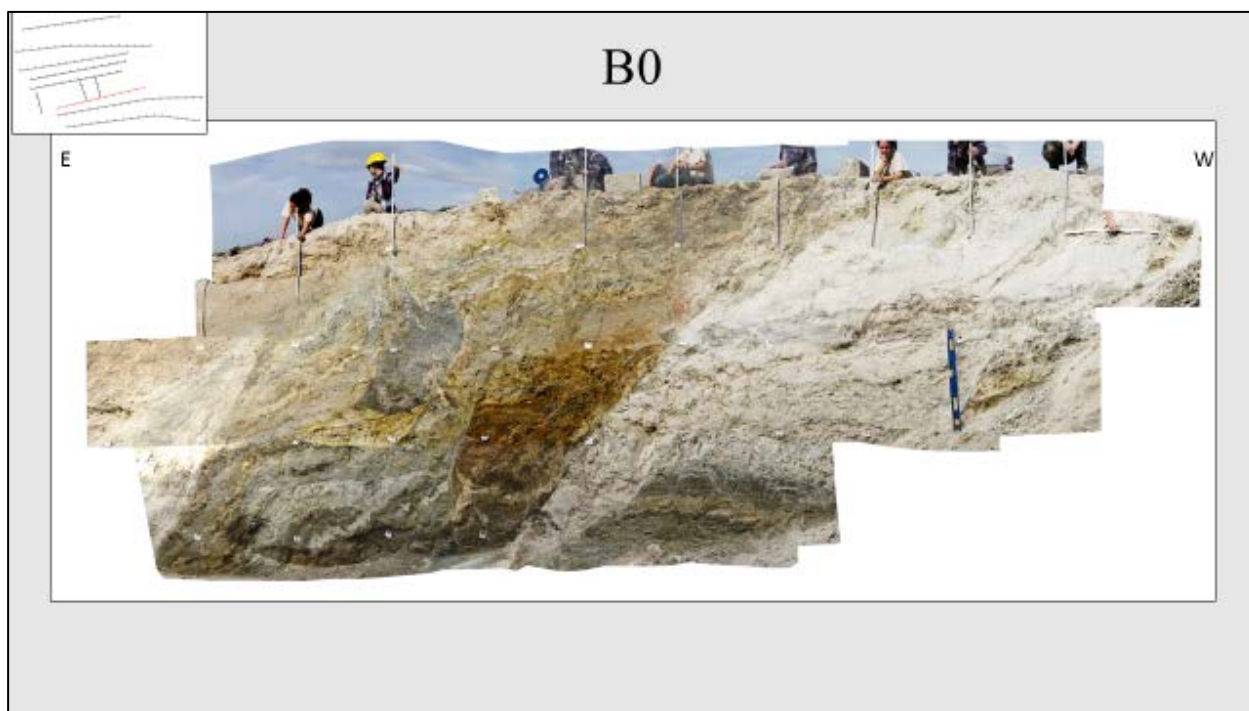
This structural model can be used for further experimentation. By applying a grid system, cells can be populated with attributes and used for flow simulation models and estimation on the impact of a fault zone on flow models. It can also be used for seismic studies. By modeling the seismic response to the lithologic and structural heterogeneity, we can begin to characterize the different properties in a fault zone.

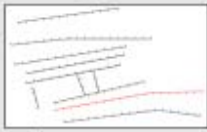
There is always need for more detailed datasets to help both understand the evolution of a fault zone, and for understanding the relationship of fault zone thickness variations. Thus, it would be prudent to continue searching for and studying fault zones in outcrops, particularly along the Baza Fault for a full characterization and across other geological settings. It is undeniable that understanding the properties of a fault zone is imperative for improving reservoir models around faults. Fault zones may seem insignificant on seismic but their impact can be tremendous.

APPENDIX

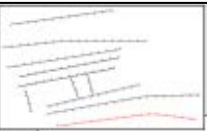








B1



B3

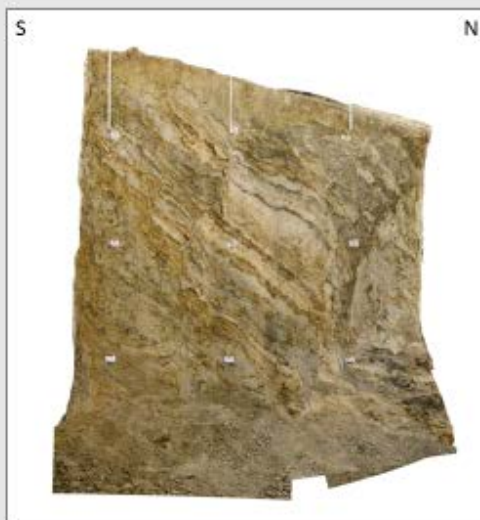




C1



C2

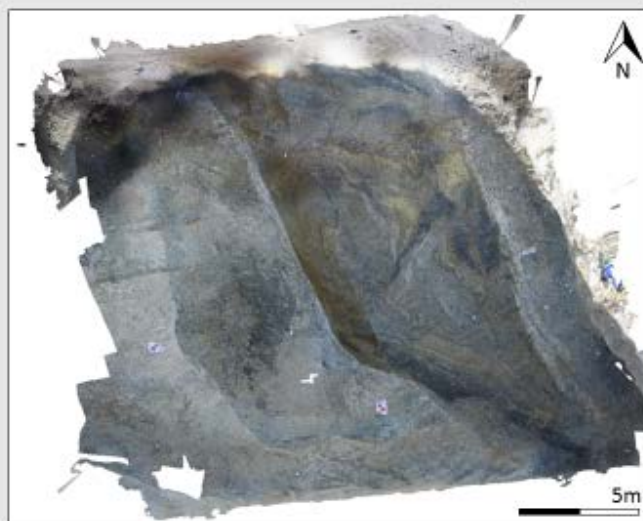




C3



Floor



REFERENCES

- Alfaro, P., Delgado, J., Galdeano, C., Galindo-Zaldívar, J., García-Tortosa, F., López-Garrido, A., . . . Borque, M. (2008). The Baza Fault: a major active extensional fault in the central Betic Cordillera (south Spain). *GR Geologische Rundschau*, 97(6), 1353-1365. doi:10.1007/s00531-007-0213-z
- Alfaro, P., Moretti, M., & Soria, J. (1997). Soft-sediment deformation structures induced by earthquakes (seismites) in pliocene lacustrine deposits (Guadix-Baza Basin. Central Betic Cordillera). *Eclogae Geologicae Helvetiae*, 90(3), 531-540.
- Allan, J.R.L. (1982). *Sedimentary structures, their character and physical basis* (Vol. 1): Elsevier.
- Andersen, K. H. (1983). *Strength and deformation properties of clay subjected to cyclic loading*: Norges Geotekniske Institutt.
- Ben-Zion, Y., & Sammis, C. (2009). Mechanics, structure and evolution of fault zones *Mechanics, Structure and Evolution of Fault Zones* (pp. 1533-1536): Springer.
- Brosch, F.-J., & Kurz, W. (2008). Fault damage zones dominated by high-angle fractures within layer-parallel brittle shear zones: examples from the eastern Alps. *Geological Society, London, Special Publications*, 299(1), 75-95.
- Butler, C., Holdsworth, R., & Strachan, R. (1995). Evidence for Caledonian sinistral strike-slip motion and associated fault zone weakening, Outer Hebrides Fault Zone, NW Scotland. *Journal of the Geological Society*, 152(5), 743-746.
- Calvache, M. L., & Viseras, C. (1997). Long-term control mechanisms of stream piracy processes in southeast Spain. *Earth Surface Processes and Landforms*, 22(2), 93-105.
- Chester, F. M. (1995). A rheologic model for wet crust applied to strike-slip faults. *JOURNAL OF GEOPHYSICAL RESEARCH-ALL SERIES-*, 100, 13033-13033.
- Chester, F. M., & Chester, J. S. (1998). Ultracataclasite structure and friction processes of the Punchbowl fault, San Andreas system, California. *Tectonophysics*, 295(1), 199-221.
- Chester, F., & Logan, J. (1986). Implications for mechanical properties of brittle faults from observations of the Punchbowl fault zone, California. *Pure and Applied Geophysics*, 124(1-2), 79-106.
- Childs, C., Manzocchi, T., Walsh, J. J., Bonson, C. G., Nicol, A., & Schöpfer, M. P. (2009). A geometric model of fault zone and fault rock thickness variations. *Journal of Structural Geology*, 31(2), 117-127.

- Childs, C., Watterson, J., & Walsh, J. (1996). A model for the structure and development of fault zones. *Journal of the Geological Society*, 153(3), 337-340.
- Chu, C., Wang, C., & Lin, W. (1981). Permeability and frictional properties of San Andreas fault gouges. *Geophysical Research Letters*, 8(6), 565-568.
- Cox, S., & Scholz, C. (1988). On the formation and growth of faults: an experimental study. *Journal of Structural Geology*, 10(4), 413-430.
- De Galdeano, C. S. (1990). Geologic evolution of the Betic Cordilleras in the Western Mediterranean, Miocene to the present. *Tectonophysics*, 172(1-2), 107-119.
- DeMets, C., Gordon, R. G., Argus, D. F., & Stein, S. (1994). Effect of recent revisions to the geomagnetic reversal time scale on estimates of current plate motions. *Geophysical Research Letters*, 21(20), 2191-2194.
- Egger, A. E., Glen, J. M., & McPhee, D. K. (2014). Structural controls on geothermal circulation in Surprise Valley, California: A re-evaluation of the Lake City fault zone. *Geological Society of America Bulletin*, 126(3-4), 523-531.
- Evans, J. P. (1990). Thickness-displacement relationships for fault zones. *Journal of Structural Geology*, 12(8), 1061-1065.
- Galindo-Zaldívar, J., Gonzalez-Lodeiro, F., & Jabaloy, A. (1989). Progressive extensional shear structures in a detachment contact in the Western Sierra Nevada (Betic Cordilleras, Spain). *Geodinamica Acta*, 3(1), 73-85.
- García-Tortosa, F. J., Alfaro, P., Galindo-Zaldívar, J., Gibert, L., López-Garrido, A., de Galdeano, C. S., & Ureña, M. (2008). Geomorphologic evidence of the active Baza fault (Betic Cordillera, south Spain). *Geomorphology*, 97(3), 374-391.
- García-Tortosa, F., Alfaro, P., de Galdeano, C. S., & Galindo-Zaldívar, J. (2011). Glacis geometry as a geomorphic marker of recent tectonics: The Guadix–Baza basin (South Spain). *Geomorphology*, 125(4), 517-529.
- Gibbons, W., & Moreno, T. (2002). *The geology of Spain*.
- Gibert, L. (2006). *Análisis de facies y magnetostratigrafía de la cuenca de Baza*. Ph. D. Thesis, Univ. Politècnica de Catalunya, Manresa, Spain.
- Gibert, L., Scott, G., Martin, R., & Gibert, J. (2007). The early to middle Pleistocene boundary in the Baza basin (Spain). *Quaternary Science Reviews*, 26(17), 2067-2089.
- Guerra-Merchán, A., & Ruiz-Bustos, A. (1992). Nuevos datos bioestratigráficos de los materiales continentales del sector suroriental de la Cuenca de Guadix-Baza. El yacimiento de Caniles. *Geogaceta*, 11, 76-78.

- Herraiz, M., Muñoz, V., Lindo, R., Giner, J., Simón, J. L., González Casado, J. M., . . . Casas, A. (2000). The recent (upper Miocene to Quaternary) and present tectonic stress distributions in the Iberian Peninsula. *Tectonics*, *19*(2000TC900006), 762-786.
- Huggins, P., Watterson, J., Walsh, J., & Childs, C. (1995). Relay zone geometry and displacement transfer between normal faults recorded in coal-mine plans. *Journal of Structural Geology*, *17*(12), 1741-1755.
- Jabaloy, A., Galindo-Zaldívar, J., & González-Lodeiro, F. (1992). The Mecina Extensional System: its relation with the post-Aquitania piggy-back basins and the paleostresses evolution (Betic Cordilleras, Spain). *Geo-Marine Letters*, *12*(2), 96-103.
- Lowe, D. R. (1975). Water escape structures in coarse-grained sediments. *Sedimentology*, *22*(2), 157-204.
- Lowe, D. R. (1976). Grain flow and grain flow deposits. *Journal of Sedimentary Research*, *46*(1).
- Manzocchi, T., Childs, C., & Walsh, J. (2010). Faults and fault properties in hydrocarbon flow models. *Geofluids*, *10*(1-2), 94-113.
- Montenat, C. (1990). *Les Bassins Néogènes Du Domaine Bétique Oriental (Espagne): Tectonique Et Sédimentation Dans Un Couloir de Décrochement. Étude Régionale:* Institut géologique Albert de Lapparent.
- Morrow, C., Shi, L., & Byerlee, J. (1984). Permeability of fault gouge under confining pressure and shear stress. *Journal of Geophysical Research: Solid Earth*, *89*(B5), 3193-3200.
- Nichols, R., Sparks, R., & Wilson, C. (1994). Experimental studies of the fluidization of layered sediments and the formation of fluid escape structures. *Sedimentology*, *41*(2), 233-253.
- Ortiz, J. E., Torres, T., Delgado, A., Reyes, E., Llamas, J. F., Soler, V., & Raya, J. (2006). Pleistocene paleoenvironmental evolution at continental middle latitude inferred from carbon and oxygen stable isotope analysis of ostracodes from the Guadix-Baza Basin (Granada, SE Spain). *Palaeogeography, Palaeoclimatology, Palaeoecology*, *240*(3), 536-561.
- Platt, J., & Vissers, R. (1989). Extensional collapse of thickened continental lithosphere: A working hypothesis for the Alboran Sea and Gibraltar arc. *Geology*, *17*(6), 540-543.
- Sagy, A., Brodsky, E. E., & Axen, G. J. (2007). Evolution of fault-surface roughness with slip. *Geology*, *35*(3), 283-286.
- Schmid, S., & Handy, M. (1991). Controversies in Modern Geology.
- Scholz, C., & Bilham, R. (1991). On the mechanics of earthquake afterslip. *Journal of Geophysical Research*, *96*(B5), 8441-8452.

- Seed, B. (1979). SOIL LIQUEFACTION AND CYCLIC MOBILITY EVALUTION FOR LEVEL GROUND DURING EARTHQUAKES. *Journal of Geotechnical and Geoenvironmental Engineering*, 105(ASCE 14380).
- Sibson, R. (1977). Fault rocks and fault mechanisms. *Journal of the Geological Society*, 133(3), 191-213.
- Smith, L., Forster, C., & Evans, J. P. (1990). Interaction between fault zones, fluid flow and heat transfer at the basin scale.
- Tchalenko, J. (1970). Similarities between shear zones of different magnitudes. *Geological Society of America Bulletin*, 81(6), 1625-1640.
- Vera, J. (1970a). Estudio estratigráfico de la Depresión de Guadix-Baza. *Boletín Geológico y Minero*, 81(85), 429-462.
- Vera, J. (1970b). Facies del Plioceno de la Depresión de Guadix-Baza. *Cuad Geol Univ Granada*, 1, 23-25.
- Von Drasche, R. (1879). Bosquejo geológico de la zona superior de Sierra Nevada. *Boletín de la Comisión del Mapa Geológico de España*, 6, 353-388.
- Vrolijk, P. J., Urai, J. L., & Kettermann, M. (2016). Clay smear: Review of mechanisms and applications. *Journal of Structural Geology*, 86, 95-152.
- Wallace, R., & Morris, H. (1979). Characteristics of faults and shear zones as seen in mines at depths as much as 2.5 km below the surface. *United States Geological Survey Open-File Report*, 79, 79-100.
- Wang, H., Li, H., Si, J., Sun, Z., & Huang, Y. (2014). Internal structure of the Wenchuan earthquake fault zone, revealed by surface outcrop and WFSD-1 drilling core investigation. *Tectonophysics*, 619-620, 101-114. doi:10.1016/j.tecto.2013.08.029
- Wibberley, C. A., Gonzalez-Dunia, J., & Billon, O. (2016). Faults as barriers or channels to production-related flow: insights from case studies. *Petroleum Geoscience*, petgeo2016-2057.
- Wibberley, C. A., Yielding, G., & Di Toro, G. (2008). Recent advances in the understanding of fault zone internal structure: a review. *Geological Society, London, Special Publications*, 299(1), 5-33.